WASHINGTON UNIVERSITY IN ST. LOUIS

Department of Chemistry

Dissertation Examination Committee:
Richard A. Loomis, Chair
William E. Buhro, Co-Chair
Sophia Hayes
Nigam Rath
Bryce Sadtler

Surface Modification of II-VI Semiconducting Nanocrystals

by

Calynn Elizabeth Morrison

A dissertation presented to
The Graduate School
of Washington University in
partial fulfillment of the
requirements for the degree
of Doctor of Philosophy

January 2021
St. Louis, Missouri

Table of Contents

List of Figures and Schemes

List of Tables

List of Abbreviations

0D	Zero-dimensional
1D	One-dimensional
2D	Two-dimensional
DTC	Dithiocarbamate
$Cd(Et_2DTC)_2$	Cadmium *n,n'*-diethyldithiocarbamate
$Cd(MePhDTC)_2$	Cadmium *n*-methyl-*n*-phenyldithiocarbamate
EA	Elemental Analysis (combustion)
E_b	Exciton binding energy
E_g	Band-gap
$E_{g,Bulk}$	Bulk Band-gap
E_{QC}	Confinement Energy
EDS	Energy Dispersive X-ray Spectroscopy
FT-IR	Fourier-Transform Infrared Spectroscopy
HOMO	Highest Occupied Molecular Orbital
ICP-MS	Inductively Coupled Plasma – Mass Spectrometry
ICP-OES	Inductively Coupled Plasma - Optical Emission Spectroscopy
L	Length of the quantum confined dimension
L_{eff}	Effective length of the quantum confined dimension
LED	Light Emitting Diode
LUMO	Lowest Occupied Molecular Orbital
m^*	Effective Mass
m_e	Mass of the electron
$M(DTC)_2$	Metal Dithiocarbamate
NMR	Nuclear Magnetic Resonance
OA	*n*-Octylamine
PIB	Particle-in-a-Box
PIW	Particle-in-a-Well

PL	Photoluminescence
PL QY	Photoluminescence Quantum Yields
PLE	Photoluminescence Excitation
PTC	Phenyldithiocarbamate
QB	Quantum Belt
QD	Quantum Dot
QP	Quantum Platelet
QW	Quantum Well
RBS	Rutherford Backscattering
TGA	Thermogravimetric Analysis
$Zn(Et_2DTC)_2$	Zinc *n,n'*-diethyldithiocarbamate
$Zn(MePhDTC)_2$	Zinc *n*-methyl-*n*-phenyldithiocarbamate

<u>Acknowledgments</u>

I would first like to acknowledge my mentors and committee members: Profs. Richard Loomis, Bill Buhro, and Bryce Sadtler. Thank you for your patient instruction and guidance. I would also like to thank Dr. Fudong Wang, whose expertise and practical teaching accelerated my development as a chemist.

On a personal and professional level, I would like to thank my husband, Dr. Paul Morrison. Thank you for understanding, for stepping up, for listening. Thank you for our beautiful children, for being a kind father and patient husband, and for encouraging me when I felt like giving up. Thank you for working hard for us. Thank you for reading over this dissertation. We are so lucky together.

Endless thanks to Dr. William (Matt) Sanderson. Matt, without you, I am not sure I would have finished this degree. Thank you for being a wonderful friend, for taking the time to teach me, for listening, and for countless other acts of kindness that sustained me.

Thanks to all of the former and current members of the Loomis and Buhro labs, notably, Dr. Yang Zhou and Dr. Waynie Schuette.

Thank you to my teaching mentors: Drs. Megan Daschbach and Jia Luo. I have enjoyed professional counsel as well as your friendship.

Thanks to all of the staff of Washington University Department of Chemistry. Thanks especially to Rick Schneider, who has been a steady, hilarious friend through it all.

Additional thanks to the staff of the Institute for Materials Science and Engineering, and the Nano Research Facility and Jens Molecular and Nanoscale Analysis Laboratory, especially Dr. Tyrone Dalton and Dr. Sanmathi Subbenaik.

Thank you to my family, both Johnson and Morrison sides, for your endless love and support. Thanks to all our childcare providers and therapists, (Julia, Linda, Melinda, Khadijah, Abby, Dorrian, Annie, Meredith, Amanda and too many others to list here) for allowing me to return to work with peace of mind, knowing that our children are well-cared for.

Finally, I would like to acknowledge the NSF and Washington University in St. Louis for financial support.

Dedicated to Mom and Dad,

And to

My husband PJ, and our sons, Milo and Finn

ABSTRACT OF THE DISSERTATION

Surface Modification of II-VI Semiconducting Nanocrystals

By

Calynn E. Morrison

Doctor of Philosophy in Chemistry

Washington University in St. Louis, 2021

Professor Richard A. Loomis, Chair

Professor William E. Buhro, Co-Chair

This dissertation presents the compositional analysis of semiconductor materials by inductively coupled plasma optical emission spectroscopy (ICP-OES), a novel low-temperature shell growth precursor and installation pathway, and L-type for Z-type ligand exchange experiments conducted with four metal dithiocarbamate ligands.

The techniques employed in the compositional analysis of semiconductor materials by inductively coupled plasma optical emission spectroscopy (ICP-OES) have a profound influence on the accuracy and reproducibility of the results. In Chapter 3, we describe methods for sample preparation, calibration, standard selection, and data collection. Specific protocols are suggested for the analysis of II-VI compounds and nanocrystals containing the elements Zn, Cd, S, Se, and Te.

In Chapter 4, cadmium bis(phenyldithiocarbamate) [$Cd(PTC)_2$] is prepared and structurally characterized. The compound crystallizes in the monoclinic space group $P2_1/n$. A one-dimensional polymeric structure is adopted in the solid state, having bridging PTC ligands and 6-coordinate pseudo-octahedral Cd atoms. The compound is soluble in DMSO, THF, DMF, and insoluble in EtOH, MeOH, $CHCl_3$, CH_2Cl_2, and toluene. {CdSe[n-octylamine]$_{0.53}$} quantum

belts and $Cd(PTC)_2$ react to deposit epitaxial CdS shells on the nanocrystals. With an excess of $Cd(PTC)_2$, the resulting thick shells contain spiny CdS nodules grown in the Stranski-Krastanov mode. Stoichiometric control affords smooth, monolayer CdS shells. A base-catalyzed reaction pathway is elucidated for the conversion of $Cd(PTC)_2$ to CdS, which includes phenylisothiocyanate and aniline as intermediates, and 1,3-diphenylthiourea as a final product.

Chapter 5 investigates the exchange of *n*-alkylamine ligands on the surface of {CdSe[n-octylamine]$_{0.53}$} quantum belts with four metal dithiocarbamate compounds: zinc *n,n*-diethyldithiocarbamate ($Zn(Et_2DTC)_2$), zinc *n*-methyl-*n*-phenyldithiocarbamate ($Zn(MePhDTC)_2$), cadmium *n,n*-diethyldithiocarbamate ($Cd(Et_2DTC)_2$, and cadmium *n*-methyl-*n*-phenyldithiocarbamate ($Cd(MePhDTC)_2$). Direct exchange of L-type *n*-alkylamine for $M(DTC)_2$ failed to follow trends established in other L-type for Z-type ligand exchange experiments. Experiments to test the exchange of *n*-alkylamine for Z-type $Cd(oleate)_2$ for Z-type $M(DTC)_2$ followed. The reasons for differences in ligand exchange experiments conducted with $M(DTC)_2$s and other Z-type ligands are discussed in detail.

Chapter 1: Introduction

Semiconductor nanocrystals (SCNCs) are of great interest to the materials science, chemical and engineering communities. They have found use in a variety of applications, notably light emitting diodes (LEDs), solar devices, and biological labels.[1] SCNCs are often synthesized from traditional semiconducting materials such as cadmium selenide or gallium arsenide, yet their smallest dimension may only be a few nanometers in width or diameter.[1] Their small size gives rise to the phenomenon known as quantum confinement, which allows for direct control of their optical properties.[2-4] Advances in synthetic techniques have allowed scientists to create a variety of morphologies, notably zero-dimensional (0D) quantum dots (QDs), one-dimensional (1D) quantum wires (QWs), pseudo 1D quantum belts (QBs), and two-dimensional (2D) quantum platelets (QPs).

As the size and shape of these SCNCs vary, so too does the surface area to volume ratio.[5-6] The smaller the SCNCs, the more important the surface becomes in determining the physical and optical properties observed.[6-9] These properties, particularly the optical properties, ultimately dictate the efficiency of any application that relies on the ability of the SCNCs to interconvert light and electronic energy. Thus, understanding and controlling the surface is paramount for device engineering. This dissertation explores the importance and possibilities of purposeful control of the surface via shell growth and ligand exchange.

This introduction serves to review fundamental concepts, definitions and explanations of the optical and structural properties of semiconductors and SCNCs, and examine the role of surface chemistry in determining the overall properties of a nanomaterial. Recent advances in the

treatment of the surface of SCNCs are also reviewed. Lastly, this introduction serves to contextualize the experiments described in this dissertation.

1.1 Semiconductors

In order to understand the properties of SCNCs, it is imperative to understand those of solids and bulk semiconductors. The electronic interactions in most solid materials, including semiconductor materials, result in continuous bands of possible energies, as opposed to the molecular orbitals at distinct energies that exist in smaller chemical structures. Electronic bands and molecular orbitals arise from the superposition of atomic orbitals, which is described by the Linear Combination of Atomic Orbitals (LCAO).

Before considering a bulk solid, it is instructive to first consider a simple diatomic molecule. According to molecular orbital theory models using the LCAO, the number of molecular orbitals must equal the number of atomic orbitals contributing to those molecular orbitals.[10] As illustrated in Figure 1.1, two molecular orbitals are formed by combining two *s* atomic orbitals; the lower energy molecular orbital is a σ (bonding) orbital, and the higher energy molecular orbital is a σ* (antibonding) orbital. There is a discrete energy gap between the σ and σ* molecular orbitals. The electronic configurations of a molecule in the ground-state can be determined by following orbital filling rules, with electrons filling the lowest energy orbitals first.

LCAO can also be applied to continuous and repeating crystal structures. In these structures, there are a large number of atomic orbitals (Figure 1.1) contributing to the formation of an equally large number of molecular orbitals. Due to constraints from quantum mechanics, however, no two quantum states can have the same energy if the states have the same symmetries and quantum numbers. Consequently, the molecular orbitals of large crystal systems

are energetically off-set from one another, forming bands of orbitals that span a continuous range

of energies, instead of discrete states or quantized energies. Figure 1.1 illustrates the formation of
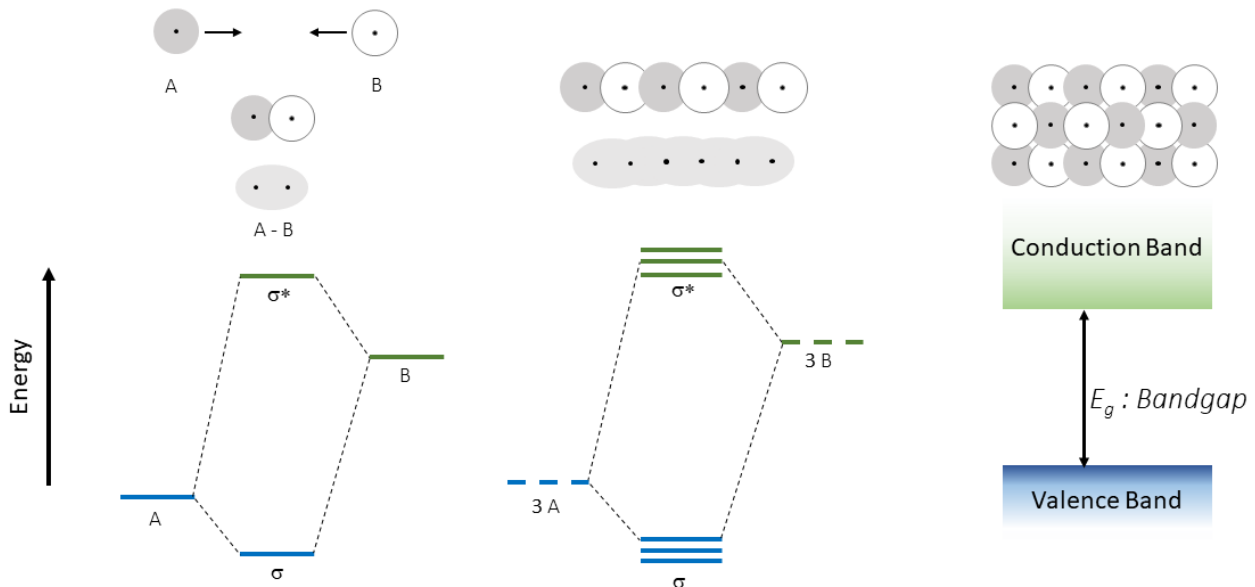
bands.

Figure 1.1   Linear combination of atomic orbitals (LCAO) approximation giving rise to
conduction and valence bands. In the left panel, two atomic orbitals, belonging to atoms A and
B, combine to form bonding (σ) and antibonding ($\sigma*$) molecular orbitals. In the center panel
displays a chain of A-B atoms. When the atomic orbitals of A and B combine, an equivalent
number of σ and $\sigma*$ molecular orbitals are formed. These molecular orbitals are slightly
energetically offset from one another. The right panel displays the combination of a large
number of A and B atoms. When a sufficient number of atoms combine, the resulting molecular
orbitals span a continuous range of energies, or bands.

Orbital filling rules also apply to solids. The lower energy bands, analogous to the highest

occupied molecular orbital (HOMO) in the molecular example, are filled with electrons first. The

highest-energy filled band is called the valence band (VB). The lowest-energy unoccupied band,

analogous to the lowest unoccupied molecular orbital (LUMO), is called the conduction band

(CB). The energetic spacing of these bands determines whether a material is a conductor,

semiconductor, or an insulator. In Figure 1.2, cartoons representing the relative spacing of the

CB and VB of conductors, semiconductors, and insulators are shown. In order for a material to

be conductive (allow for the flow of electric current) there must be electrons in the CB. In a

conductor, the VB and CB energetically overlap. No additional energy is required for electrons

to occupy the conduction band, and they move relatively freely through the material. In an

insulator, there is a large gap between the CB and VB, and a large amount of energy is needed to

promote electrons to the CB. As a result, the free flow of electrons is not typically permitted.

Semiconductors, which form the focus of this thesis, are defined as solid substances with a well-

defined energy gap between the VB and CB, defined as the bandgap energy, E_g.[10] In the ground-

state configuration, a semiconductor material is not conductive, and it behaves as an insulator.

With the input of energy, typically in the form of visible or ultraviolet light, electrons can be

promoted (or excited) to the CB. In this excited state, electrons can freely traverse the material

and the semiconductor behaves as a conductor.
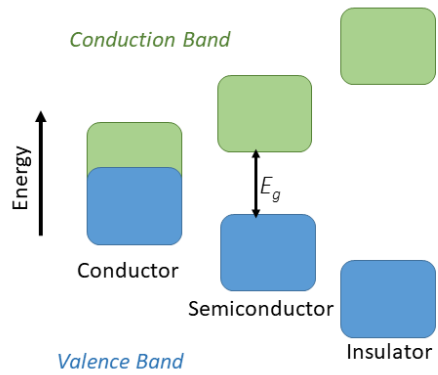
Figure 1.2   Cartoon of the conduction and valence band spacing in conductors, semiconductors and insulators.

When a semiconductor absorbs light of sufficient energy to promote an electron to the

CB, the electron deficient region created by the absence of the electron in the VB acts as a net-

positive charge, referred to as a 'hole.' This is illustrated in Figure 1.3. There is a Coulombic

attraction between the electron and hole. If the attraction is sufficient, the electron and hole are

bound with an energy denoted E_b, or binding energy. The resulting interaction forms an exciton,

which is a neutral quasiparticle. The most probable distance between an excited electron and a

hole is defined as the exciton Bohr radius, R_b, which is unique to each material and the dimensionality of the material in which the exciton is formed. An exciton in bulk CdSe has $R_b =$ 5.4 nm, while an exciton in bulk CdTe has $R_b = 7.5$ nm.[11]
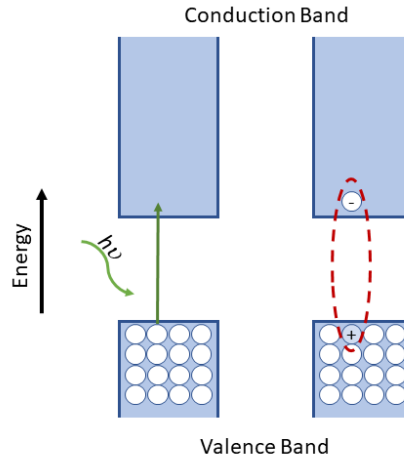
Figure 1.3   The formation of an exciton in a semiconductor. Upon the absorption of a photon of with $h\nu > E_g$, an electron (e^-) is promoted from the valence band to the conduction band. An electron deficient region, or 'hole' (h^+) is created in the valence band. The Coulombic attraction between an electron and a hole can form an exciton.

Electric current is defined as the flow of charged particles past a given point or through a region.[12] In device engineering, it is imperative that current be able to pass through the semiconductor. While an exciton is mobile, its movement does not represent the flow of current, because the exciton itself is neutral. The E_b of an electron and a hole must be overcome to separate the charges and allow for the flow of current. The E_b of an exciton formed in bulk wurtzite CdSe is 15 meV.[13] Once an electron and hole are separated, the charge carriers may independently move through space while occupying their respective bands, allowing for the flow of current.

As the charge carriers move through the crystalline lattice of a semiconductor, they experience varying electronic interactions depending on the direction or wave vector of motion. Figure 1.4a displays a band diagram, where electronic energy is plotted a function of k space, or

momentum space. The term k is defined as the wave vector, and it is proportional to momentum. In a direct bandgap semiconductor, such as wurtzite CdSe, the minimum energy of the CB occurs at the same point in k space as the maximum energy of the VB. This point is referred to as the Γ point, the region highlighted by the yellow box in Figure 1.4a. Figure 1.4b displays a schematic illustrating the bands present near the Γ point. The top three valence states are shown (B, A, and C).[14] The shapes of the bands plotted versus k are commonly approximated as parabolas, proportional to k^2 with a scaling factor of $\hbar^2/(2m^*m_e)$ near the Γ point, where $\hbar$ is a constant, m_e is the mass of a free electron, and m^* is the unitless, effective mass of the carrier in that band. Bands with steep parabolas have small or light m^*, and shallow or broad bands have large or heavy m^*. The three valence band states closest in energy to the band edge are the heavy hole (B band), the light hole (A), and the split-off hole (C) states.[14] Spectral features associated with the B band and A band are present in the absorption spectrum of wurtzite CdSe QBs, discussed in Section 1.2.3.
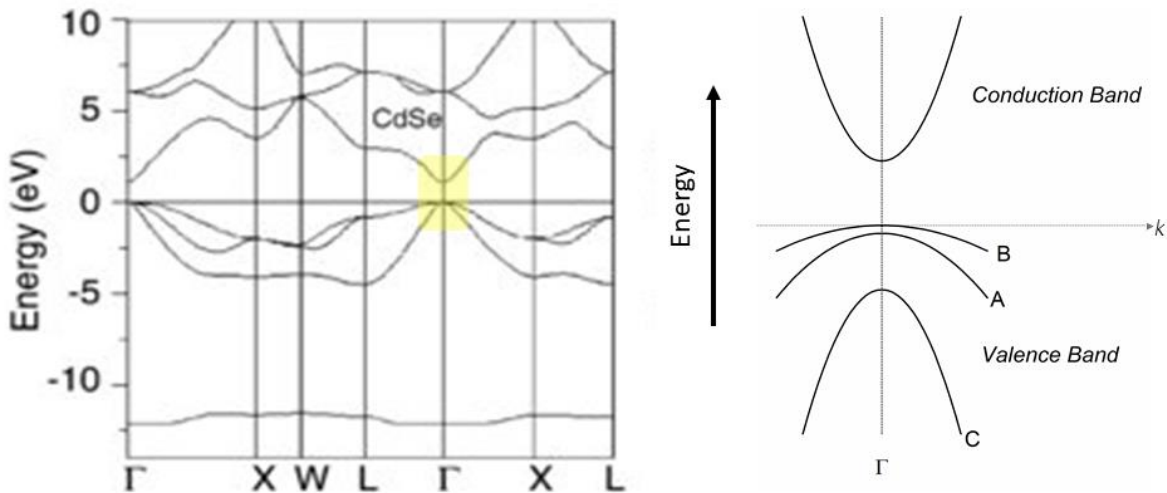
Figure 1.4   (a) Wurtzite CdSe band diagram, with Γ point highlighted in yellow.[10] (b) Schematic enlarged band diagram near the Γ point.

1.2 Semiconductor Nanomaterials

1.2.1 Definitions

SCNCs are fundamentally defined by their chemical composition, surfaces, and size. The term "nanomaterial" refers to a material in which at least one dimension of the material is between 1-100 nm.[1] The tiny scale of SCNCs results in very different physical, chemical and optical properties relative to their bulk counterparts, including, but not limited to, differences in melting point, solubility, toxicity, and absorptivity. Their absorption and emission colors can be tuned by changing their size, due to a phenomenon known as quantum confinement. SCNC materials are also capable of highly efficient emission if the surfaces of the material are properly passivated.

This section describes the phenomenon of quantum confinement and summarizes the structure and properties of the SCNC chosen for experiments described in this dissertation, wurtzite {CdSe[n-octylamine]$_{0.53}$} quantum belts (QBs). The quantum-confinement effect is important for the interpretation of the results presented in Chapters 4 and 5, which detail modifications to the surface chemistry of {CdSe[n-octylamine]$_{0.53}$} QBs.

1.2.2 Quantum confinement

When a SCNC is made with a size in at least one dimension that is on the order of tens of nanometers or less, its size in that dimension is comparable to the size of the wavefunctions of the electrons and holes.[2-4] The electrons and their holes are confined to a finite space, and the wavefunctions of these charge carries become perturbed. Discrete or quantized states result in both the valance and conduction bands of the SCNC. This phenomenon is known as the quantum-confinement effect. The lowest-energy states are shifted to higher energies than the band edges, increasing the E_g of the SCNC relative to the bulk bandgap ($E_{g,Bulk}$). The additional energy is known as quantum-confinement energy (E_{QC}). The observed energy of transitions

between the ground and excited states is equal to the sum of the bulk bandgap ($E_{g,Bulk}$) and the E_{QC}, which is the sum of the quantum confinement energies of the lowest energy states in the conduction and valence bands, less E_b, as shown in equation 1.

$$E_g = E_{g,Bulk} + E_{QC} - E_b \qquad (1.1)$$

The confinement energy of excited charge carriers in 1D quantum systems is often approximated using the quantum-mechanical "Particle-in-a-1D-Box" equation, which is shown below.

$$E_n = \frac{n^2 h^2}{8mL^2} \qquad (1.2)$$

E_n gives the allowed kinetic energy of the particle, and the quantum number of the state is given by n. L is the length of the box (or quantum confined dimension), and m is the mass of the particle, which for a SCNC is equal to the product of the mass of the electron and the reduced mass of the carrier, $m_e \, m^*$. The term h is Planck's constant. In this simple model, the "walls" of the box are an infinite potential energy barrier through which the particle cannot escape to the surrounding environment. Inside the confinement box, there are no forces acting on the particle, other than the walls of the box. As indicated by equation 2, the energetic spacing of the states is inversely proportional to the size or length of the box, L, squared. In SCNC systems, two distinct E_n values exist, one for the CB and one for the VB, which correspond to two distinct confinement energies for the electron and hole. Figure 1.5 illustrates the phenomenon of quantum confinement, and the effects of increasing n and L on the energies of the states.
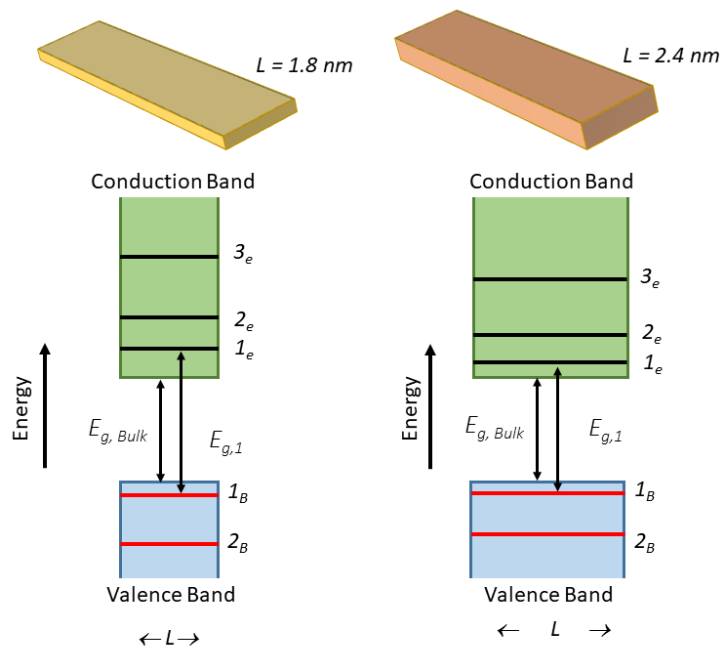
Figure 1.5 The quantum confinement effect. The energies of the discrete states in quantum confined materials are higher in energy than the band gap. The energies of these states in each band are directly proportional to the square of principle quantum number (n), and inversely proportional to the squared value of the length of the quantum-confinement dimension (L), which is the 'x-axis' in these simplified schematic quantum-confinement diagram.

Researchers have developed synthetic procedures for reliably producing various morphologies of quantum-confined SCNCs with a variety of chemical compositions, including but not limited to: spherical or semi-spherical dots, cylindrical or semi-cylindrical wires, and flat platelets and ribbon-like belt structures, which result in three-, two- and one- dimensional confinement of the charge carriers, respectively.[1] The degree of confinement and the dimensionality of a nanomaterial, 0D, 1D, pseudo 1D, or 2D, are related. The charge carriers in structures with three-dimensional confinement have zero degrees of freedom of translational motion, and thus, these structures are sometimes referred to as zero-dimensional or '0D' structures. Likewise, a structure with two-dimensional charge-carrier confinement may be referred to as a '1D' structure, in which the charge carrier has one degree of freedom of translational movement. The shape of these crystals can be accounted for by making changes to

equation 1.2 to account for the symmetries and dimensionalities of the SCNCs. The various

morphologies also have an impact on the density of states within the SCNCs, but an in-depth

discussion of density of states is not related to this dissertation.

As mentioned, the quantum-confinement effect gives rise to the tunability of the optical

and electronic properties of SCNCs.[1, 4] A single material can absorb and emit at various energies,

depending on the diameter or width of the quantum-confined dimension. The experiments

described in this dissertation primarily utilize{CdSe[n-octylamine]$_{0.53}$} QBs.[15] The properties

and composition of these structures are discussed in Section, 1.2.3.

1.2.3 {CdSe[n-octylamine]$_{0.53}$} Quantum Belts

The research efforts presented in this dissertation were performed on {CdSe[n-

octylamine]$_{0.53}$} QBs, in which charge carriers are confined in one dimension.[16] These QBs were

chosen because of their highly reproducible synthesis, nearly atomic flat faces, well-defined

spectral features, high photoluminescence (PL) quantum yields (QY), and the sensitivity of their

spectral properties to surface modification.

Wurtzite{CdSe[n-octylamine]$_{0.53}$} QBs are grown in n-octylamine bilayer templates.[16-18]

A typical synthesis yields belts approximately 1 μm in length and 5-10 nm in width, with a

discrete thickness of 1.8 nm. The 1.8 nm thickness corresponds to a structure of five monolayers

of continuously bonded atoms, as shown in the edge-on view presented in Figure 1.6a. Each

surface cation (cadmium) and anion (selenium) is ligated by n-octylamine, which gives rise to

the stoichiometry of {CdSe[n-octylamine]$_{0.53}$}.[15]

The broad top and bottom facets of {CdSe[n-octylamine]$_{0.53}$} QBs are neutral, with an

equal number of cations (Cd) and anions (Se).[15, 17] Because of the wurtzite crystal structure, the

neutral facets are corrugated, creating "ridges" and "valleys."[15, 17] Figure 1.6b displays a top-

down view of the belts; the Cd and Se in the ridge positions are shown in red and yellow, while

the Cd and Se in the valley positions are displayed in grayscale. The edge facets, shown in figure

1.6a, represent a very small portion of the overall surface area of the belt and contribute

minimally to the overall character of the QBs. Overall, the stoichiometry of the as-synthesized

QBs is 1:1 Cd:Se.[15, 19]
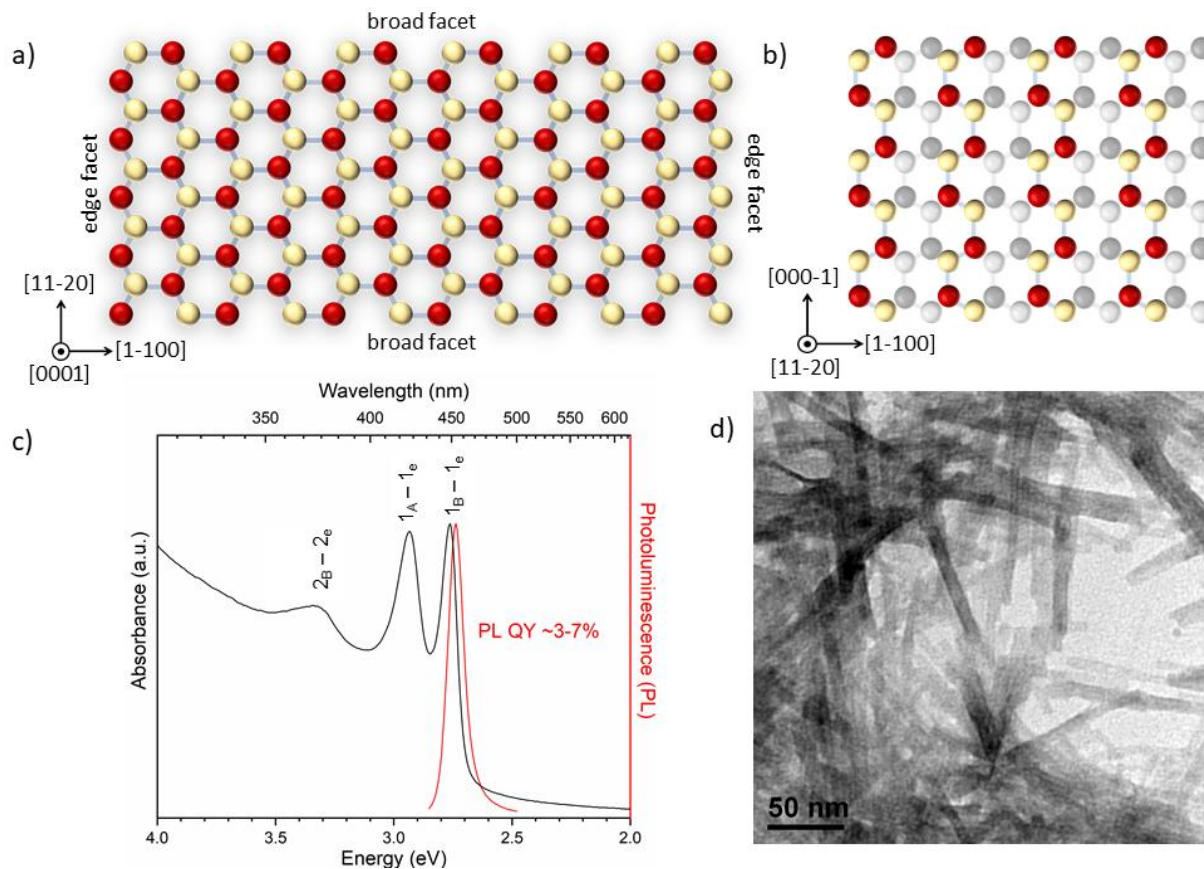
Figure 1.6   {CdSe[n-octylamine]$_{0.53}$} quantum belts structure and optical properties. (a) An edge-on view of a 1.8 nm {CdSe[n-octylamine]$_{0.53}$} QB. Cd atoms are shown in red and selenium atoms are shown in yellow; (b) a top-down view of a part of a {CdSe[n-octylamine]$_{0.53}$} QB, where Cd and Se in the ridge position are shown in red and yellow, respectively, and Cd and Se in the valley positions are shown in gray-scale. (c) The absorbance and photoluminescence (PL) spectra of {CdSe[n-octylamine]$_{0.53}$} QBs. The three lowest-energy transitions are labeled. (d) TEM images of unbundled CdSe QBs.[20]

The UV-Vis absorption and PL spectra (Figure 1.6c) of {CdSe[n-octylamine]$_{0.53}$} QBs

show sharp, distinct features. The two lowest energy features, 1_B-1_e and 1_A-1_e, correspond to the

11

heavy and light hole transitions to the first electronic state in the CB (n=1), respectively.[16] The lowest energy (1_B-1_e) feature in the absorption spectrum is at 2.76 eV, which is approximately 1 eV higher than the bulk bandgap.[16] The PL spectrum is bright, with literature PL QYs up to 30%[21] (although a *typical* synthesis will achieve lower PL QYs), and displays a Stokes shift of 25 meV.

As previously stated, the spectral properties of these structures are sensitive to surface modification. Displacing even a small percentage of the native *n*-octylamine ligands impacts the position and intensity of the peaks in both the UV-Vis and PL spectra.[15] Given the relative ease of these measurements and the sensitivity of these structures to surface modification, wurtzite CdSe QBs are a natural choice for the surface chemistry experiments discussed in this dissertation.

1.3   Surface Chemistry

1.3.1   Defining the Surface

For SCNCs, controlling the chemistry of the surface is imperative, both from fundamental and engineering perspectives.[5-6, 22] The surface chemistry of SCNCs impacts nearly all physical and optical properties, ranging from the dispersibility of nanoparticles in solution to the modulation of the energies of the quantum-confinement states, to controlling carrier relaxation along competing pathways. The small size and length scales of the quantum confined dimension force the wavefunctions of the electrons and holes to sample the surfaces of the SCNCs. Instead of resembling a quantum-mechanical particle-in-an-infinite box system, it is more accurate to think of the SCNCs as particles confined in boxes with finite heights. The surfaces of the SCNCs dictate the heights and shapes of the confining potentials, and contribute to the energetics and dynamics of the carriers.

Traditional materials chemistry defines a surface as an interface between two distinct materials or two distinct phases, or the interface of a material and vacuum.[23] The surface of a material may differ significantly from the bulk interior both in composition and behavior, because the chemical equilibrium that exists at the surface of a material is different from that of the interior of a bulk material. The surface of any material is prone to the formation of "dangling bonds," lattice contraction or expansion,[24] and chemi- and physiabsorption of surrounding species.[6] However, in the bulk, the surface represents only a tiny portion of the overall material, and surface imperfections tend to be ignored when considering the overall properties.

While seemingly straightforward, the definition of the surface becomes murky at the nanoscale. As the physical size of a nanocrystal shrinks, the fraction of atoms that interact with the surrounding environment increases, and at some small dimension, all of the atoms within a nanomaterial may be impacted by the effects mentioned above.[7] It could be argued, that, due to their size, many nanocrystals are entirely surface structures. Analytical techniques used to probe the "surface" often probe the first 1-20 nm of a material,[25] which may be well beyond the thickness of any individual nanocrystal, especially that of the CdSe QBs utilized in the experiments detailed in Chapters 3, 4 and 5.

In this dissertation, a specific definition of the surface is developed and used for clarity. Herein, the 'surface' is comprised of the atoms that are not fully coordinated to other atoms inside the crystalline structure of a nanomaterial. In Figure 1.7, a top-down view of a broad facet of a {CdSe[n-octylamine]$_{0.53}$} QB is shown. Cd and Se atoms in the ridge position are represented by red and yellow spheres, respectively. These ridge-position atoms are coordinated to only three other atoms within the crystal, not four other atoms, and are surface atoms by this definition. The fourth coordination site for both Cd and Se surface atoms in the wurtzite CdSe

QBs is occupied by a neutral ligand, *n*-octylamine, represented by the blue dots. The Cd and Se

atoms in the valley positions are presented in grayscale, and are entirely coordinated to other

atoms, i.e., four bonds, within the crystal structure. These atoms would not be considered surface

atoms by this definition of the surface.
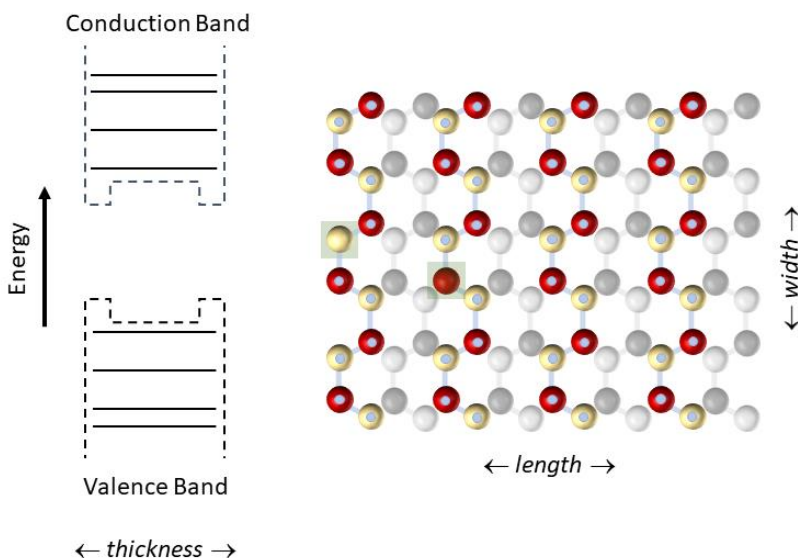
Figure 1.7   The surface {CdSe[*n*-octylamine]$_{0.53}$} QBs and the formation of "dangling bonds." A schematic energy diagram shows potential energy minima associated with unpassivated surface sites. The dangling bonds formed by Cd atoms with no ligation are lower in energy than the lowest state in the conduction band, while dangling bonds formed by Se atoms with no ligation are higher in energy than the highest state in the valence band.

If a coordination site of a surface atom is not passivated, it creates a "dangling bond."[6]

These dangling bonds form potential energy minima at the surface of the SCNC, as shown in the

schematic quantum-confinement diagram in Figure 1.7. The dangling bonds formed by

unpassivated Cd atoms a potential energy minimum relative to the lowest state of the conduction

band. Likewise, dangling bonds from unpassivated Se atoms are a potential energy 'minimum'

for holes (higher in energy relative to the highest state in the valence band). Purposeful control of

these vacant coordination sites (surface sites), is ultimately the subject of this dissertation.

Modification of the surface of SCNCs can be achieved by two methods: 1) growing a crystalline shell of a different material (i.e. depositing CdS on the surface of CdSe quantum dots) or 2) adding or exchanging organic or inorganic ligands. The research presented in this dissertation makes use of both techniques.

1.3.2   Shells

This section provides basic definitions associated with SCNC core-shell heterostructures, and to illustrate how energetic offsets at the interface of distinct materials affect charge-carrier behavior. These energetic differences are most easily visualized using the block-like schematics that represent core-shell heterostructures, but the effects can be generalized to surface modifications that employ organic and inorganic ligands.

A core-shell heterostructure is a class of SCNCs in which a semiconducting material of one composition is epitaxially grown over a SCNC of a different composition.[1, 26] Synthetic techniques for the deposition of shells have enabled researchers to produce a variety core-shell structures, and with that, a variety of energetic landscapes, as shown in Figure 1.8. Shell-growth allows for the passivation of the dangling bonds associated with both surface cations and anions, which can improve the uniformity of the potential energy barrier associated with the surface.

Type I core-shell semiconductors are synthesized by adding layers of a wider bandgap material to the surface of a narrower bandgap material, usually in effort to boost PLQY.[26] If aligned correctly, as shown in Figure 1.8, the wider bandgap material efficiently energetically confines the electron and hole to the core, thereby eliminating low-energy surface traps. By confining the charge carrier wavefunctions to the core, the electron and hole wavefunctions are forced to physically overlap. This increases the probability of radiative recombination, which is experimentally monitored by PLQY.
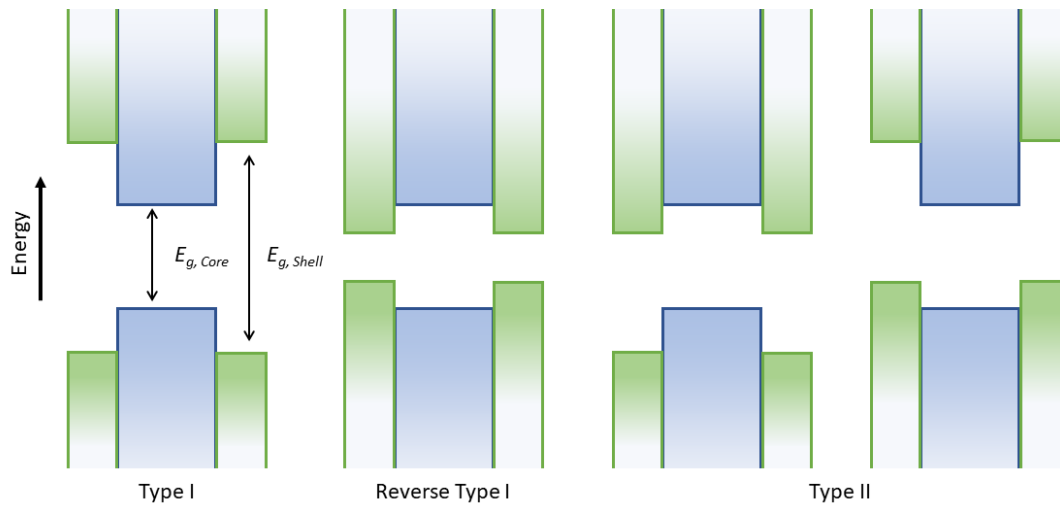
Figure 1.8   Types of core-shell heterostructures. "Core" materials are represented in blue, while shell materials are represented in green. Type I structures are formed when a material with a wider band gap is grown on the surface of a narrower bandgap material. Reverse type I structures are composed of a narrower bandgap material grown on a wider bandgap material. Type II structures are formed when band gaps of the core and shell material are offset.

Reverse Type I core-shell structures are composed of a narrower bandgap material grown atop a wider bandgap material with proper alignment, as shown in Figure 1.4.[26] If the wavefunction of the exciton can be localized within the shell, recombination of an excited electron and hole occurs within the shell region of the SCNC. Thus, the thickness of the shell determines the emission wavelength. These structures tend to have low PLQYs because the charge carriers interact with the surface of the structures, and are thus exposed to surface defects.

Type II core-shell structures are formed when the band edges of the core and shell material are offset in the same direction.[26] This separation is utilized for separation of the electron and hole. The emission of such structures may be quenched because the electron and hole may be physically separated and prevented from radiatively recombining. Alternatively, the emission may significantly shifted to lower energy relative to the core-only structure, if one of the charge carriers can delocalize into the shell. This increases the "effective L" of the quantum confinement potential, and is discussed in detail in Chapter 4.

While shells offer the advantage of eliminating both cationic and anionic traps created by dangling bonds at the surface, there are drawbacks to using this passivation technique.[1, 26] The first drawback is the semi-permanent nature of the surface modification. The shells behave as extensions of the crystalline lattice; they are tightly bound and cannot be modified without etching.[6-7] Secondly, when an epitaxial layer of another semiconductor is deposited, lattice mismatch between the two species can result in stability problems.[1, 27] Lattice mismatch refers to the situation in which two materials with different lattice constants are brought together by deposition of one material on top of another, generating strain.[27] Depending on the morphology of the nanocrystal, this procedure can result in brittle structures that easily degrade due to the strain on the lattice. For example, if a shell is applied to a spherical structure (quantum dot), the strain is evenly distributed.[6] However, in a SCNC with a long dimension (QW or QB), the lattice strain is additive over the length of SCNCs. The structures become prone to breakage.[17, 28-29]

1.3.3 Ligands

Ligand-Nanocrystal Coordination Chemistry

The second major way to amend the surface of SCNCs is by exchange of the ligands that decorate the surface. Like core-shell structures, the choice and extent of ligation determines the shape and energetic offset of the energetic potential at the surface of SCNCs.[6-7, 30-31] This section summarizes the nomenclature and basic concepts from coordination chemistry that are applied throughout the literature to describe ligand-nanocrystal interactions.

A system developed by M.L.H Green[32] is used to categorize ligands by how they contribute to the oxidation state of the atom to which they coordinate. L-type ligands are neutral Lewis bases, which act as two-electron donors when coordinating to the metal centers of other ligands, or to the surface cations of SCNCs. Z-type ligands are composed of a central metal atom

covalently bonded to two anions (MX_2). MX_2 complexes behave as Lewis acids, in which the metal centers act as two-electron acceptors in the presence of electron donors, or when bound to surface anions of SCNCs. Both L- and Z-type ligands form dative bonds to atoms on the nanocrystal surface.[8] X-type anionic ligands (one-electron donors) form covalent bonds to metals, or to the surface cations of SCNCs. They are considered strongly bound. X-type bound ion-pair (BIP) ligands weakly bind via metal atoms on the surface. Examples of these ligand types are shown in Figure 1.9.
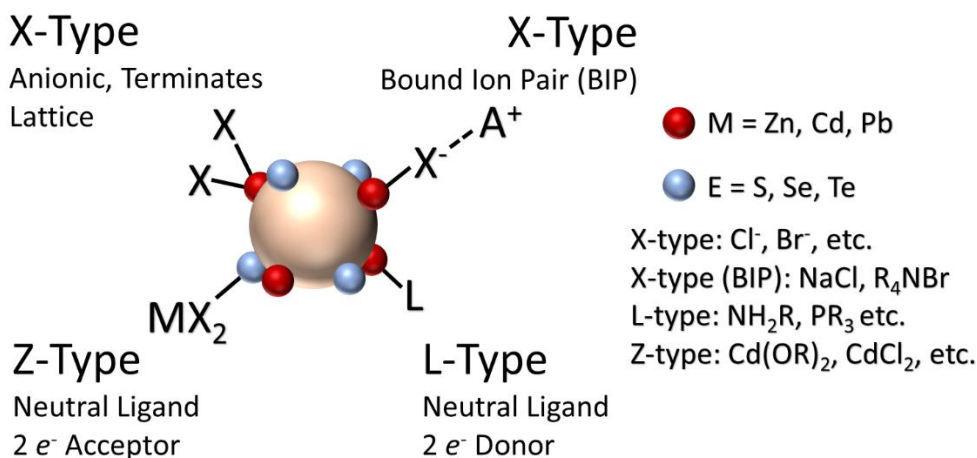
Figure 1.9   Classification of ligands based on the system developed by M. L. H. Green.[32]

This ligand classification system has been used by several groups to form simple guidelines regarding ligand exchange on the surface of SCNCs.[8] In order to maintain the original structure and composition of the nanocrystal, displacement of native ligands requires that the ligands be easily removed: in general, a neutral, L-type ligand cannot displace a strongly bound, one-electron donor X-type ligand without surface reconstruction.[15] However, another one-electron donor ligand, X′, may be successful in displacing the native X-type ligand, depending on the energies of the molecular orbitals.[33-34] L-type ligands, such as amines or phosphines, can usually be displaced by Z-type ligands, such as $Zn(oleate)_2$ or $Cd(oleate)_2$.[15, 35] L-for-Z

exchanges are usually rapid and easily reversible.[15, 35] A bound ion-pair ligand, or A⁺X⁻, cannot usually displace an L-type ligand, but is easily exchanged with a Z-type ligand.[36] Examples of common L-type and Z-type ligands are shown in Figure 1.10.
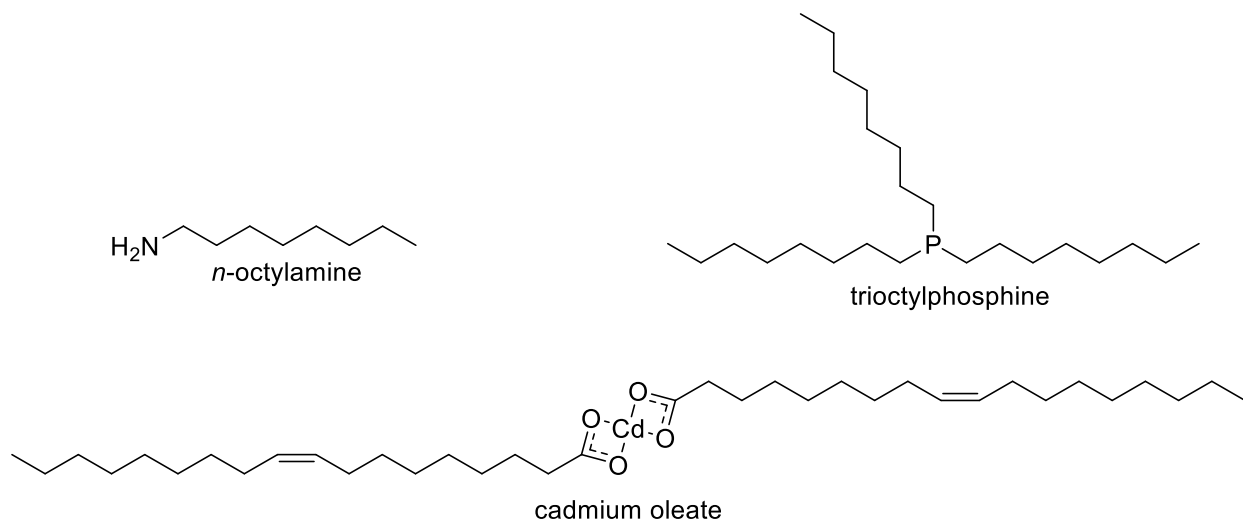
Figure 1.10   Structures of commonly used L- and Z-type ligands. The structures of two common L-type ligands, *n*-octylamine and trioctylphosphine are shown. The structure of Cd(oleate)$_2$, a Z-type ligand, is also shown.

While Green's nomenclature is convenient, useful, and accessible, the classifications cannot predict how tightly a ligand binds to a metal surface atom, relative to another ligand of the same classification. For example, two L-type ligands, like *n*-octylamine and trioctylphosphine may have very different binding energies. Some groups have suggested that successful predictions can be made by considering hard-soft acid-base (HSAB) interactions,[37-38] and by Ligand Field Theory.[31, 39] HSAB predictions can be made from periodic trends.[24] The relative "hardness" or "softness" of a Lewis acid (electron-accepting species) or Lewis base (electron-donating species) is determined by its size and charge state. Larger ions with lower charge states are "soft" and more polarizable, while smaller ions with higher charge states are "hard." HSAB is a way of applying the concept of orbital overlap – "hard" acids will experience more orbital overlap with "hard" bases because of the similarity in size and energetics. Likewise,

"soft" acids will experience more orbital overlap with "soft" bases. A bond between a soft acid and a soft base will be stronger than a bond between a soft acid and a hard base, and vice versa. Many trends have been explained or predicted using HSAB, including ligand-exchange rates.[24, 40] However, HSAB does not explain or predict the changes in the optoelectronic properties of the ligand or nanocrystal once bound to the nanocrystal surface.

Ligand Field Theory categorizes ligands based on their acceptor and donor capabilities in a bond, and is a useful approach for estimating the orbital energies in coordination complexes.[24] As stated previously, the orbital energies of surface atoms represent changes in the potential experienced by charge carrier and can direct charge carrier dynamics. Ligands are segregated into three categories: sigma donors, pi donors, and pi acceptors.[24] Donors contribute electron density and provide additional filled states at the edge of the SCNC structure, whereas acceptors drain electron density from the surface, creating a potential barrier, [41-42] to be discussed in detail later in this section

Ligand-Nanocrystal Interactions

Like shells, the energetics of the molecular orbitals of ligands perturb the potentials experienced by charge carriers in nanocrystal structures, but they offer distinct advantages and greater versatility from an engineering perspective.[6-8] Similar to core-shell structures, the energetic relationship between the conduction and valence bands of the nanocrystal must be appropriately complimented by the HOMO and LUMO of the ligand(s). Generally, ligands will not cause lattice strain in the same fashion as epitaxially grown core-shell structures, modifying energetic pathways while maintaining long-term structural integrity and chemical mutability.[6-8]
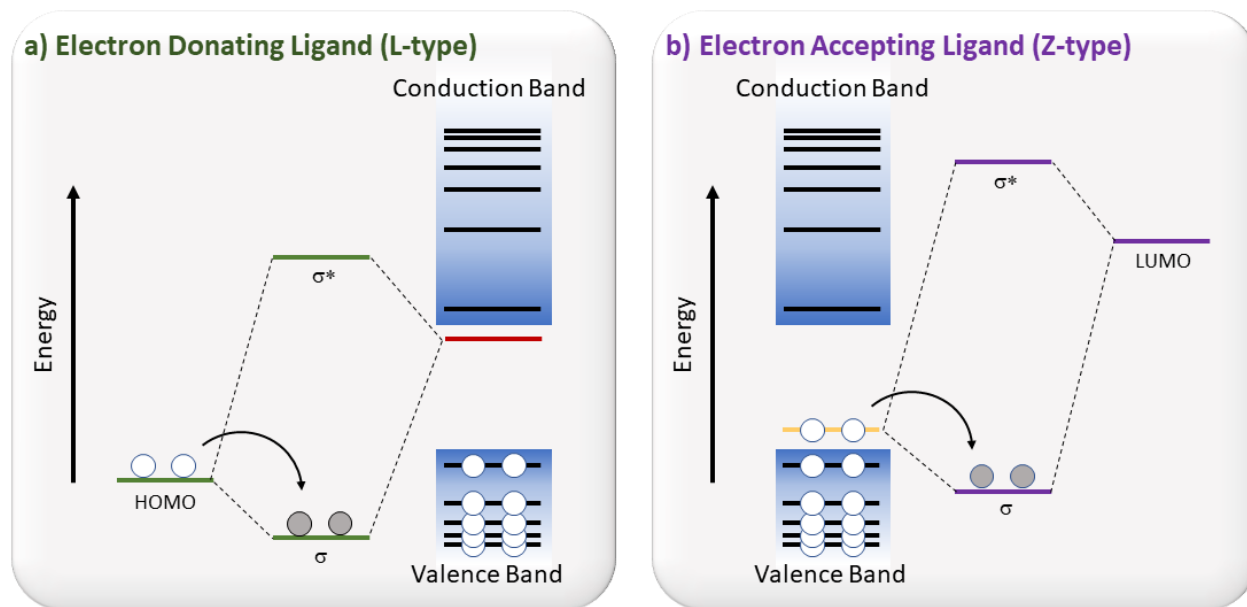
Figure 1.11   A molecular orbital perspective of ligand-nanocrystal interactions.[6] These interactions are specific to the classifications of L-type and Z-type interactions. (a) The HOMO of an electron-donating ligand interacting with the dangling bond created by a surface cation. Interaction with dangling bonds of surface anions or with valence band states is possible, but the ligand would no longer meet the criteria of an L-type ligand. (b) The LUMO of an electron-accepting ligand interacting with the dangling bond created by a surface anion. Interaction with dangling bonds of surface cations or with conduction band states is possible, but the ligand would no longer meet the criteria of a Z-type ligand. Both (a) and (b) demonstrate methods by which localized surface states may be passivated.

The nature of the ligand-nanocrystal interaction is defined by the how the HOMO and LUMO of the ligand interact with the states in the valence and conduction bands.[6, 8] A commonly used interpretation of these interactions is shown in Figure 1.10.[6] A simplified schematic of a SCNC and molecular orbital diagrams of L-type and Z-type ligands are shown. In the case of L-type ligands, (Figure 1.10a), the HOMO of the ligand and a dangling orbital of a surface cation combine. While the HOMO of the ligand and a dangling orbital of a surface selenium could interact (mix with valence band states), this would not meet the classification of an L-type ligand. The resulting σ and σ^* orbitals are pushed to lower and higher energies, respectively, compared to the HOMO of the ligand and the dangling bond of the cation (surface metal atom).

A similar process occurs in the case of electron-accepting ligands (Figure 1.10b). These are not the only two possibilities, nor the only interpretation of the electronic interaction, however, this figure demonstrates how the HOMO/LUMO alignment with the valence or conduction bands can change the potential experienced by charge carries within the structure.

Experimental Methods in Ligand Modification

In practice, ligand exchange methods are relatively simple. Most groups choose to modify the surface post-synthetically rather than adjust an existing synthesis for the SCNC. *In-situ* exchange may occur when as-synthesized nanocrystals are suspended in a solvent, such as toluene, and stirred with the desired ligand for a set length of time. The exchanged nanocrystals are then purified by flocculation techniques and centrifuged.[33,42-43] *Ex-situ* ligand exchange studies are performed by casting a solution of the nanostructures onto a glass slide or coverslip, and then dipping or flowing a solution of the new ligands over the film.[44,45] The experiments in this dissertation utilize *in-situ* exchange.

Nuclear magnetic resonance spectroscopy (NMR), Rutherford back-scattering (RBS), energy dispersive x-ray spectroscopy (EDS), thermogravimetric analysis (TGA), inductively coupled plasma mass spectrometry (ICP-MS), inductively coupled plasma optical emission spectrometry (ICP-OES), combustion elemental analysis (EA) and Fourier transform infrared spectroscopy (FT-IR) are commonly used to assess the composition of semiconducting nanocrystals and changes to their surface. Elucidation of the composition of nanomaterials, especially quantitative values, remains difficult, as   discussed in Chapter 3. Lighter and volatile elements are prone to losses, regardless of the ligand-exchange technique employed.

1.4 Dissertation Hypotheses

1.4.1 Relevant Literature Studies

The experiments and results detailed in this dissertation report the use of L-type to Z-type ligand-exchange schemes to install functional ligands and degrading ligands on surface of wurtzite CdSe QBs. These results build on previous studies reported in the literature.[15, 33, 35, 42, 46-49] The breadth and body of work devoted to the study of the nanocrystal surface has expanded rapidly in the past fifteen years. This section is devoted to summarizing the most relevant works associated with the experiments in this dissertation.

Anderson and coworkers conducted an L-type for Z-type ligand exchange study on carboxylate-terminated QDs (CdSe, CdS, PbSe, PbS).[33] They reported dramatic, reversible changes to the absorption and PL spectra of the QDs were observed upon exchange of native ligands with Lewis bases.[33] According to Anderson et *al*., the exterior of the SCNC can be thought of as an assembly of labile, coordination complexes decorating a stoichiometric core. Incoming ligands can form adducts with these surface-bound coordination complexes, allowing them to be easily removed. This sort of surface reconstruction indicates nanocrystal surface responds to the environment. Phrased slightly differently, a dynamic equilibrium exists between the surface of the nanocrystal and the surrounding environment. If the environment around the nanocrystal changes, the equilibrium may shift to favor native ligand displacement.

In 2015, Yang et al demonstrated that L-type primary amines, such as *n*-octylamine, on the surface of wurtzite CdSe QBs could be readily exchanged for Z-type $M(oleate)_2$ ligands.[15] They observed large energetic shifts in the absorption and PL spectra, up to 140 meV, which were attributed to a combination of the electronic coupling of $Cd(oleate)_2$ to the CdSe nanocrystal lattice, and changes in the strain state of the lattice (lattice expansion) relative to the

amine-passivated CdSe QBs. Both contributions effectively increased the confinement

dimension. Additionally, it was determined that $Cd(oleate)_2$ coordinates to surface Se atoms,

yielding a final stoichiometry of $\{CdSe[Cd(oleate)_2]_{0.26}\}$.

In 2018, Yao and coworkers reported reversible L-type for Z-type ligand exchange with

MX_2 ligands (where M = Zn, Cd and X = Cl^-, I^-, Br^-) on the surface of $\{CdSe(n\text{-octylamine})_{0.53}\}$

QBs.[36] Spectral shifts up to 252 meV were observed with those ligand replacements. These

results demonstrated the instantaneous, facile nature of the exchange and suggested that L-for-Z-

type ligand exchange experiments are generalizable on the surface of $\{CdSe(n\text{-octylamine})_{0.53}\}$.

As mentioned in Section 1.3.3, ligands can be used to alter the confinement potential of

an SCNC in order to separate the electron and hole wave functions.[43,42] Conducting ligands are

selected for the energetic placement of the HOMOs and LUMOs of the frontier orbitals; the

energetic off-set of these orbitals relative to the valence and conduction bands provide the

potential differences necessary for charge separation. The offset of the HOMOs and/or LUMOs

must be enough to overcome the coulombic binding energy.

Frederick and co-workers performed a series of studies using modified phenyl

dithiocarbamate ligands (PTCs) and CdSe quantum dots.[42, 47-49] They demonstrated that the

spectral features of the CdSe QDs shifted to lower energy (up to an eV) upon ligand exchange

with PTC ligands. PTCs are referred to as "non-innocent" ligands, a term used by the

coordination chemistry community to imply strong interactions of the ligand and the metal

center, or in this case, surface cation.

Because of their unique structure, dithiocarbamates can bind to the surface of a SCNC in

multiple ways. The dithiocarbamate can bind through a single sulfur to achieve monodentate,

anionic coordination, or through both sulfurs to achieve bidentate chelation.[50] The redox states of

the metal and ligand are ambiguous; instead, the redox center is delocalized over the entire structure. This interaction leads to the creation of new electronic character without distinct metal and organic phases, making PTCs ideal candidates for strongly coupled ligand-QD systems.[42, 46-49]

phenyldithiocarbamate
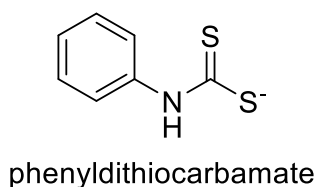
Figure 1.12   Structure of phenyldithiocarbamate (PTC).

1.4.2   Research in this Dissertation

The research presented in this dissertation was undertaken in an effort to learn more about the nature of ligand-nanocrystal interactions, specifically, the interactions of CdSe QBs and a variety of dithiocarbamate derivatives. Purposeful control of the surface is necessary if SCNCs are to be used in devices.[6, 31]

Accurate determination of nanocrystal stoichiometry is imperative for understanding structure – function relationships. The research and interpretation of results in this dissertation require quantitative elemental analysis. In trying to quantitatively determine the stoichiometry of the different CdSe QB-ligand systems, numerous techniques and protocols were followed. Consistent and accurate determination of the chemical constituents could not be determined. As a result, significant effort resulted in the development of an ICP-OES method that can be used to determine the stoichiometry of II-VI semiconducting materials. Methods for sample preparation, calibration, standard selection, and data collection are described in Chapter 3. Specifically, detailed protocols are suggested for the analysis of II-VI compounds and nanocrystals containing the elements Zn, Cd, S, Se, and Te in order to obtain quantitative results.[19]

The investigations described in Chapter 4 were conceived as a combination of the work described by the team of Weiss[42, 46-49] and the work performed by Zhou[15] and Yao, et al.[35] The goal was to install a charge-carrier delocalizing ligand, PTC, on the surface of CdSe QBs using the L-for-Z ligand exchange technology established by Zhou and Yao. PTC, originally installed as an X-type (anionic, 1-electron donor) ligand, was used to synthesize $Cd(PTC)_2$, an MX_2 or Z-type ligand (two electron acceptor). $Cd(PTC)_2$ had not previously been synthesized or reported in the literature. We conducted a full characterization, including single-crystal x-ray analysis. The exchange of primary amine (L-type ligand) for $Cd(PTC)_2$ (Z-type ligand) was attempted, however, $Cd(PTC)_2$ proved to be unstable and susceptible to both acid- and base-catalyzed decomposition. $Cd(PTC)_2$ was then successfully used as a single-source precursor for the growth of CdS shells on the surface of CdSe QBs.

The goal of the research described in Chapter 5 was to develop stabile dithiocarbamates (DTCs) for ligand exchange and explore the changes in the optoelectronic properties of CdSe QBs when those DTCs were installed on the surface. The experiments were undertaken because of the instability of $Cd(PTC)_2$ described in Chapter 4. By synthesizing metal dithiocarbamates $(M(DTC)_2s)$ from a secondary amine, the pathway for base-catalyzed decomposition to CdS is eliminated. In order to test the delocalizing effects of the metal center (Zn vs Cd) versus the effect of the organic substituents of the dithiocarbamate functional group, we present results collected for four related $M(DTC)_2$ ligands: zinc diethyldithiocarbamate $(Zn(Et_2DTC)_2)$, zinc n-methyl-n-phenyldithiocarbamate $(Zn(MePhDTC)_2)$, cadmium diethyldithiocarbamate $(Cd(Et_2DTC)_2$, and cadmium n-methyl-n-phenyldithiocarbamate $(Cd(MePhDTC)_2)$. When compared to other L-type for Z-type ligand exchange experiments, several key differences emerged. The timescale of L-type ligand displacement exceeded that which is typically observed

26

in L-for-Z exchange. The energetic shifting in the absorbance and PL spectra and the retention of PL intensity were insensitive to the identity of the metal center utilized in each ligand. Changes observed in the FT-IR upon binding indicated that the electronic character of the ligand changed upon surface binding. We posit that, unlike other Z-type ligands, $M(DTC)_2$ ligands may not primarily bind through their metal center to surface selenium atoms, but rather through the sulfur of the DTC functional group to the surface cadmiums.

Ultimately, this thesis describes efforts aimed at quantitatively and qualitatively characterizing ligand-exchange strategies, and includes three particularly noteworthy results: (1) ICP-OES is a practical and useful tool for the analysis of semiconducting materials; (2) the growth of CdS shells from $Cd(PTC)_2$ demonstrates the versatility of L-for-Z ligand exchange technology for structural modification; and (3) determination of the surface binding mode of a ligand cannot always be assigned based on the system of ligand classification system developed by M.L.H Green.[32]

1.5   References

1.   Smith, A. M.; Nie, S., Semiconductor Nanocrystals: Structure, Properties, and Band Gap Engineering. *Acc. Chem. Res.* **2010,** *43* (2), 190-200.

2.   Alivisatos, A. P., Perspectives on the Physical Chemistry of Semiconductor Nanocrystals. *J. Phys. Chem.* **1996,** *100* (31), 13226-13239.

3.   Brus, L. E., Electron–Electron and Electron-Hole Interactions in Small Semiconductor Crystallites: The Size Dependence of the Lowest Excited Electronic State. *J. Chem. Phys.* **1984,** *80* (9), 4403-4409.

4.   Bawendi, M. G. S., M.L.; and Brus, L. E., The Quantum Mechanics of Larger Semiconductor Clusters ("Quantum Dots"). *Annu. Rev. Phys. Chem.* **1990,** *41* (1), 477-496.

5.   McBride, J. R.; Pennycook, T. J.; Pennycook, S. J.; Rosenthal, S. J., The Possibility and Implications of Dynamic Nanoparticle Surfaces. *ACS Nano* **2013,** *7* (10), 8358-8365.

6.   Boles, M. A.; Ling, D.; Hyeon, T.; Talapin, D. V., The Surface Science of Nanocrystals. *Nat. Mater.* **2016,** *15* (2), 141-153.

7.   Kilina, S. V.; Tamukong, P. K.; Kilin, D. S., Surface Chemistry of Semiconducting Quantum Dots: Theoretical Perspectives. *Acc. Chem. Res.* **2016,** *49* (10), 2127-2135.

8.   Owen, J., The Coordination Chemistry of Nanocrystal Surfaces. *Science* **2015,** *347* (6222), 615-616.

9.   Hines, D. A.; Kamat, P. V., Recent Advances in Quantum Dot Surface Chemistry. *ACS Appl. Mater.* **2014,** *6* (5), 3041-3057.

10.   Haug, H.; Koch, S. W., *Quantum Theory of the Optical and Electronic Properties of Semiconductors*. Fifth Ed. ed.; World Scientific Publishing Co.: 2009.

11.   *Semiconductors - Basic Data*. 2nd revised edition ed.; Springer: Berlin, 1996.

12.   McKelvey, J. P., *Semiconductor and Solid State Physics*. Krieger Pub Co: 1982

13.   Pelant, I.; Valenta, J., *Luminescence Spectroscopy of Semiconductors*. OUP Oxford: 2012.

14.   Lew Yan Voon, L. C.; Willatzen, M.; Cardona, M.; Christensen, N. E., Terms Linear in k in the Band Structure of Wurtzite-Type Semiconductors. *Phys. Rev. B* **1996,** *53* (16), 10703-10714.

15.   Zhou, Y.; Wang, F.; Buhro, W. E., Large Exciton Energy Shifts by Reversible Surface Exchange in 2D II–VI Nanocrystals. *J. Am. Chem. Soc.* **2015,** *137* (48), 15198-15208.

16.   Liu, Y.-H.; Wayman, V. L.; Gibbons, P. C.; Loomis, R. A.; Buhro, W. E., Origin of High Photoluminescence Efficiencies in CdSe Quantum Belts. *Nano Lett.* **2010,** *10* (1), 352-357.

17.   Wang, F.; Wang, Y.; Liu, Y.-H.; Morrison, P. J.; Loomis, R. A.; Buhro, W. E., Two-Dimensional Semiconductor Nanocrystals: Properties, Templated Formation, and Magic-Size Nanocluster Intermediates. *Acc. Chem. Res.* **2015,** *48* (1), 13-21.

18.   Wang, Y.; Liu, Y.-H.; Zhang, Y.; Kowalski, P. J.; Rohrs, H. W.; Buhro, W. E., Preparation of Primary Amine Derivatives of the Magic-Size Nanocluster $(CdSe)_{13}$. *Inorg. Chem.* **2013,** *52* (6), 2933-2938.

19.   Morrison, C.; Sun, H.; Yao, Y.; Loomis, R. A.; Buhro, W. E., Methods for the ICP-OES Analysis of Semiconductor Materials. *Chem. Mater.* **2020,** *32* (5), 1760-1768.

20.   Sanderson, W. M.; Hoy, J.; Morrison, C.; Wang, F.; Wang, Y.; Morrison, P. J.; Buhro, W. E.; Loomis, R. A., Excitation Energy Dependence of Photoluminescence Quantum Yields in Semiconductor Nanomaterials with Varying Dimensionalities. *J. Phys. Chem. Lett.* **2020,** *11* (9), 3249-3256.

21.   Liu, Y.-H.; Wayman, V. L.; Gibbons, P. C.; Loomis, R. A.; Buhro, W. E., Origin of High Photoluminescence Efficiencies in CdSe Quantum Belts. *Nano Lett.* **2009,** *10* (1), 352-357.

22.   Drijvers, E.; De Roo, J.; Martins, J. C.; Infante, I.; Hens, Z., Ligand Displacement Exposes Binding Site Heterogeneity on CdSe Nanocrystal Surfaces. *Chem. Mater.* **2018,** *30* (3), 1178-1186.

23.   Prutton, M., *Introduction to Surface Physics*. Oxford University Press: Oxford, United Kingdom, 1994.

24.   Gary L. Miessler, P. J. F., Donald A. Tarr, *Inorganic Chemistry*. Pearson Education, Inc.: Upper Saddle River, NJ, 2013.

25.   Hoye, R. L. Z.; Schulz, P.; Schelhas, L. T.; Holder, A. M.; Stone, K. H.; Perkins, J. D.; Vigil-Fowler, D.; Siol, S.; Scanlon, D. O.; Zakutayev, A.; Walsh, A.; Smith, I. C.; Melot, B. C.; Kurchin, R. C.; Wang, Y.; Shi, J.; Marques, F. C.; Berry, J. J.; Tumas, W.; Lany, S.; Stevanović, V.; Toney, M. F.; Buonassisi, T., Perovskite-Inspired Photovoltaic Materials: Toward Best Practices in Materials Characterization and Calculations. *Chem. Mater.* **2017,** *29* (5), 1964-1988.

26.   Ghosh Chaudhuri, R.; Paria, S., Core/Shell Nanoparticles: Classes, Properties, Synthesis Mechanisms, Characterization, and Applications. *Chem. Rev.* **2012,** *112* (4), 2373-2433.

27.   Ji, B.; Panfil, Y. E.; Waiskopf, N.; Remennik, S.; Popov, I.; Banin, U., Strain-Controlled Shell Morphology on Quantum Rods. *Nat. Commun.* **2019,** *10* (1), 2.

28.   Morrison, C. E.; Wang, F.; Rath, N. P.; Wieliczka, B. M.; Loomis, R. A.; Buhro, W. E., Cadmium *Bis*(phenyldithiocarbamate) as a Nanocrystal Shell-Growth Precursor. *Inorg. Chem.* **2017,** *56* (21), 12920-12929.

29.   Hoy, J.; Morrison, P. J.; Steinberg, L. K.; Buhro, W. E.; Loomis, R. A., Excitation Energy Dependence of the Photoluminescence Quantum Yields of Core and Core/Shell Quantum Dots. *J. Phys. Chem. Lett.* **2013,** *4* (12), 2053-2060.

30.   Kaniyankandy, S.; Rawalekar, S.; Verma, S.; Palit, D. K.; Ghosh, H. N., Charge Carrier Dynamics in Thiol Capped CdTe Quantum Dots. *PCCP* **2010,** *12* (16), 4210-4216.

31.   Liu, P.; Qin, R.; Fu, G.; Zheng, N., Surface Coordination Chemistry of Metal Nanomaterials. *J. Am. Chem. Soc.* **2017,** *139* (6), 2122-2131.

32.   Green, M. L. H., A New Approach to the Formal Classification of Covalent Compounds of the Elements. *J. Organomet. Chem.* **1995,** *500* (1), 127-148.

33.   Anderson, N. C.; Hendricks, M. P.; Choi, J. J.; Owen, J. S., Ligand Exchange and the Stoichiometry of Metal Chalcogenide Nanocrystals: Spectroscopic Observation of Facile Metal-Carboxylate Displacement and Binding. *J. Am. Chem. Soc.* **2013,** *135* (49), 18536-18548.

34.   Anderson, N. C.; Owen, J. S., Soluble, Chloride-Terminated CdSe Nanocrystals: Ligand Exchange Monitored by ^{1}H and ^{31}P NMR Spectroscopy. *Chem. Mater.* **2013,** *25* (1), 69-76.

35.   Yao, Y.; Zhou, Y.; Sanderson, W. M.; Loomis, R. A.; Buhro, W. E., Metal-Halide-Ligated Cadmium Selenide Quantum Belts by Facile Surface Exchange. *Chem. Mater.* **2018,** *30* (8), 2848-2857.

36.   Yao, Y.; DeKoster, G. T.; Buhro, W. E., Interchange of L-, Z-, and Bound-Ion-Pair X-Type Ligation on Cadmium Selenide Quantum Belts. *Chem. Mater.* **2019,** *31* (11), 4299-4312.

37.   Nag, A.; Zhang, H.; Janke, E.; Talapin, D. V., Inorganic Surface Ligands for Colloidal Nanomaterials. *Z. Phys. Chem.* **2015,** *229* (1-2), 85.

38.   Champouret, Y.; Spataro, G.; Coppel, Y.; Gauffre, F.; Kahn, M. L., Nanocrystal–Ligand Interactions Deciphered: the Influence of HSAB and pKa in the Case of Luminescent ZnO. *Nanoscale Adv.* **2020,** *2* (3), 1046-1053.

39.   del Rosal, I.; Mercy, M.; Gerber, I. C.; Poteau, R., Ligand-Field Theory-Based Analysis of the Adsorption Properties of Ruthenium Nanoparticles. *ACS Nano* **2013,** *7* (11), 9823-9835.

40.   Pearson, R. G., Hard and Soft Acids and Bases. *J. Am. Chem. Soc.* **1963,** *85* (22), 3533-3539.

41.   Morris-Cohen, A. J.; Donakowski, M. D.; Knowles, K. E.; Weiss, E. A., The Effect of a Common Purification Procedure on the Chemical Composition of the Surfaces of CdSe Quantum Dots Synthesized with Trioctylphosphine Oxide. *J. Phys. Chem. C* **2009,** *114* (2), 897-906.

42.   Frederick, M. T.; Amin, V. A.; Weiss, E. A., Optical Properties of Strongly Coupled Quantum Dot–Ligand Systems. *J. Phys. Chem. Lett.* **2013,** *4* (4), 634-640.

43.   Buckley, J. J.; Couderc, E.; Greaney, M. J.; Munteanu, J.; Riche, C. T.; Bradforth, S. E.; Brutchey, R. L., Chalcogenol Ligand Toolbox for CdSe Nanocrystals and Their Influence on Exciton Relaxation Pathways. *ACS Nano* **2014,** *8* (3), 2512-2521.

44.   Liu, F.; Zhu, J.; Wei, J.; Li, Y.; Hu, L.; Huang, Y.; Takuya, O.; Shen, Q.; Toyoda, T.; Zhang, B.; Yao, J.; Dai, S., *Ex Situ* CdSe Quantum Dot-Sensitized Solar Cells Employing Inorganic Ligand Exchange To Boost Efficiency. *J. Phys. Chem. C* **2013,** *118* (1), 214-222.

45.   Santhosh, K.; Samanta, A., Exploring the CdTe Quantum Dots in Ionic Liquids by Employing a Luminescent Hybrid of the Two. *J. Phys. Chem. C* **2012,** *116* (38), 20643-20650.

46.   Harris, R. D.; Amin, V. A.; Lau, B.; Weiss, E. A., Role of Interligand Coupling in Determining the Interfacial Electronic Structure of Colloidal CdS Quantum Dots. *ACS Nano* **2016,** *10* (1), 1395-1403.

47.   Knowles, K. E.; Frederick, M. T.; Tice, D. B.; Morris-Cohen, A. J.; Weiss, E. A., Colloidal Quantum Dots: Think Outside the (Particle-in-a-)Box. *J. Phys. Chem. Lett.* **2012,** *3* (1), 18-26.

48.   Frederick, M. T.; Amin, V. A.; Cass, L. C.; Weiss, E. A., A Molecule to Detect and Perturb the Confinement of Charge Carriers in Quantum Dots. *Nano Lett.* **2011,** *11* (12), 5455-5460.

49.   Frederick, M. T.; Weiss, E. A., Relaxation of Exciton Confinement in CdSe Quantum Dots by Modification with a Conjugated Dithiocarbamate Ligand. *ACS Nano* **2010,** *4* (6), 3195-3200.

50.   Transition Metal Dithiocarbamates: 1978–2003. In *Progress in Inorganic Chemistry*, Hogarth, G., Ed. 2005; pp 71-561.

Chapter 2: General Experimental Methods

2.1   Synthesis

Unless otherwise specified, all syntheses were carried out under dry, anaerobic conditions using standard Schlenk line and glovebox techniques.[1]

Preparation of Dry Solvents

Solvents were prepared according to literature procedures.[2] Activated 3 Å aluminosilicate molecular sieves (approx. 175 mL) were added to a 500 mL round bottom flask. HPLC grade solvents, toluene, dichloromethane, tetrahydrafuran, dimethylsulfoxide, ethanol, dimethylformamide, were added (300 mL) to the round bottom flask, capped with a rubber septa, and purged with N_2 for 15-20 min. Solvents were allowed to rest for 48 h prior to use, at which time they were filtered via 0.2 μm Teflon filter or forced through tightly packed, clean glass wool to remove particulates. Solvents were stored under N_2.

Degassing of Solvents

Solvents were degassed according to well-known "freeze-pump-thaw" procedures.[1]

Preparation of {CdSe[*n*-octylamine]$_{0.53}$} Quantum Belts

{CdSe[*n*-octylamine]$_{0.53}$} QBs were synthesized by modification of a previously reported procedure.[3] Cd(OAc)$_2$·2H$_2$O (40 mg, 0.14 mmol) and *n*-octylamine (3.15 g, 24 mmol) were added to a Schlenk flask and purged with N_2. The flask was transferred to a 70 °C oil bath for 1 h. A solution of selenourea (29 mg, 0.24 mmol) in *n*-octylamine (0.675 g, 5.2 mmol) was

prepared in a small, septum-capped vial and sonicated (20 min) to ensure dissolution. The

selenourea solution was injected into the Schlenk flask containing $Cd(OAc)_2 \cdot 2H_2O$ and n-

octylamine. The reaction was held at 70 °C for 16 h, at which time tri-n-octylphosphine (1 mL)

was injected into the flask to scavenge for elemental selenium. The reaction yielded a viscous,

bright-yellow mixture.

Unbundling of {CdSe[n-octylamine]$_{0.53}$} QBs

{CdSe[n-octylamine]$_{0.53}$} QBs were unbundled by modification of a procedure

previously described.[3] An aliquot (1 mL) of the crude reaction mixture was added to a septum-

capped test tube and centrifuged (2 min, 2000 RPM). The supernatant was decanted and the

pellet was resuspended in dry toluene (0.5 mL). An aliquot of n-oleylamine (1.5 mL) was added

to the suspension. The test tube was purged with N_2, and allowed to rest on the bench top

overnight. The {CdSe[n-octylamine]$_{0.53-x}$[n-oleylamine]$_x$} QBs settled to the bottom of the test

tube. Mild centrifugation (1000 RPM, 2 min) was used to separate the settled belts from the

supernatant, which was then decanted. The belts were then resuspended in dry, degassed toluene.

2.2   Analysis and Characterization

Absorbance Spectroscopy

UV − visible spectra were obtained from a PerkinElmer Lambda 950 UV/vis/NIR

spectrometer equipped with a 150 mm integration sphere to minimize attenuation due to

scattering spectrometer.

Photoluminescence Spectroscopy

Photoluminescence spectra were collected on a Horiba Fluorolog-3 spectrometer with a Quanta-phi integration sphere.

Fourier-Transform Infrared Spectroscopy (FT-IR)

FT-IR spectra were collected on a Bruker ALPHA Platinum ATR spectrometer or a Thermo Scientific Nicolet 470 spectrometer.

Nuclear Magnetic Resonance Spectroscopy (NMR)

^{1}H NMR and ^{13}C{H} NMR spectra were collected using a Varian Unity Inova-500 NMR spectrometer.

Transmission Electron Microscopy (TEM) and Energy Dispersive X-ray Spectroscopy (EDS)

HR-TEM images were obtained from a JEOL JEM 2100F microscope operating at 200 keV. TEM images and EDS data were collected on a JEOL 2000FX microscope operating at 200 keV.

Inductively Coupled Plasma Optical Emission Spectroscopy (ICP-OES) and Combustion Elemental Analysis

ICP-OES methods are described in detail in Chapter 3. Combustion Elemental analyses (C, H, N, S) were obtained by Galbraith Laboratories.

X-ray Powder Diffraction

Powder XRD patterns were recorded on a Bruker AXS D8 ADVANCE powder diffractometer, using Cu K$_\alpha$ radiation (λ = 1.5418 Å).

2.3   References

1.   Shriver, D. F. D., M. A. , *The Manipulation of Air Sensitive Compounds*. 2nd ed.; Wiley & Sons: New York, NY, 1986.

2.   Williams, D. B. G.; Lawton, M., Drying of Organic Solvents: Quantitative Evaluation of the Efficiency of Several Desiccants. *J. Org. Chem.* **2010,** *75* (24), 8351-8354.

3.   Liu, Y.-H.; Wayman, V. L.; Gibbons, P. C.; Loomis, R. A.; Buhro, W. E., Origin of High Photoluminescence Efficiencies in CdSe Quantum Belts. *Nano Lett.* **2010,** *10* (1), 352-357.

Chapter 3: Methods for the ICP-OES Analysis of Semiconductor Materials

3. 1 Introduction

Determination of the stoichiometries of semiconductor nanocrystals is a key aspect of their characterization. Most standard syntheses afford nanocrystals having a super-stoichiometric layer of metal cations at their surfaces, such that the metal-to-nonmetal ratio M/E exceeds one.[2-7] The excess charge from the super-stoichiometric cations is counterbalanced by surface-bound anionic ligands. Such non-stoichiometric semiconductor nanocrystals may be interconverted with stoichiometric nanocrystals having charge-neutral surface ligation.[3, 5] Thus, the core stoichiometries of semiconductor nanocrystals are variable and dependent on the surface ligation and nanocrystal size. Understanding and controlling the surface chemistry benefits from the precise determination of nanocrystal core stoichiometry.

Compositional analyses of semiconductor nanocrystals have been conducted by X-ray photoelectron spectroscopy (XPS),[8-11] Rutherford back scattering (RBS),[2-3, 8-9, 12-14] atomic-absorption spectroscopy,[15] inductively coupled plasma mass spectrometry (ICP-MS),[4, 16-17] inductively coupled plasma optical-emission spectroscopy (ICP-OES),[7, 16, 18-19] X-ray fluorescence spectroscopy (XRF),[20] and energy-dispersive X-ray spectroscopy (EDS) using a transmission electron microscope (TEM).[7] These techniques can divided into two categories:

"beam techniques," which include XPS, RBS, XRF, and EDS, and "digestion-requisite analyses," with ICP-OES, ICP-MS, and FAAS requiring that samples be digested prior to analysis.

While each analysis method comes with a unique set of advantages and disadvantages, accurate and precise determination of lighter elements or volatile components of semiconducting materials can be challenging regardless of the analytical technique employed. In the case of beam techniques, high-energy photons, electrons or ions strike the material and may eject lighter or volatile elements, degrade the surface or change the oxidation state and crystal structures *during* the measurement.[21-23] Difficulties determining exact stoichiometries have been reported in XPS, with up to 46% difference between initial and final measurements of metal ions in samples during depth profiling.[23] Some techniques, such as XRF, require that samples must be homogeneous and meet "infinite thickness requirements" in order to produce accurate results.[24] Ligand exchange or surface-chemistry experiments may only result in differences of a single monolayer of atoms between nanostructures,[3, 5, 13, 25] and thus, beam-analysis techniques could yield stoichiometries that deviate from actuality.

Errors in composition similar to those in beam techniques often accompany digestion-requisite techniques. The formation of volatile products of acid digestion results in losses *before* the measurement,[26-27] however, by altering the digestion and sample-preparation method, volatile elements and surface components may be retained for measurement, as we demonstrate in this paper. Analyses performed by ICP-OES, ICP-MS, and FAAS are total-composition measurements. Because the samples are digested prior to analysis, particle size or sample thickness is irrelevant. ICP-OES and ICP-MS are capable of detecting concentrations in the parts per million (approximately mg/L) and parts per billion range, respectively.[26] ICP

techniques are capable of analyzing upwards of 70 elements simultaneously. With multiple emission wavelengths per element, interferences from spectral overlaps can generally be overcome. ICP-OES also offers the convenience to the user of high sample throughput.

In the majority of studies reporting the stoichiometries of semiconductor nanocrystals cited above, the measured M/E ratios have fallen in the range of 1.0 – 1.8,[2, 4, 8, 10, 14, 16-17, 20] and, in about a third of these studies the determined values were larger.[7, 15, 18-19] Interestingly, all but one of the studies employed a digestion technique prior to analysis. In the specific case of zinc blende (ZB) CdSe nanoplatelets, four-monolayer specimens with an expected Cd/Se ratio of 1.25 analyzed for 1.80 ± 0.07,[16] and five-monolayer specimens with an expected[28] Cd/Se ratio of 1.20 analyzed for 1.72 ± 0.11, by ICP-OES.[16] (The expected Cd/Se ratios are taken from an analysis of ZB CdS nanoplatelets having the same numbers of monolayers.[28]) While these measured ratios are close to expectation, they are *higher*, matching the outcomes of most of our initial efforts at ICP-OES analysis. These observations, and the experiences conveyed to us by others,[29-30] motivated us to conduct a thorough investigation of the ICP-OES analysis of semiconductor materials.

The ICP-OES method detailed in this paper was developed using samples with known or strong theoretical bases for compositions, and protocols were optimized such that our results consistently reflect the expected values. We report results for four samples of semiconductor nanocrystals, one nanocluster, and one molecular compound as test cases.

We identify several pitfalls associated with conventional ICP-OES analysis. We offer suggestions for improving reproducibility and accuracy in methods for sample digestion, calibration-curve construction, and emission-line and calibration-standard selection. We provide specific protocols for the analysis of compounds and nanocrystals containing cadmium, zinc,

41

sulfur, selenium, and tellurium, which we expect to apply more generally to the analysis of other semiconductor materials, such as InP and PbS. We demonstrate that seemingly small variations in sample preparation, calibration, and data collection can have a large impact on the reliability of the results.

3.2   Materials

The following nanomaterials were prepared as described in previous reports: $\{CdSe[n\text{-}octylamine]_{0.53}\}$ quantum belts (QBs),[31] $\{CdSe[Cd(oleate)_2]_{0.19}\}$ QBs,[5] $[(CdSe)_{13}(n\text{-}PrNH_2)_{13}]$ clusters,[32] $\{CdTe_{0.50}Se_{0.50}[oleylamine]_x\}$ and $\{CdTe_{0.73}S_{0.27}[oleylamine]_z\}$ quantum platelets (QPs).[27]

Trace-metal grade nitric acid (70%) and trace-metal grade hydrogen peroxide (32%) were obtained from Millipore Sigma. Zinc diethyldithiocarbamate (97%) was obtained from Sigma Aldrich. HPLC grade ethanol and methanol were obtained from Sigma Aldrich. A multielement calibration standard containing Sr, Ba, V, Cr, Co, Ni, Cu, Zn, Mo, Cd, Hg, Pb, U, As, and Se (1000 µg/mL) was obtained from Spex Certiprep. A Pure™ multielement standard containing As, Tl (100 µg/mL), Cd, Pb, Se (50 µg/mL) and a PurePlus™ multielement standard containing Au, Hf, Ir, Pd, Pt, Rh, Ru, Sb, Sn, Te (10 µg/mL) were obtained from Perkin Elmer. Four single-element calibration standards, Cd, Se, Te, and S, (1000 µg/mL) were obtained from Inorganic Ventures. Ultrapure water was obtained from a Millipore Direct-Q UV-3 filtration system.

Polypropylene and high-density polyethylene screw-cap centrifuge tubes were obtained from Corning and VWR (Figure A1). A 1000 µL solvent-resistant Nichiryo Nichipet EX Plus II™ and Eppendorf ResearchPlus™ Micropipettes were employed during ICP-OES sample preparation procedures.

Analyses were conducted using a PerkinElmer ICP-OES PE Optima 7300DV with Syngistix for ICP, Version 2.0.0.22336 software. Detailed instrument settings can be found in Table A1.

3.3 Procedure

3.3.1 Estimation of Concentration from Synthesis

Analyte solutions were ultimately prepared in the concentration range of 0.5-20 mg/L (see Note 1 in AI). This required estimation of the amount of semiconductor compound contained in an analytical sample. We assumed 100% yield in a given semiconductor nanocrystal synthesis, on the basis of the limiting reagent. The following example is given. In a typical synthesis of {CdSe[n-octylamine]$_{0.53}$} quantum belts (QBs), Cd(OAc)$_2$·2H$_2$O (0.039 g, 1.5 mmol) and selenourea (0.029 g, 2.4 mmol) were allowed to react in n-octylamine (3.825 g), making Cd(OAc)$_2$·2H$_2$O the limiting reagent.[31] The total mass of the crude reaction mixture was 3.893 g.

An aliquot (0.157 g, 200 μL) was withdrawn from the reaction mixture, constituting 4% of the mixture, and containing 4% of the original cadmium (6.6×10^{-4} g, 5.8 μmol). This aliquot was ultimately digested in hydrogen peroxide (500 μL) and nitric acid (500 μL) to produce a concentrated digestion solution. The estimated Cd and Se concentrations in this solution were therefore 660 mg/L. As described below, aliquots of the concentrated digestion solution were diluted to 10.00 mL, to produce analytical solutions having Cd-analyte concentrations of 3.3 – 13.1 mg/L, which were within the desired range for analysis.

3.3.2 General Sample Preparation and Digestion

An aliquot of a nanocrystal dispersion estimated to yield an analyte solution with a final concentration below 20 mg/L (see above) was purified by three centrifugation-washing cycles

using centrifugation at 2000 RPM for three minutes, 2 mL toluene, and a borosilicate test tube in each cycle, each time disposing of the supernatant to remove excess organic material and unreacted precursors. The pellet obtained from the third centrifugation step was then suspended in isopropanol or ethanol, which are solvents compatible with polypropylene and high-density polyethylene (HDPE) centrifuge tubes.[33] The dispersion was transferred to a centrifuge tube, again centrifuged (2000 RPM, 3 min), and the supernatant was removed. The tube was sealed with a rubber septum and dried under vacuum via syringe needle to remove all remaining solvent (Figure A2). A 500 μL aliquot of 30% aqueous hydrogen peroxide solution was added via micropipette, and the centrifuge tube was quickly and tightly closed with a screw cap. The sample was allowed to digest for 3 minutes, after which tube was then opened, a 500 μL aliquot of 65% aqueous nitric acid solution was added, and the cap was promptly replaced. The reaction mixture was allowed to digest for a minimum of 15 minutes, until no solid material remained (and the solution had become optically clear and colorless).

Aliquots of the digestion solution containing 200 μL, 100 μL and 50 μL were pipetted into clean centrifuge tubes and diluted with a 1% aqueous HNO_3 solution to 10.00 mL, giving analyte solutions with concentrations less than 20 mg/L. The tubes remained tightly capped prior to analysis. Analyses were conducted on the day the analyte solutions were prepared.

3.3.3   Preparation of Standard Solutions and Construction of the Calibration Lines

After preparation of the analyte solutions, calibration solutions were prepared u4ng a commercial multi-element calibration standard containing fifteen elements (Sr, Ba, V, Cr, Co, Ni, Cu, Zn, Mo, Cd, Hg, Pb, U, As, and Se) at concentrations of 1000 μg/mL (1000 mg/L). The solutions were prepared in the same PP/HDPE centrifuge tubes mentioned previously. A 200 μL micropipette was used to deliver aliquots of the multi-element standard in volumes of 10 μL, 20

μL, 50 μL, 100 μL, and 200 μL and diluted with 1% HNO_3 to a final volume of 10.00 mL using a 10.00 mL pipette. This yielded calibration solutions with concentrations of 1.0, 2.0, 5.0, 10.0 and 20.0 mg/L, respectively.

Emission spectra were collected at the following wavelengths: for Cd, 214.438, 226.502 and 228.802 nm, and for Se, 196.026 and 203.985 nm. Once the appropriate conditions were obtained, the integrated areas of the spectral lines recorded as a function of concentration then fit to a straight line to obtain the calibration lines for analyte, as discussed below.

3.3.4   Analysis of Experimental Samples

After data collection from the calibration standards, emission spectra were obtained for the experimental analyte solutions at the same wavelengths as used with the standards: for Cd, 214.438, 226.502 and 228.802 nm, and for Se, 196.026 and 203.985 nm. The spectral data were exported, plotted, and inspected for overlapping emission lines. Overlapping emission lines are described in detail in the Results and Discussion portion of this paper.

Figure 1 displays the linear fits obtained from the calibration data for known concentrations of Cd and Se. Integrated emission intensities of the spectral lines for digested {CdSe[*n*-octylamine]$_{0.53}$} QBs obtained from three dilutions of experimental analyte solutions are plotted as squares, circles, or triangles on the calibration lines. The concentration of the experimental analyte solutions in mg/L was determined by plugging the value of the integrated intensity into the linear fit equation and solving for the concentration. The emission lines of Cd at 226.502 nm and Se at 196.026 nm were selected to determine the Cd:Se molar ratios. An example of the conversion of measured mg/L data to a molar ratio is given in eq 3.1.   Error calculations are omitted for clarity. The final ratios reported were averages of those obtained from the various dilutions. An example of the error calculations can be found in Example A1.

45

$$\frac{1.91 \left(^{mg}/_L\right) \div [\, 112.414 \left(^g/_{mol}\right) \times 1000 \left(^{mg}/_g\right)]}{1.33 \left(^{mg}/_L\right) \div [\, 78.971 \left(^g/_{mol}\right) \times 1000 \left(^{mg}/_g\right)]} = 1.01 \; Cd\!:\!Se \quad (3.1)$$
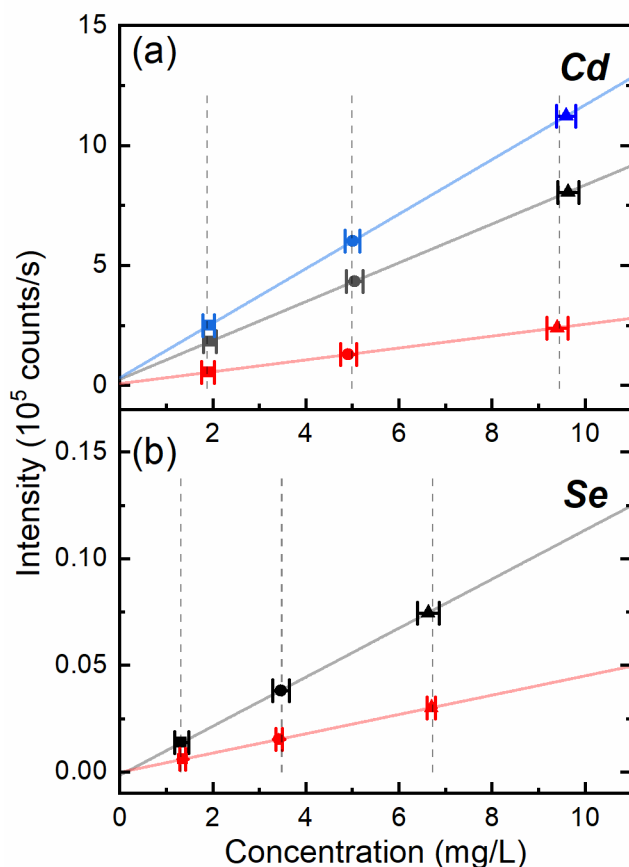
Figure 3.1 ICP-OES calibration lines and data collected from the analysis of {CdSe[*n*-octylamine]$_{0.53}$} QBs. (a) calibration lines and experimental data points for Cd analyses at the wavelengths 214.438 (red), 226.502 (blue), and 228.802 nm (black); (b) calibration lines and experimental data points for Se analyses at the wavelengths 196.026 (black) and 203.985 nm (red). The dotted lines are averages of the data points at each concentration.

3.4 Safety

Appropriate safety practices for handling strong acids (HNO$_3$) and oxidizing agents (H$_2$O$_2$) should be observed.[34] High concentrations of nitric acid and hydrogen peroxide in combination may react violently, producing heat and large volumes of NO$_x$ gas.[35-36] The concentrations used in the digestion procedure here are in the safe range given in Ref. 29, and we

have observed that the combination HNO_3 and H_2O_2 solutions employed here in the absence of analyte produces only mild bubbling for less than a minute. The safest order of combination is the addition of HNO_3 (aq) to H_2O_2 (aq),[35] as our procedure does.

Appropriate safety practices for working with nanomaterials[37] and toxic gases[34] should be observed. Particles smaller than 200 nm readily aerosolize when dry. Sample digestion in HNO_3/H_2O_2 may produce volatile, toxic gases such as H_2Se and SO_2. Working in a fume hood with proper personal protective equipment mitigates the risk of exposure to both aerosolized and volatile material.

The generation of gas pressure in closed (capped) centrifuge tubes poses a potential problem. The digestion procedure employed here generates sufficient gas pressure to distend a rubber septum cap under the conditions described. The use of HDPE centrifuge tubes mitigates the risks associated with glass, however, caution is advised.[33] HDPE and polypropylene centrifuge tubes are incompatible with toluene and several other aromatic and non-aromatic hydrocarbon solvents.[33] The nanocrystals must be suspended in a compatible solvent like isopropyl alcohol, methanol or ethanol before transferring them to the HDPE centrifuge tube. If the structure of the tube is weakened due to contact with incompatible solvents, the accumulating pressure from the production of gases becomes a more significant risk. We have not encountered any problems related to over-pressurization using the methods described.

3.5   Results and Discussion

3.5.1   Selection of Standards, Wavelength Selection, and Construction of the Calibration Line

Experiments were conducted using both multi-element and single-element standard solutions. The advantages of multi-element standards include user convenience, cost savings, and avoidance of error associated with multiple additions to create a custom multi-element standard. However, spectral overlaps (of emission lines) constitute a disadvantage to the use of multi-element standards. Cd and As are often present together in commercial multi-element standards, despite the overlap of their emission lines at 228.802 and 228.812 nm, as shown in Figure 2a. If such a multi-element calibration standard is used, the 228.802 nm line should not be employed for the calibration of Cd due to this overlap.

Caution must also be taken when *combining* multi-element standards, because of the potential for creating spectrally overlapping emission lines (also referred to here as "spectral overlaps"). For example, multi-element standards containing both Cd and Te are not to our knowledge commercially available. Multi-element standards containing Te tend to also contain Pt. The combination of such multi-element standards containing Cd and Te generates a spectral overlap of Cd and Pt emission lines near 214.438 nm (Figure 2b). Thus, one could not use the 214.438 nm line to calibrate for Cd concentration with this combination of standard solutions. The emission lines typically used for determination of elements in semiconductor nanocrystals, and their potential spectral overlaps, are listed in Table 1.
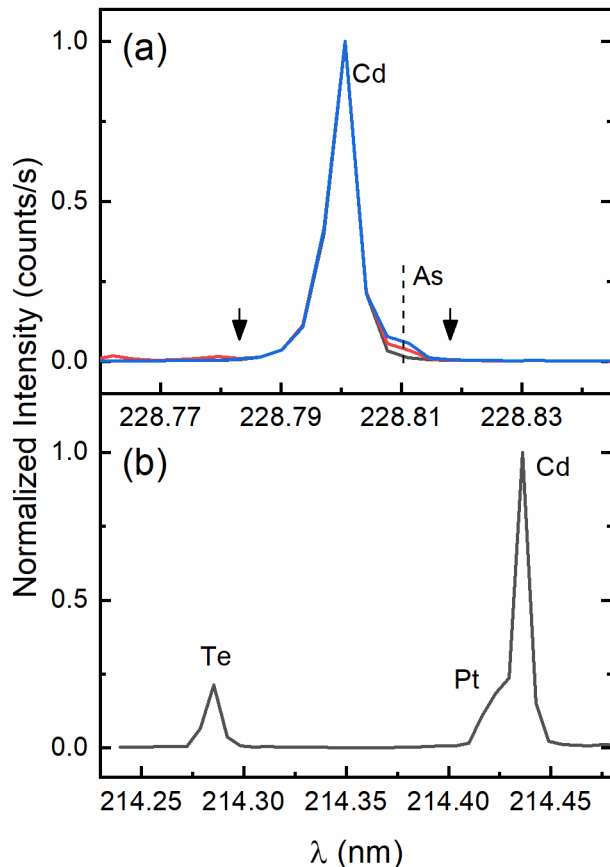
Figure 3.2 (a) Demonstration of the overlap of the Cd emission at 228.802 nm with the As emission at 228.810 nm (marked by the dotted line). The integration limits are shown by the black arrows ($\pm$ 3.5$\times$ the FWHM of the peak). The black spectrum corresponds to a single-element Cd standard. The red spectrum corresponds to a multi-element standard having a 1:1 As/Cd ratio (in mg/L units). The blue spectrum corresponds to a multi-element standard having a 2:1 As/Cd ratio (in mg/L units). Integration of the Cd emission at 228.802 nm in the multi-element standard would result in an over-estimation of Cd by 4% and 6%, respectively. (b) Overlap of Pt and Cd emission lines near 214.438 nm, resulting from the combination of multi-element calibration standards.

The specific emission lines utilized depend, in part, on the use of commercial or custom multi-element calibration solutions. We ultimately prepared custom multi-element calibration solutions from single-element standards to avoid spectral overlaps. The Cd emission line at 228.802 nm is generally regarded as reliable for analyses; its high sensitivity allows for detection of ultra-dilute concentrations.[26] Comparison of the concentrations obtained using different emission lines, such as 214.438 nm and 228.802 nm for Cd, afforded a check on the analytical

49

results. In the absence of spectral overlaps, the concentrations found from both lines, (measured simultaneously), were within error the same. Note that the determination of apparently different concentrations from two emission lines may indicate the presence of an overlapping line at one or both wavelengths.

Table 3.1 Commonly Used Emission Lines for Semiconductor Elements, and Elements with Potential Overlapping Emission Lines.[a]

Element	Emission λ (nm)[38-39]	Elements Producing Potential Overlapping Emission Lines
Al	394.401	U, Ce
	396.152	Mo, Zr, Ce
	167.078	Fe
As	189.042	Cr
	193.696	Ve, Ge
	228.812	Cd, Pt, Ir, Co
Cd	214.438	Pt, Ir
	226.502	Ir
	228.802	Co, Ir, As, Pt
Ge	164.919	Co, Fe, Cu
	219.871	W, Ir, Re, Co
	265.117	Ir, Re
In	158.583	
	230.606	Ni, Os
	325.609	Ir, Re
P	178.287	I
	177.495	Cu, Hf,
	213.618	Cu, Mo
Pb	220.353	Bi, Nb
	217.000	W, Ir, Hf, Sb, Th
S	166.669	Si, B
	180.669	
	181.975	
	182.563	
	189.965	Sn
Se	196.026	Fe
	203.985	Sb, Ir, Cr, Ta
Sn	189.927	S
	242.170	W, Mo, Rh, Ta, Co
Te	170.000	Sn
	214.281	Ta, Re, V
	225.902	Ir, Os, W, Ga, Ru, Ta
	238.578	Os
Zn	213.856	Ni, Cu, V
	202.548	Nb, Cu, Co, Hf
	206.200	Sb, Ta, Bi, Os
	330.258	Na, Bi, Zr
	334.501	Zr, W

[a]Emission wavelengths and potential overlapping emission lines compiled from Refs. 31 and 32.

We used the emission line at 196.026 nm for Se analyses, although the emission at 203.985 nm was equally usable (Table 1). Zn has five commonly used emission lines; we chose the emission at 206.200 nm for Zn analyses to optimize sensitivity and linearity. In our experience, the S emission lines at 180.669, 181.975, and 182.563 nm are all suitable for analyses. The S emission at 189.965 nm is too weak for reliable analyses at the concentrations necessary for accurate determinations of Cd and Zn. We used the emission lines at 214.281 and 238.578 nm for Te.

Experiments were conducted to investigate the proper construction of calibration lines. The multi-element calibration standard used above, having Cd, Se, Pb, and Zn at 1000 mg/L, was employed to prepare standard solutions at 1 mg/L, 5 mg/L, 10 mg/L, 25 mg/L, and 50 mg/L. Figure 3 below plots the optical-emission intensities for Cd (at 228.802 nm), Zn (at 206.200 nm), and Pb (at 220.353 nm). While the data for Zn and Pb were linear over this range, the Cd data significantly deviated from linearity.
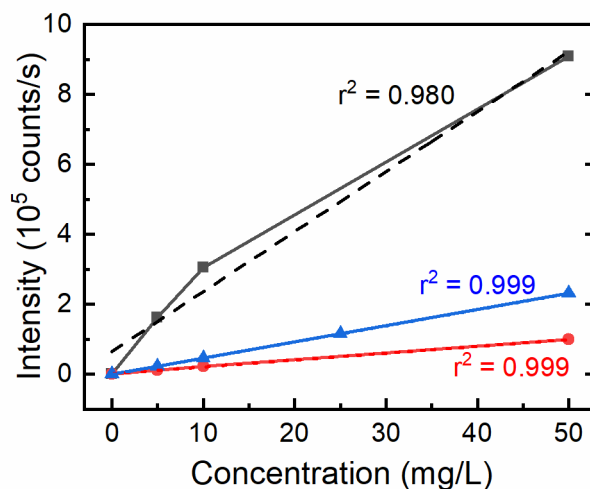
Figure 3.3 Comparison of optical-emission data for Cd (at 228.802 nm, black squares), Zn (at 206.200 nm, red circles), and Pb (at 220.353 nm, blue triangles) over a concentration range of 0-50 mg/L. The solid lines are point-to-point linear segments; the dotted lines (evident only for Cd data) are linear fits to all of the points for each set.

With current instrumentation, users may obtain calibration lines without actual inspection of the data. Use of the linear fit to the Cd data in Figure 3 as a calibration line would lead to errors in determined concentrations as large as 18% (at 25 mg/L). Calibration data may be fit with non-linear functions; however, training protocols and software packages vary. Non-expert users will likely find the use of linear calibration fits to be most convenient. This example emphasizes the importance of plotting and inspecting the calibration data at the outset of any experiment.
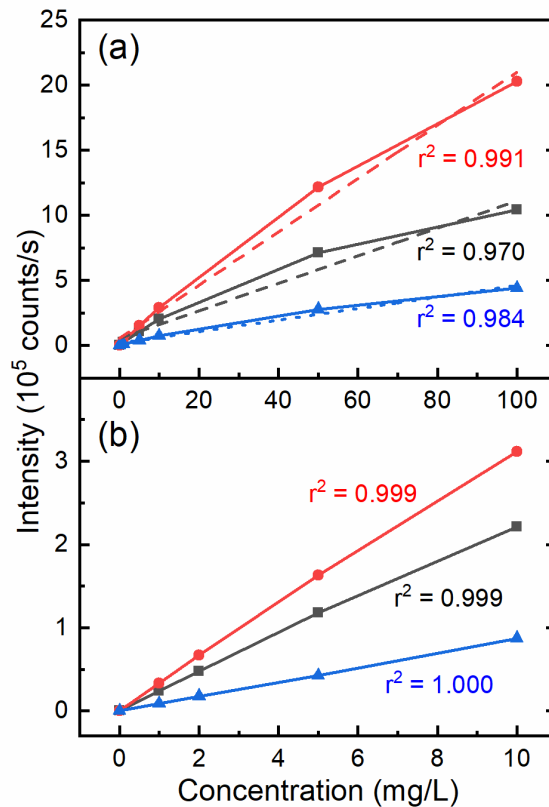
Figure 3.4 Comparison of optical-emission data for Cd at three wavelengths. (a) Emission intensity from Cd at 214.438 nm (blue), 226.502 nm (red), and 228.802 nm (black), over a concentration range of 0-100 mg/L. The linear fits of these data do not produce a satisfactory calibration line. (b) Emission intensity from cadmium at 214.438 nm (blue), 226.502 nm (red), and 228.802 nm (black), over a concentration range of 0-10 mg/L. The solid lines are point-to-point linear segments; the dotted lines are linear fits to all of the points for each set. These linear fits of these data produce a satisfactory calibration line. Errors of the linear fit of 4(b) are described in Figure A3 in Appendix A.

Additional emission data for Cd collected at three wavelengths are compared in Figure 3. Over the concentration range of 0-100 mg/L (Figure 4a), the data for all three wavelengths, 214.438, 226.502, and 228.802 nm, were nonlinear. However, the data over the lower concentration range of 0-10 mg/L were linear. The results underscore the value of conducting analyses at low concentrations near 10 mg/L. Strong emission lines tend to exhibit nonlinearities in emission intensities at higher concentrations.[26]

The utmost care should be taken in preparation of calibration solutions. Generally, a minimum of 3 (preferably 5) calibration standards should be used per order of magnitude.[26] If the concentration range of samples cannot be estimated in advance of analysis, calibration solutions should be prepared in concentrations scaled by orders of magnitude. With concentration ranges of samples better defined, 3-5 calibration solutions should be prepared with evenly spaced concentrations (5, 10, 15, 20 mg/L, for example). For preparation of calibration solutions within such a narrow concentration range, a single pipette should be used to deliver aliquots of the commercial standard to ensure precision and reproducibility. Calibration solutions over a range of concentrations are sometimes prepared by serial dilutions, which, however, does not higher ensure accuracy than preparing solutions over a concentration range by individual dilutions.[26]

3.5.2   Optimization of Materials and Methods

A series of analyses were conducted on a single synthetic batch of {CdSe[n-octylamine]$_{0.53}$} QBs to establish best practices. This material was selected for its stoichiometric wurtzite nanocrystal core having a Cd/Se ratio of unity.[5] Various digestion procedures were conducted in glass and HDPE centrifuge tubes, with the tubes either open or closed during digestion and thereafter. The Cd and Se concentrations in analyte solutions were adjusted to <

10 mg/L, within the linear range for both. Calibration data and experimental measurements were obtained from the emission lines at 228.802 nm for Cd, and 196.026 nm for Se. The results determined from the different conditions employed are given in Table 2 and Figure 5, and are reported as Cd/Se ratios obtained by the analyses, and as deviations from the expected ratio of unity.
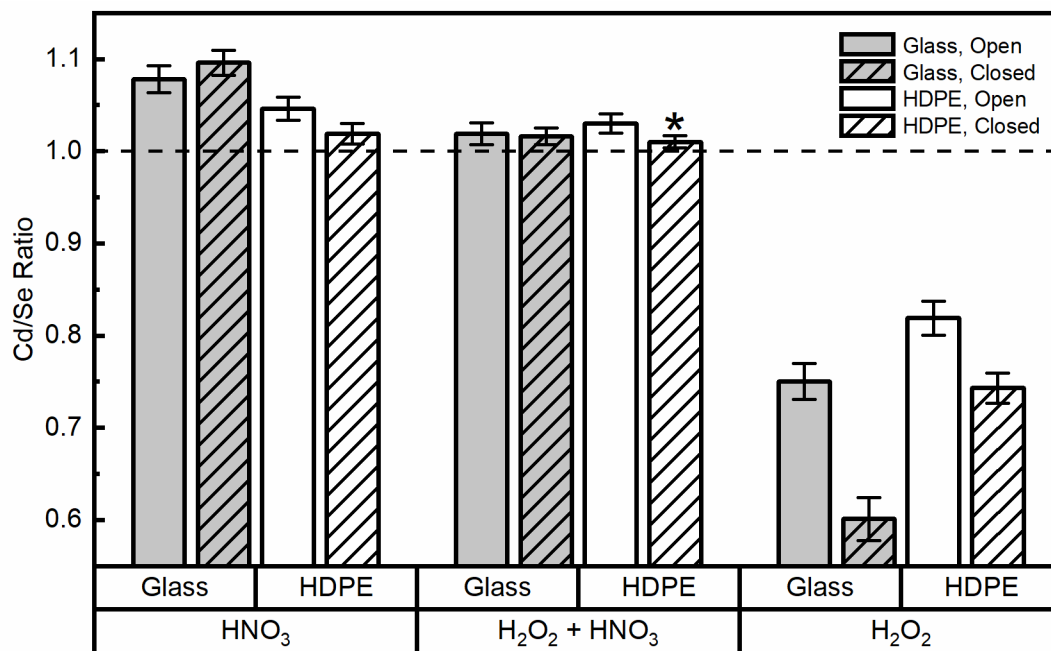
Figure 3.5 Analytical results reported as Cd/Se ratios obtained from various digestion procedures using {CdSe[n-octylamine]$_{0.53}$} quantum belts from a single synthetic batch. The dashed line is at the expected Cd/Se ratio of unity. The optimal conditions and result are marked by an asterisk. The error bars are plus and minus one standard deviation of the analytical trials.

The data in Table 2 and Figure 5 establish that generally better results (closer to the expected value of 1) were obtained using HDPE than borosilicate (glass) digestion tubes, especially in closed tubes (with HNO_3 or H_2O_2/HNO_3 as digestion agents). The Cd/Se ratios were closer to the theoretical value of unity in HDPE. Because many elements adsorb to the surface of borosilicate glass, Nölte[26] recommends against the use of glass in any phase of the analysis. HDPE and/or PP centrifuge tubes are suitable choices during the digestion phase; both

materials are resistant to the strong acids and oxidizers used for digestion. It is important to note that HDPE and PP centrifuge tubes are not compatible with all organic solvents.[33] Methanol, ethanol, or isopropanol are good choices for the suspension of nanocrystals for their transfer to the plastic centrifuge tubes.

Table 3.2 Analytical results reported as Cd/Se ratios obtained from various digestion procedures using {CdSe[*n*-octylamine]$_{0.53}$} QBs from a single synthetic batch. The percent deviations from the expected value of unity are given in parentheses.

Digestion Agent(s)	HDPE Centrifuge Tube		Borosilicate Glass Test Tube	
	Open	Closed	Open	Closed
HNO_3	1.046 (4.57%)	1.019 (1.88%)	1.078 (7.84%)	1.096 (9.55%)
H_2O_2/HNO_3	1.030 (3.03%)	1.010 (1.00%)	1.019 (1.94%)	1.016 (1.57%)
H_2O_2	0.819 (-18.05%)	0.743 (-25.67%)	0.750 (-25.40%)	0.601 (39.87%)

When the digestions were conducted in HDPE centrifuge tubes, better results (Table 2, Figure 5) were obtained in closed tubes (with HNO_3 or H_2O_2/HNO_3 as digestion agents). Semiconductors that generate volatile hydrides, such as H_2S and H_2Se, in contact with acid are prone to loss of these elements during digestion.[26] Such loss leads to the determination of M/S(e) ratios that are higher than those in the analytes, and thus to incorrect analytical results. We surmise that similar problems may attend analyses of III-V semiconductors for which digestion may produce PH_3 or AsH_3. Conducting the digestions in closed containers increases the probability of retention of the volatile species for their oxidation to less volatile solutes. We note that some oxidation products such as SO_2 retain volatility, and so the digestion and analyte solutions should remain in closed containers prior to analyses, which should be completed on the same day. One may also fill the tubes containing analyte solutions such that minimal head space remains open.

Cd/Se ratios were also measured as a function of the digestion agent used. Digestion by HNO_3 in closed, HDPE tubes gave Cd/Se ratios close to the expected value (Table 2, Figure 5).

However, similar HNO_3 digestions conducted in borosilicate glass produced larger deviations. Digestions conducted with both H_2O_2 and HNO_3 by the procedure described above gave better results under all circumstances. The use of H_2O_2/HNO_3 in closed HDPE tubes gave the Cd/Se ratio closest to the theoretical and known[5] value of unity for {CdSe[n-octylamine]$_{0.53}$} QBs.

Analyses were also conducted using H_2O_2 as the sole digestion agent, for comparison (Table 2, Figure 5). Such digestion is sometimes employed in analyses of biological materials.[40] However, sole use of H_2O_2 for digestion of our samples resulted very low apparent Cd/Se ratios, indicative of incomplete digestion.

Strong acids such as aqua regia, nitric acid, and concentrated hydrochloric acid are frequently employed for sample digestion prior to ICP-OES analyses.[7, 40] As indicated above, the formation of volatile compounds during digestion can compromise accuracy.[26, 40] Pre-oxidizing the analyte with H_2O_2 presumably mitigates the formation of H_2S and H_2Se upon addition of HNO_3. The use of an oxidation agent may also promote oxidation by increasing the oxidative power of HNO_3.[41] We selected H_2O_2 because it is a strong oxidizer in acidic solution,[36, 41] and because high-purity, trace-metal grade >30% H_2O_2 is readily available commercially.

3.5.3   Results from Experimental Specimens

ICP-OES analyses were conducted on several additional specimens from our research program using the optimized procedure described above. The M/E ratios (M = Cd, Zn; E = S, Se, Te, Te + Se, or Te + S) in the specimens selected were determined from other analytical measurements, and from theoretical arguments. Four of the specimens were semiconductor nanocrystals, one was a magic-size nanocluster, and one was a molecular compound. The results are summarized in Table 3.

Table 3.3 M/E Ratios Determined by Optimized ICP-OES and Other Methods.

Specimen	M/E^a ratio from ICP-OES^b	M/E^a ratio from other measurements^c	Theoretical
{CdSe[*n*-octylamine]$_{0.53}$} QBs	1.00±0.02	1.05±0.02[42]	1[5]
{CdSe[Cd(oleate)$_2$]$_{0.19}$} QBs	1.27±0.02	1.19±0.02,[5] 1.21±0.02[42]	1.26[5]
{CdTe$_{0.50}$Se$_{0.50}$[oleylamine]$_x$} QPs	0.98±0.01	1.02±0.07	1[43]
{CdTe$_{0.73}$S$_{0.27}$[oleylamine]$_z$} QPs	1.05±0.02	0.95±0.06	1[43]
[(CdSe)$_{13}$(*n*-PrNH$_2$)$_{13}$] Cluster	1.00±0.01	1.11^d	1[44]
Zn(S$_2$CNEt$_2$)$_2$	0.26±0.02	0.25[45]	0.25

^{a}M=Cd or Zn; E = S, Se, Te, Te + Se, or Te + S.
^{b}The error reported is the propagated error.
^{c}The values are the average ± one standard deviation based on repeated measurements.
^{d}Measurement performed on the analog [(CdSe)$_{13}$(*n*-octylamine)$_{13}$] nanocluster.

The first two specimens in Table 3 are variously ligated CdSe QBs.[5] The wurtzite nanocrystal cores of the {CdSe[*n*-octylamine]$_{0.53}$} QBs are precisely stoichiometric with Cd/Se ratios of unity, as required by the lack of anions in the empirical formula determined by combustion-based elemental analyses.[5] The average ratio of 1.05 ± 0.02 was determined by repeated energy-dispersive X-ray spectroscopy (EDS) measurements, with a range determined by the standard deviation of those measurements.[42] The ratio of 1.00 ± 0.02 determined by the optimized ICP-OES procedure was very close to the expected, theoretical value of unity. In this case, the error has been propagated through each step of the analysis and includes multiple measurements.

In the second specimen, the L-type *n*-octylamine ligands on the surface of the {CdSe[*n*-octylamine]$_{0.53}$} QBs were exchanged by Z-type Cd(oleate)$_2$ ligands to give {CdSe[Cd(oleate)$_2$]$_{0.19}$} QBs. As this exchange adds additional Cd atoms to the surface of the quantum belts, the Cd/Se ratio becomes greater than one. The theoretical ratio of 1.26 is the value achieved by coordinating one Cd(oleate)$_2$ ligand per 3-coordinate surface Se atom.[12] The values derived from combustion-based elemental analysis, 1.19 ± 0.02, and EDS, 1.21 ± 0.02,

were slightly below the theoretical ratio. The value obtained by the optimized ICP-OES procedure, 1.27 ± 0.02, was in agreement with theory.

The third and fourth specimens in Table 3 are core-shell CdTe-CdSe and CdTe-CdS QPs. We determined the Cd/E ratios (E = Te + Se or Te + S) in a prior study by EDS and a non-optimal ICP-OES procedure.[27] Whereas the Cd/E ratios determined by EDS remained close to the expected value of one, those measured by ICP-OES increasingly deviated to larger apparent ratios with increasing CdSe or CdS shell thickness. Additionally, the non-optimized procedure produced Se/Te and S/Te ratios measured by ICP-OES were smaller than those determined by EDS.

The differences in the Cd/E ratios measured by EDS and ICP-OES were in the pattern expected for partial loss of volatile S and Se species during preparation of ICP-OES samples. The digestion procedure employed in the prior study[27] differed from the optimized procedure described here. Analytical samples were first digested by HNO_3, and subsequently by HCl in closed, polytetrafluoroethylene containers. Here we analyzed comparable core-shell CdTe-CdSe and CdTe-CdS nanoplatelets using the optimized procedure.

The results of these new analyses are recorded in Table 3. The Cd/E ratios determined by EDS, 1.02 ± 0.07, and ICP-OES, 0.98 ± 0.01, for $\{CdTe_{0.50}Se_{0.50}[oleylamine]_x\}$ were the same within experimental error. Those determined by EDS, 0.95 ± 0.06, and ICP-OES, 1.05 ± 0.02, for $\{CdTe_{0.73}S_{0.27}[oleylamine]_z\}$ may have differed by more than the error in the analyses. The EDS ratio of 0.95 seemed too low, and the ICP-OES ratio of 1.05 seemed too high, given the expected ratio of 1. The empirical formula (and therefore absence of acetate) was not established by combustion-based elemental analysis in this case,[27] and we entertain the possibility that these nanoplatelets may contain excess Cd.

Further validation for the optimized ICP-OES procedure was obtained by comparison of

ε/Te ratios (ε = S or Se) by ICP-OES using the optimized procedure here, and for comparable

samples analyzed previously[27] by a non-optimal ICP-OES method and EDS (Table 4). In the

prior study, the ε/Te ratios measured by ICP-OES were always *smaller* than those measured by

EDS, suggesting volatilization of S and Se during ICP-OES analysis. Here the Se/Te ratio

determined by ICP-OES, 1.00 $\pm$ 0.01, for {CdTe$_{0.50}$Se$_{0.50}$[oleylamine]$_x$} was larger than that

previously determined for a comparable sample, 0.84, error unavailable. Although the ICP-OES

ratio measured here differed from the corresponding Se/Te ratios measured by EDS (Table 4),

the values were within experimental error. Here, the S/Te ratio determined by ICP-OES, 0.39 $\pm$

0.03, for {CdTe$_{0.73}$S$_{0.27}$[oleylamine]$_z$} QPs was larger than that previously determined for a

comparable sample, 0.24, error unavailable, and in close agreement with the values determined

by EDS (Table 4). Among the four ratios determined for each of the two specimens, only the

ratios measured previously by a non-optimal ICP-OES analysis differed by more than

experimental error. The results establish that the optimized ICP-OES methods described here

gave more reliable values, and that loss of volatile S and Se species during analysis is the likely

cause of the deviation.

Table 3.4 ε/Te Ratios (ε = Se or S) Determined by ICP-OES and EDS in CdTe-Cdε Core-Shell QPs.

Specimen	ε/Te ratio from optimized ICP-OES analysis[a]	ε/Te ratio from prior ICP-OES analysis[27]	ε/Te ratio from current EDS analysis[c]	ε/Te ratio from prior EDS analysis[27,c]
{CdTe$_{0.50}$Se$_{0.50}$[oleylamine]$_x$}	1.00 $\pm$ 0.01	0.84[b]	0.91 $\pm$ 0.09	0.91 $\pm$ 0.06
{CdTe$_{0.73}$S$_{0.27}$[oleylamine]$_z$}	0.39 $\pm$ 0.03	0.24[b]	0.35 $\pm$ 0.05	0.32 $\pm$ 0.04

[a]The error reported is the propagated error.
[b]Error unavailable.
[c]The range is one standard deviation of repeated measurements.

Although the emphasis here is on analyses of semiconductor nanocrystals, we included

two molecular compounds for comparison, also listed in Table 3. These were analyzed using the

optimized ICP-OES procedure. The first is the magic-size-nanocluster $[(CdSe)_{13}(n\text{-}PrNH_2)_{13}]$.[32]

Here the theoretical or expected Cd/Se ratio of one is established by the lack of anions in the

empirical formula, as determined by combustion-based elemental analysis, and theoretical

calculations.[46] Rutherford backscattering gave a Cd/Se ratio of 1.11 (error unavailable) for the

analog $[(CdSe)_{13}(n\text{-}octylNH_2)_{13}]$, and laser-induced-ionization mass spectrometry on this

derivative identified the nanocluster core stoichiometry as $(CdSe)_{13}$.[44] Here, ICP-OES analysis

of $[(CdSe)_{13}(n\text{-}PrNH_2)_{13}]$ found a Cd/Se ratio of 1.00 ± 0.01, confirming expectation.

Finally, the molecular dithiocarbamate complex $Zn(S_2CNEt_2)_2$ was analyzed. The

theoretical or expected Zn/S ratio of 0.25 was obtained from the empirical formula determined

by elemental analysis, and x-ray crystallography.[45] The ratio of 0.26 ± 0.02 determined by ICP-

OES matched the expected value.

3.6   Conclusions

Herein we have provided methods and procedures for accurate determination of the

composition of semiconductor nanocrystals via ICP-OES. In general terms, we recommend

sample digestion in closed, HDPE containers using H_2O_2 and HNO_3 solutions in sequence. We

also advise care in construction of calibration lines, and attention to potential spectral overlaps.

We also remind researchers that ICP-OES measurements are obtained in units of mg/L (mg/L),

which must be converted to molarities to determine molar ratios (Eq 1). In our experience, if

unexpectedly *low* M/E ratios are determined when compared to other measurements or

theoretical calculations, the digestion process is likely incomplete, and the fraction of HNO_3

should be carefully increased. If unexpectedly *high* M/E ratios are determined, the nonmetallic

element E is likely depleted by volatilization. Although we have studied only materials and

compounds corresponding to groups II and VI, we expect the methods detailed here to be more broadly applicable.

Associated Content can be found in Appendix A.

3.7   References

1.   Morrison, C.; Sun, H.; Yao, Y.; Loomis, R. A.; Buhro, W. E., Methods for the ICP-OES Analysis of Semiconductor Materials. *Chem. Mater.* **2020,** *32* (5), 1760-1768.

2.   Taylor, J.; Kippeny, T.; Rosenthal, S. J., Surface Stoichiometry of CdSe Nanocrystals Determined by Rutherford Backscattering Spectroscopy. *J. Cluster Sci.* **2001,** *12* (4), 571-582.

3.   Anderson, N. C.; Hendricks, M. P.; Choi, J. J.; Owen, J. S., Ligand Exchange and the Stoichiometry of Metal Chalcogenide Nanocrystals: Spectroscopic Observation of Facile Metal-Carboxylate Displacement and Binding. *J. Am. Chem. Soc.* **2013,** *135* (49), 18536-18548.

4.   Moreels, I.; Lambert, K.; De Muynck, D.; Vanhaecke, F.; Poelman, D.; Martins, J. C.; Allan, G.; Hens, Z., Composition and Size-Dependent Extinction Coefficient of Colloidal PbSe Quantum Dots. *Chem. Mater.* **2007,** *19* (25), 6101-6106.

5.   Zhou, Y.; Wang, F.; Buhro, W. E., Large Exciton Energy Shifts by Reversible Surface Exchange in 2D II–VI Nanocrystals. *J. Am. Chem. Soc.* **2015,** *137* (48), 15198-15208.

6.   Luther, J. M.; Pietryga, J. M., Stoichiometry Control in Quantum Dots: A Viable Analog to Impurity Doping of Bulk Materials. *ACS Nano* **2013,** *7* (3), 1845-1849.

7.   Morris-Cohen, A. J.; Donakowski, M. D.; Knowles, K. E.; Weiss, E. A., The Effect of a Common Purification Procedure on the Chemical Composition of the Surfaces of CdSe Quantum Dots Synthesized with Trioctylphosphine Oxide. *J. Phys. Chem. C* **2010,** *114* (2), 897-906.

8.   Katari, J. E. B.; Colvin, V. L.; Alivisatos, A. P., X-ray Photoelectron Spectroscopy of CdSe Nanocrystals with Applications to Studies of the Nanocrystal Surface. *J. Phys. Chem.* **1994,** *98* (15), 4109-4117.

9.   Voznyy, O.; Zhitomirsky, D.; Stadler, P.; Ning, Z.; Hoogland, S.; Sargent, E. H., A Charge-Orbital Balance Picture of Doping in Colloidal Quantum Dot Solids. *ACS Nano* **2012,** *6* (9), 8448-8455.

10.   Jasieniak, J.; Mulvaney, P., From Cd-Rich to Se-Rich − the Manipulation of CdSe Nanocrystal Surface Stoichiometry. *J. Am. Chem. Soc.* **2007,** *129* (10), 2841-2848.

11.   Peng, Z. A.; Peng, X., Nearly Monodisperse and Shape-Controlled CdSe Nanocrystals via Alternative Routes: Nucleation and Growth. *J. Am. Chem. Soc.* **2002,** *124* (13), 3343-3353.

12.   Underwood, D. F.; Kippeny, T.; Rosenthal, S. J., Ultrafast Carrier Dynamics in CdSe Nanocrystals Determined by Femtosecond Fluorescence Upconversion Spectroscopy. *J. Phys. Chem. B* **2001,** *105* (2), 436-443.

13.   Anderson, N. C.; Owen, J. S., Soluble, Chloride-Terminated CdSe Nanocrystals: Ligand Exchange Monitored by ^{1}H and ^{31}P NMR Spectroscopy. *Chem. Mater.* **2013,** *25* (1), 69-76.

14.   Fritzinger, B.; Capek, R. K.; Lambert, K.; Martins, J. C.; Hens, Z., Utilizing Self-Exchange To Address the Binding of Carboxylic Acid Ligands to CdSe Quantum Dots. *J. Am. Chem. Soc.* **2010,** *132* (29), 10195-10201.

15.   Dai, Q.; Wang, Y.; Li, X.; Zhang, Y.; Pellegrino, D. J.; Zhao, M.; Zou, B.; Seo, J.; Wang, Y.; Yu, W. W., Size-Dependent Composition and Molar Extinction Coefficient of PbSe Semiconductor Nanocrystals. *ACS Nano* **2009,** *3* (6), 1518-1524.

16.   Yeltik, A.; Delikanli, S.; Olutas, M.; Kelestemur, Y.; Guzelturk, B.; Demir, H. V., Experimental Determination of the Absorption Cross-Section and Molar Extinction Coefficient of Colloidal CdSe Nanoplatelets. *J. Phys. Chem. C* **2015,** *119* (47), 26768-26775.

17.   Montoro Bustos, A. R.; Encinar, J. R.; Fernández-Argüelles, M. T.; Costa-Fernández, J. M.; Sanz-Medel, A., Elemental Mass Spectrometry: a Powerful Tool for an Accurate Characterisation at Elemental Level of Quantum Dots. *Chem. Commun.* **2009,** (21), 3107-3109.

18.   Hughes, B. K.; Ruddy, D. A.; Blackburn, J. L.; Smith, D. K.; Bergren, M. R.; Nozik, A. J.; Johnson, J. C.; Beard, M. C., Control of PbSe Quantum Dot Surface Chemistry and Photophysics Using an Alkylselenide Ligand. *ACS Nano* **2012,** *6* (6), 5498-5506.

19.   Morris-Cohen, A. J.; Frederick, M. T.; Lilly, G. D.; McArthur, E. A.; Weiss, E. A., Organic Surfactant-Controlled Composition of the Surfaces of CdSe Quantum Dots. *J. Phys. Chem. Lett.* **2010,** *1* (7), 1078-1081.

20.   Wilcoxon, J. P.; Provencio, P. P., Chemical and Optical Properties of CdSe and CdSe/ZnS Nanocrystals Investigated Using High-Performance Liquid Chromatography. *J. Phys. Chem. B* **2005,** *109* (28), 13461-13471.

21.   Hoye, R. L. Z.; Brandt, R. E.; Osherov, A.; Stevanović, V.; Stranks, S. D.; Wilson, M. W. B.; Kim, H.; Akey, A. J.; Perkins, J. D.; Kurchin, R. C.; Poindexter, J. R.; Wang, E. N.; Bawendi, M. G.; Bulović, V.; Buonassisi, T., Methylammonium Bismuth Iodide as a Lead-Free, Stable Hybrid Organic–Inorganic Solar Absorber. *Chem. Eur. J.* **2016,** *22* (8), 2605-2610.

22.   Hoye, R. L. Z.; Schulz, P.; Schelhas, L. T.; Holder, A. M.; Stone, K. H.; Perkins, J. D.; Vigil-Fowler, D.; Siol, S.; Scanlon, D. O.; Zakutayev, A.; Walsh, A.; Smith, I. C.; Melot, B. C.; Kurchin, R. C.; Wang, Y.; Shi, J.; Marques, F. C.; Berry, J. J.; Tumas, W.; Lany, S.; Stevanović, V.; Toney, M. F.; Buonassisi, T., Perovskite-Inspired Photovoltaic Materials: Toward Best Practices in Materials Characterization and Calculations. *Chem. Mater.* **2017,** *29* (5), 1964-1988.

23.   Saparov, B.; Hong, F.; Sun, J.-P.; Duan, H.-S.; Meng, W.; Cameron, S.; Hill, I. G.; Yan, Y.; Mitzi, D. B., Thin-Film Preparation and Characterization of $Cs_3Sb_2I_9$: A Lead-Free Layered Perovskite Semiconductor. *Chem. Mater.* **2015,** *27* (16), 5622-5632.

24.   *XRF Data Differences: Quantitative, Semi-quantitative, and Qualitative data.* https://www.bruker.com/products/x-ray-diffraction-and-elemental-analysis/handheld-xrf/xrf-data-primer-quantitative-semi-quantitative-qualitative.html. (accessed July 5, 2019).

25.   Chen, P. E.; Anderson, N. C.; Norman, Z. M.; Owen, J. S., Tight Binding of Carboxylate, Phosphonate, and Carbamate Anions to Stoichiometric CdSe Nanocrystals. *J. Am. Chem. Soc.* **2017,** *139* (8), 3227-3236.

26.   Nölte, J., *ICP Emission Spectrometry: A Practical Guide*. Wiley-VCH Verlag GmbH & Co, KGaA Weinheim, Germany, 2003.

27.   Sun, H.; Buhro, W. E., Core–Shell Cadmium Telluride Quantum Platelets with Absorptions Spanning the Visible Spectrum. *ACS Nano* **2019,** *13* (6), 6982-6991.

28.   Li, Z.; Qin, H.; Guzun, D.; Benamara, M.; Salamo, G.; Peng, X., Uniform Thickness and Colloidal-Stable CdS Quantum Disks with Tunable Thickness: Synthesis and Properties. *Nano Research* **2012,** *5* (5), 337-351.

29.   Cossairt, B. M. University of Washington, Seatle, Washington. Personal Communication, 2019.

30.   Whittaker-Brooks, L. University of Utah, Salt Lake City, Utah. Personal Communication, 2019.

31.   Liu, Y.-H.; Wayman, V. L.; Gibbons, P. C.; Loomis, R. A.; Buhro, W. E., Origin of High Photoluminescence Efficiencies in CdSe Quantum Belts. *Nano Lett.* **2010,** *10* (1), 352-357.

32.   Wang, Y.; Liu, Y.-H.; Zhang, Y.; Kowalski, P. J.; Rohrs, H. W.; Buhro, W. E., Preparation of Primary Amine Derivatives of the Magic-Size Nanocluster (CdSe)13. *Inorg. Chem.* **2013,** *52* (6), 2933-2938.

33.   *Centrifuge Chemical Resistance Table*. Thermo Fisher Scientific. http://tools.thermofisher.com/content/sfs/brochures/D20825.pdf. (accessed June 30, 2019).

34.   *Prudent Practices in the Laboratory: Handling and Management of Chemical Hazards, Updated Version*. National Research Council. The National Academies Press: Washington, DC, 2011; p 360.

35.   *Nitric Acid with Hydrogen Peroxide Reaction Hazards Technical Data Sheet*. Solvay Chemicals Inc. . https://www.solvay.com/. (accessed June 28, 2019).

36.   Hatcher, W. H., MacLauchlan, D. W. , Conductivity Data of Aqueous Mixtures of Hydrogen Peroxide and Nitric Acid. *Can. J. Res. Sec. B.* **1938,** *16* (8), 253-259.

37.   Approaches to Safe Nanotechnology. Department of Health and Human Services, Centers for Disease Control and Prevention, National Institute for Occupational Safety and Health: Washington D.C., Atlanta, GA, Cincinatti, OH, 2009; Vol. 2009-125.

38.   *Interactive Periodic Table*. Inorganic Ventures. https://www.inorganicventures.com/periodic-table. (accessed June 6, 2019).

39.   *Optima Simutaneous Spectrometers Wavelength Tables*. Perkin Elmer Instruments LLC: 2002.

40.   Sah, R. N.; Miller, R. O., Spontaneous Reaction for Acid Dissolution of Biological Tissues in Closed Vessels. *Anal. Chem.* **1992,** *64* (2), 230-233.

41.   Luque de Castro, M. D., Luque García, J. L., *Techniques and Instrumentation in Analytical Chemistry*. Elsevier: Amsterdam, The Netherlands, 2002; Vol. 24.

42.   Yao, Y.; DeKoster, G. T.; Buhro, W. E., Interchange of L-, Z-, and Bound-Ion-Pair X-Type Ligation on Cadmium Selenide Quantum Belts. *Chem. Mater.* **2019,** *31* (11), 4299-4312.

43.   Wang, F.; Wang, Y.; Liu, Y.-H.; Morrison, P. J.; Loomis, R. A.; Buhro, W. E., Two-Dimensional Semiconductor Nanocrystals: Properties, Templated Formation, and Magic-Size Nanocluster Intermediates. *Acc. Chem. Res.* **2015,** *48* (1), 13-21.

44.   Wang, Y.; Liu, Y.-H.; Zhang, Y.; Wang, F.; Kowalski, P. J.; Rohrs, H. W.; Loomis, R. A.; Gross, M. L.; Buhro, W. E., Isolation of the Magic-Size CdSe Nanoclusters [(CdSe)$_{13}$(n-octylamine)$_{13}$] and [(CdSe)$_{13}$(oleylamine)$_{13}$]. *Angew. Chem. Int. Ed.* **2012,** *51* (25), 6154-6157.

45.   Bonamico, M.; Mazzone, G.; Vaciago, A.; Zambonelli, L., Structural Studies of Metal Dithiocarbamates. III. The Crystal and Molecular Structure of Zinc Diethyldithiocarbamate. *Acta Cryst.* **1965,** *19* (6), 898-909.

46.   Nguyen, K. A.; Day, P. N.; Pachter, R., Understanding Structural and Optical Properties of Nanoscale CdSe Magic-Size Quantum Dots: Insight from Computational Prediction. *J. Phys. Chem. C* **2010,** *114* (39), 16197-16209.

Chapter 4: Cadmium Bis(phenyldithiocarbamate) as a Nanocrystal Shell-Growth Precursor

4.1   Introduction

We report the synthesis, crystal structure, spectroscopic characterization, and chemical reactivity of cadmium bis(phenyldithiocarbamate) [Cd(PTC)$_2$]. We find that Cd(PTC)$_2$ is a potent molecular precursor to CdS, and is useful for low-temperature, solution-based CdS-shell deposition on CdSe quantum belts (QBs).[2] The chemical pathway for the conversion of Cd(PTC)$_2$ to CdS is also elucidated here.

We argue herein that CdS shell deposition proceeds after coordination of Cd(PTC)$_2$ to the CdSe QB surfaces. We previously established that the surface coordination chemistry of these CdSe QBs is determined by their wurtzite crystal structure and crystallographic orientation (Figure 1).[3-4] The QBs have top and bottom facets containing equal numbers of Cd and Se atoms, and are hence nonpolar facets. If unreconstructed, these top and bottom facets exhibit a corduroy-like ridge-and-valley structure consisting of parallel, zig-zag, (-Cd-Se-)$_n$ chains (Figure 4.1). The Cd and Se atoms in the valley positions are 4 coordinate and sterically saturated. Those in the ridge positions are 3 coordinate, prior to surface ligation. The long, thin, (left and right) edge facets (Figure 4.1a) are similarly nonpolar, having half of their CdSe units in 4-coordinate valley positions, and half in 3-coordinate ridge positions. The QBs have a discrete thickness of 5 CdSe monolayers (MLs, Figure 4.1a).[4] The

stoichiometries of surface ligand binding is ultimately determined by the discrete thickness

and structural characteristics of these large-area top, bottom, and edge facets.
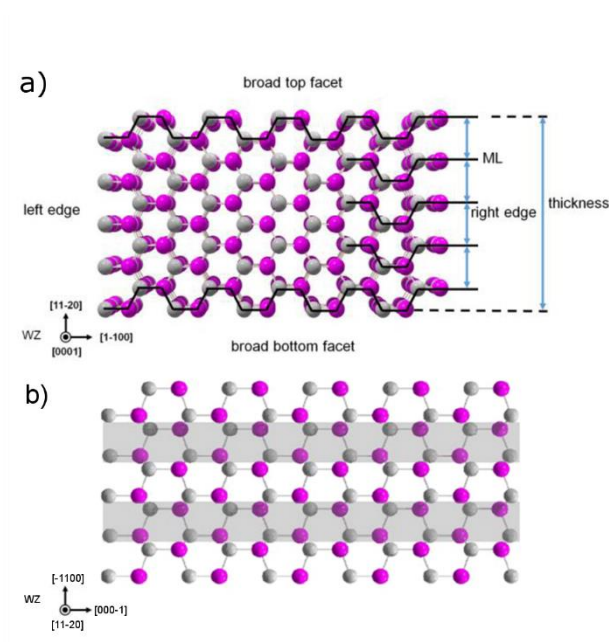
Figure 4.1   The surface coordination chemistry of wurtzite CdSe QBs. Cd and Se atoms
are gray and magenta, respectively. (a) View perpendicular to the small end facet of a QB.
(b) View of a top CdSe QB facet, with the valley positions shaded. Adapted with permission
from Ref. 2. Copyright 2015 American Chemical Society.

As initially synthesized, the wurtzite CdSe QBs employed in this study are ligated

exclusively by *n*-octylamine, or L-type[5] ligation.[3] Elemental analyses established the

empirical formula {CdSe[*n*-octylamine]$_{0.53}$} for these QBs. We previously showed this

formula to be consistent with the bonding of one *n*-octylamine ligand to every surface Cd and

Se atom in a 3-coordinate ridge position, as a normal datively bound Lewis base to the Cd

sites, and as a pseudo-hydrogen-bond donor to the Se sites.[3]

We also showed that the L-type *n*-octylamine ligation was readily, completely, and

reversibly exchanged to Z-type[5] Cd(oleate)$_2$ ligation (Scheme 4.1), in which the Cd(oleate)$_2$

serves as a Lewis acid bound to the CdSe QB surfaces by coordination to Se sites.[3] The

empirical formula established for this Z-type ligation is {CdSe[Cd(oleate)$_2$]$_{0.19}$}, which is

consistent with the bonding of one Cd(oleate)$_2$ molecule per surface Se atom in a 3-

coordinate ridge position. We proposed that the surface-bound Cd atoms in the Cd(oleate)$_2$ ligands bridged adjacent Se atoms on the CdSe QBs.[3] The facility of the Scheme 4.1 L- to Z-type surface-ligation exchange suggested it as a means of installing purposeful surface functionality on the CdSe QBs.

Scheme 4.1   Exchange of L- to Z-Type Surface Ligation on CdSe Quantum Belts.
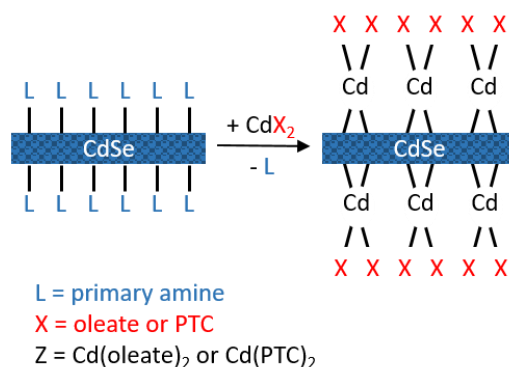
Our interest in Cd(PTC)$_2$ as a potential Z-type (Lewis-acid) ligand was prompted by reports that PTC ligands surface bound to semiconductor nanocrystals effectively delocalize photo-generated carriers into the PTC-ligand layers.[6-12] We considered that the exchange process in Scheme 4.1 may provide a new means for ligating CdSe nanocrystals exclusively with PTC groups. However, under our experimental conditions the reactions of {CdSe[*n*-octylamine]$_{0.53}$} QBs and Cd(PTC)$_2$ were not a simple L-type for Z-type ligand exchange, but rather resulted in the growth of CdS shells on the QBs.

Cadmium bis(dithiocarbamate) compounds have been previously used as solution-phase and gas-phase precursors to CdS powders or nanoparticles,[13-19] and films,[20-21] respectively. Most of these studies have employed dithiocarbamates derived from secondary amines, such as cadmium bis(diethyldithiocarbamate) [Cd(S$_2$CNEt$_2$)$_2$].[19] The compound Cd(PTC)$_2$ was previously prepared, but isolated and characterized as the bipyridine adduct [Cd(PTC)$_2$(bipy)].[22] This adduct was thermally decomposed to CdS nanoparticles. Here we describe the parent compound Cd(PTC)$_2$. We note that octyldithiocarbamate ligands have

71

been employed as thermally degradable surface functionalization for semiconductor nanocrystals in thin films.[23] Although high-temperature thermolyses (140 – 250 °C) of zinc and cadmium bis(dialkyldithiocarbamate) precursors have been used to deposit ZnS[24] and CdS[25-27] shells on CdSe nanocrystals, the low-temperature shell-growth pathway (70 °C) reported here from a mono-substituted dithiocarbamate precursor has not to our knowledge been previously employed.

4.2   Experimental Section

4.2.1   Materials and General Procedures

All experimental procedures were performed under ambient conditions unless otherwise specified. Ammonium phenyldithiocarbamate [NH$_4$][PTC],[12, 28] was synthesized according to literature procedures.

4.2.2   Preparation of Bis(phenyldithiocarbamato) cadmium(II)

The synthesis of bis(phenydithiocarbamato) cadmium(II) (Cd(PTC)$_2$) was adapted from similar literature procedures.[22, 29-34] In brief, a solution of CdCl$_2$ (98 mg, 0.54 mmol) in deionized H$_2$O (40 mL) was added dropwise to a continuously stirred solution of NH$_4$PTC (200 mg, 1.07 mmol) deionized H$_2$O (60 mL). A white precipitate began to form immediately upon addition. The solution was allowed to stir for 30 min. At that time, the precipitate was vacuum filtered and washed with ice-chilled deionized H$_2$O (25 mL), followed by three washes with ice-chilled ethanol (3 × 10 mL). The product Cd(PTC)$_2$, a pale yellow powder, was dried under vacuum (1 h). Yield 0.149 g (33 mmol, 60%). mp 138 °C dec. UV-Visible (THF) λ_{max}, nm: 299. IR, cm^{-1}: 3303 ν(N-H), 3070 ν(=CH), 1586 σ(N-H), ν(C=N), 1586 ν(C=N), 980 ν(C=S) (see Figure S1). ^{1}H NMR (500 MHz, DMSO-d_6, δ) 11.6 (s, 2H); 7.55 (d, J = 7.34 Hz, 4H), 7.35 (t; J = 7.58 Hz, 4H), 7.18 (t, J = 7.34 Hz, 2H).

$^{13}C\{^{1}H\}$ NMR (125 MHz, DMSO-d_6, δ) 208.0, 141.3, 128.4, 125.3, 123.4. Anal. Calcd for

$C_{14}H_{12}CdN_2S_4$: C, 37.46; H, 2.69; N, 6.24; S, 28.57. Found: C, 37.47; H, 2.76; N, 6.20; S,

28.58. All values given as percentages.

4.2.3   X-ray Structure Determination of Cd(PTC)$_2$

Single crystals of Cd(PTC)$_2$ were grown using the vapor-diffusion method. A 20

mmol solution of Cd(PTC)$_2$ in THF was prepared in a small vial, and which was placed

inside a larger, sealable jar containing hexane. The jar was sealed and left undisturbed

overnight. Small, needle-like pale-yellow crystals were obtained, and used for the single-

crystal X-ray structure determination.

A crystal of approximate dimensions 0.60 x 0.12 x 0.08 mm^3 was mounted on a

MiTeGen cryoloop in a random orientation. Preliminary examination and data collection

were performed using a Bruker X8 Kappa Apex II Charge Coupled Device (CCD) Detector

system single-crystal X-Ray diffractometer equipped with an Oxford Cryostream LT device.

All data were collected using graphite monochromated Mo Kα radiation (λ = 0.71073 Å)

from a fine focus sealed tube X-Ray source. Preliminary unit cell constants were determined

with a set of 36 narrow frame scans. Typical data sets consist of combinations of ϖ and ϕ

scan frames with typical scan width of 0.5° and counting time of 10 seconds/frame at a

crystal to detector distance of 4.0 cm. The collected frames were integrated using an

orientation matrix determined from the narrow frame scans. Apex II[35] and SAINT[36] software

packages were used for data collection and data integration. Analysis of the integrated data

did not show any decay. Final cell constants were determined by global refinement of 9861

reflections harvested from the complete data set. Collected data were corrected for

systematic errors using SADABS[37] based on the Laue symmetry using equivalent reflections.

Crystal data and intensity data collection parameters are listed in Table 4.1. Structure solution and refinement were carried out using the SHELXTL- PLUS software package.[38] The structure was solved and refined successfully in the monoclinic space group $P2_1/n$. Full matrix least-squares refinements were carried out by minimizing $\Sigma w(F_O^2-F_c^2)^2$. The non-hydrogen atoms were refined anisotropically to convergence. The N-H H atoms were located and refined with geometrical restraints (SADI). All other hydrogen atoms were treated using an appropriate riding model (AFIX m3). The final residual values and structure refinement parameters are listed in Table 4.1.

Complete listings of positional and isotropic displacement coefficients for hydrogen atoms, and anisotropic displacement coefficients for the non-hydrogen atoms are provided in the Supporting Information (Tables B1 – B4). A table of calculated and observed structure factors are available in electronic format.

Table 4.1. Crystal data and structure refinement for Cd(PTC)₂.

Empirical formula	$C_{18} H_{20} Cd N_2 O S_4$
Formula weight	521.00
Temperature	100(2) K
Wavelength	0.71073 Å
Crystal system	Monoclinic
Space group	$P2_1/n$
Unit cell dimensions	$a = 15.5501(6)$ Å $\quad$ $\alpha = 90°$
	$b = 7.3761(3)$ Å $\quad$ $\beta = 90.915(2)°$
	$c = 17.2620(7)$ Å $\quad$ $\gamma = 90°$
Volume	1979.68(14) Å^3
Z	4
Density (calculated)	1.748 Mg/m^3
Absorption coefficient	1.535 mm^{-1}
F(000)	1048
Crystal size	0.598 x 0.121 x 0.075 mm^3
Theta range for data collection	1.749 to 45.000°
Index ranges	$-28 \leq h \leq 30, -9 \leq k \leq 14, -34 \leq l \leq 34$
Reflections collected	66935
Independent reflections	16292 [R(int) = 0.0464]
Completeness to theta = 25.242°	99.7 %
Absorption correction	Semi-empirical from equivalents
Max. and min. transmission	0.4481 and 0.3434
Refinement method	Full-matrix least-squares on F^2
Data / restraints / parameters	16292 / 1 / 243
Goodness-of-fit on F^2	1.002
Final R indices [I>2sigma(I)]	R1 = 0.0309, wR2 = 0.0554
R indices (all data)	R1 = 0.0583, wR2 = 0.0632
Largest diff. peak and hole	0.914 and -1.026 e.Å^{-3}

4.2.4 Monitoring the Conversion of Cd(PTC)$_2$ to CdS

The degradation products of Cd(PTC)$_2$ were monitored using ^{1}H NMR and ^{13}C{^{1}H} NMR at 50 °C. Cd(PTC)$_2$ (12 mg, 0.003 mmol) was dissolved in DMSO-d_6 (1 g). Spectra were recorded every 60 minutes for 12 hours, until spectral evolution was complete (See Figures B.2 and B.3).

The bright yellow, solid precipitate from the decomposition reaction monitored via NMR was then isolated from the DMSO-d_6 via centrifugation with a benchtop centrifuge, washed three times with toluene (3 × 1 mL), and deposited on an XRD substrate for powder XRD analysis (the pattern is included in Figure B.6).

The reaction was also undertaken in THF for comparison of the solid products. Cd(PTC)$_2$ (12 mg, 0.003 mmol) was dissolved in THF (3 mL) in a septum-capped vial and heated at 66 °C. The yellow product was washed three times with toluene (3 × 1 mL), and deposited on an XRD substrate for analysis (the pattern is included in Figure S6).

4.2.5 Monolayer CdS Shell Growth on CdSe QBs

A {CdSe[n-octylamine]$_{0.53}$}QB dispersion was prepared according to the literature.[2] In a typical synthesis, toluene (1 mL) was added to an aliquot of the QB dispersion (0.512 g), and the mixture was centrifuged using a benchtop centrifuge (2000 RPM, 3 min) to precipitate the QBs. The supernatant was discarded, and the procedure was repeated twice (for a total of three washing steps), to remove excess n-octylamine from the synthetic dispersion.

The purified CdSe QB precipitate from the procedure above was then suspended in a solution of Cd(PTC)$_2$ in THF (2 mL, 10 mM). The mixture was then heated at 66 °C, with reaction monitoring by UV-vis and PL spectroscopies at 1, 2, 3, 4, and 16 h. The ideal reaction time for monolayer shell growth was 3 h.

Each aliquot (2-3 drops) for spectroscopic analysis was combined with THF (0.5 mL), centrifuged using a benchtop centrifuge (2000 RPM, 3 min), and the supernatant was discarded. The resulting precipitate was then suspended in *n*-octylamine to re-passivate the QB surfaces with L-type ligation. This dispersion was combined with toluene (1 mL), and the mixture was centrifuged using a benchtop centrifuge (2000 RPM, 3 min) to precipitate the QBs. The supernatant was discarded, and the procedure was repeated to remove excess *n*-octylamine. The QBs were then suspended in toluene for acquisition of UV-vis and PL spectra.

4.3   Results

4.3.1   Preparation and Characterization of Cd(PTC)$_2$

The title compound was prepared from [NH$_4$][PTC][28] and CdCl$_2$ under aqueous conditions by adaptation of literature methods.[22, 29-34] The product Cd(PTC)$_2$ was collected as a pale-yellow precipitate in $\geq 60\%$ yields. The IR spectrum of Cd(PTC)$_2$ contained the characteristic features of dithiocarbamate ligands (Figure B.1), and the dithiocarbamate carbon appeared at 208 ppm in the ^{13}C{^{1}H} NMR spectrum. Interestingly, the ^{1}H NMR spectrum in THF-d_8 contained two singlets corresponding to the N-H, suggesting that Cd(PTC)$_2$ exists in this solvent as a mixture of nuclearities (monomer, dimer, or trimer, etc.). The compound was soluble in DMSO, THF, DMF, and insoluble in EtOH, MeOH, CHCl$_3$, CH$_2$Cl$_2$, and toluene.

Single crystals of Cd(PTC)$_2$ were obtained from THF/hexane, and the structure solved by X-ray diffraction. A one-dimensional-polymer structure is adopted (Figure 4.2a), which is similar to analogous cadmium dithiocarbamate structures recently reported.[34] The polymer crystallizes with one THF solvate molecule per Cd atom. All Cd atoms are crystallographically equivalent, and each Cd(PTC)$_2$ unit is bridged to two neighboring units

through μ-S interactions. Thus, each Cd center acquires a distorted octahedral coordination geometry with two κ_2-PTC ligands, and the two μ-S interactions, which have a *cis* relationship to one another (Figure 1b).
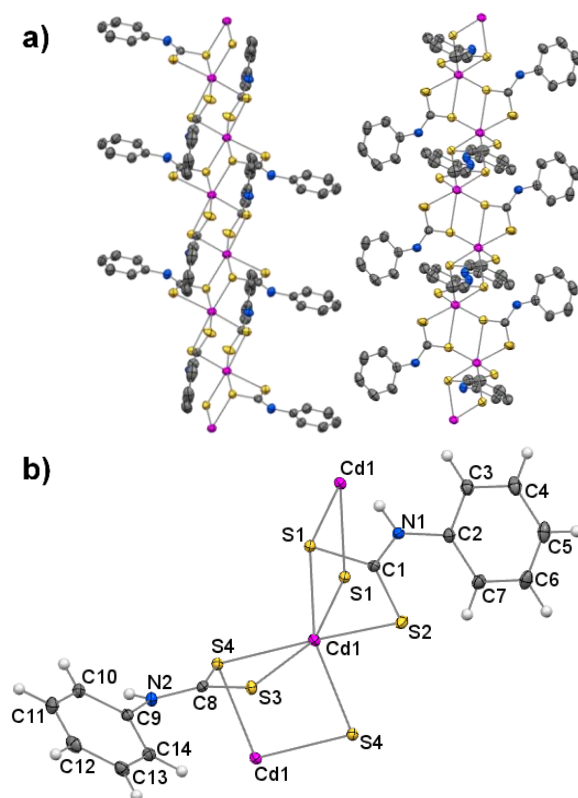
Figure 4.2   Thermal-ellipsoid plots from the crystal structure of Cd(PTC)$_2$. (a) Two views of the coordination-polymer structure (rotated 90° about the vertical relative to one another). (b) A numbering diagram revealing the coordination environment about the Cd atom. The THF solvate molecules are omitted.

The distorted-octahedral Cd center is surrounded by two longer (2.77 – 2.80 Å) and four shorter Cd-S interactions (2.62 – 2.69 Å), with the two longer interactions (Cd1-S1 and Cd1-S4) having a *trans* relationship. The S-Cd-S angles within the κ_2 chelate rings are smaller (66.8 – 67.7°), as expected, than those outside the chelate rings (85.5 – 110.4°), which are closer to the ideal for octahedral coordination. These distances and angles compare very closely to the corresponding values in the two analogous structures (Table 4 in ref. 32).

Table 4.2 Selected Bond Distances and Angles for Cadmium bis(phenyldithiocarbamate)

Distances (Å)		Angles (°)	
Cd1-S1	2.7992(3)	S1-Cd-S1'	85.461(8)
Cd1-S4'	2.7691(3)	S1-Cd-S2	66.752(8)
Cd1-S1'	2.6719(3)	S1-Cd-S3	89.032(8)
Cd1-S2	2.6149(3)	S1-Cd-S4	110.441(8)
Cd1-S3	2.6917(3)	S3-Cd1-S4	160.512(8)
Cd1-S4	2.6687(3)	S1-Cd-S4'	67.689(8)

4.3.2   Attempted L-type to Z-type Ligation Exchange using Cd(PTC)$_2$

L- to Z-type ligand exchange on CdSe QBs using Cd(oleate)$_2$ as the Z-type ligand was previously shown to produce instantaneous shifts in the QB absorption spectrum of 140 meV to lower energy at room temperature.[3] Consequently we expected that L- to Z-type exchange using Cd(PTC)$_2$ would produce spectral shifts of at least that magnitude. Surface exchange was investigated by combining (L-type) amine-ligated {CdSe[n-octylamine]$_{0.53}$} QBs with an excess quantity of a saturated (ca. 40 mM) solution of Cd(PTC)$_2$ in DMSO at room temperature. The n-octylamine-ligated CdSe QBs dispersed rapidly in DMSO solution of Cd(PTC)$_2$, whereas the QBs were immiscible in DMSO in the absence of Cd(PTC)$_2$ (Figure S9). These observations suggested that exchange of L-type amine ligation to Z-type Cd(PTC)$_2$ ligation had indeed occurred. Surprisingly, however, UV-visible spectroscopic monitoring revealed no initial shift of the CdSe QB spectrum within the first 5 min of combination with Cd(PTC)$_2$ (Figure 4.3a).

79
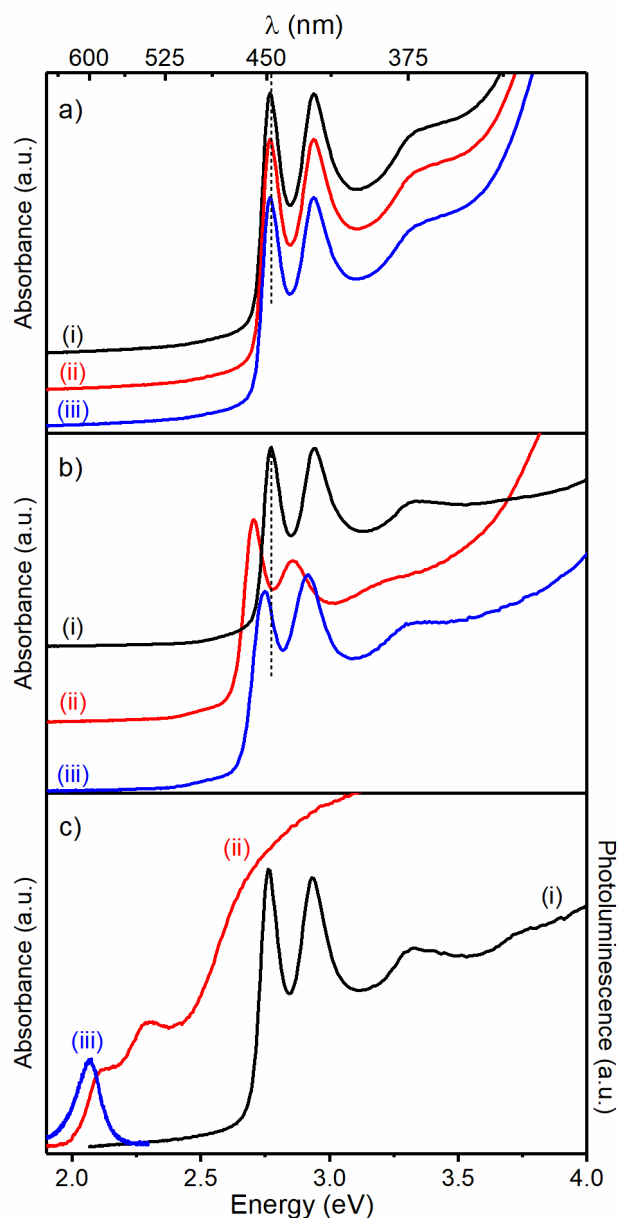
Figure 4.3 UV-visible and PL spectra from the reaction of {CdSe[*n*-octylamine]$_{0.53}$} QBs and excess Cd(PTC)$_2$. (a) Taken after 0 (i, black curve), 2 (ii, red), and 5 (iii, blue) min of reaction time at room temperature. (b) Starting {CdSe[*n*-octylamine]$_{0.53}$} QBs (i, black curve), taken after 40 min of reaction time at room temperature (ii, red), and the 40-min specimen after back exchange with *n*-octylamine (iii, blue). (c) Starting {CdSe[*n*-octylamine]$_{0.53}$} QBs (i, black curve), taken after 4 h of reaction time at 70 °C (ii, red), PL spectrum taken after 4 h of reaction time at 70 °C (PL QY = 1.2 ± 0.3%, iii, blue).

The spectrum *was* observed to shift to lower energy on the time scale of a few hours. For example, the lowest-energy feature in the spectrum of the starting amine-ligated QBs shifted from 449 nm to 458 nm after 40 min in the presence of Cd(PTC)$_2$, or by 60 meV

(Figure 4.3b). At this point, the excess $Cd(PTC)_2$, was removed, and the QBs were redispersed in neat *n*-octylamine. The CdSe QB spectrum instantaneously shifted to higher energy, in the direction of the original spectral shifts, but did not return to the original spectral positions (Figure 4.3b). The lowest energy feature, which had shifted from 449 to 458 nm in the presence of $Cd(PTC)_2$, shifted back only to 453 nm. The results were thus inconsistent with an instantaneous, reversible L-type, Z-type ligand exchange, as previously characterized for CdSe QBs.[3]

The reaction of {CdSe[*n*-octylamine]$_{0.53}$} QBs and excess $Cd(PTC)_2$ was subsequently undertaken at 70 °C. Within 15 minutes an obvious color change from pale yellow to tangerine orange was observed. After 4 h of reaction time, the mixture had become deep red. During this period, the CdSe QB spectrum was observed to shift progressively to lower energy, reaching a maximum shift of the lowest-energy feature of 664 meV, from 449 to 591 nm (Figure 4.3c). Thus, a very large spectral shift was observed, in the direction expected for exchange of L-type ligation to Z-type ligation, but several observations indicated a process more complex than a straightforward surface-ligand exchange.

After reaction with $Cd(PTC)_2$ at 70 °C, the resulting CdSe QBs were redispersed in *n*-octylamine. No further shifting of the QB spectral features was observed, and the spectrum remained as in Figure 4.3c. Moreover, the PL spectrum retained a significant fraction of the intensity of the initial {CdSe[*n*-octylamine]$_{0.53}$} QB spectrum, upon shifting to lower energy (Figure 3c). In contrast, Z-type ligation on CdSe QBs had previously resulted in a quenching of the PL spectrum.[3] The failure to restore L-type QB passivation by back exchange with *n*-octylamine, and the observation of a PL spectrum inconsistent with Z-type passivation, strongly suggested that the surface-exchange processes had not occurred in the expected manner.

81
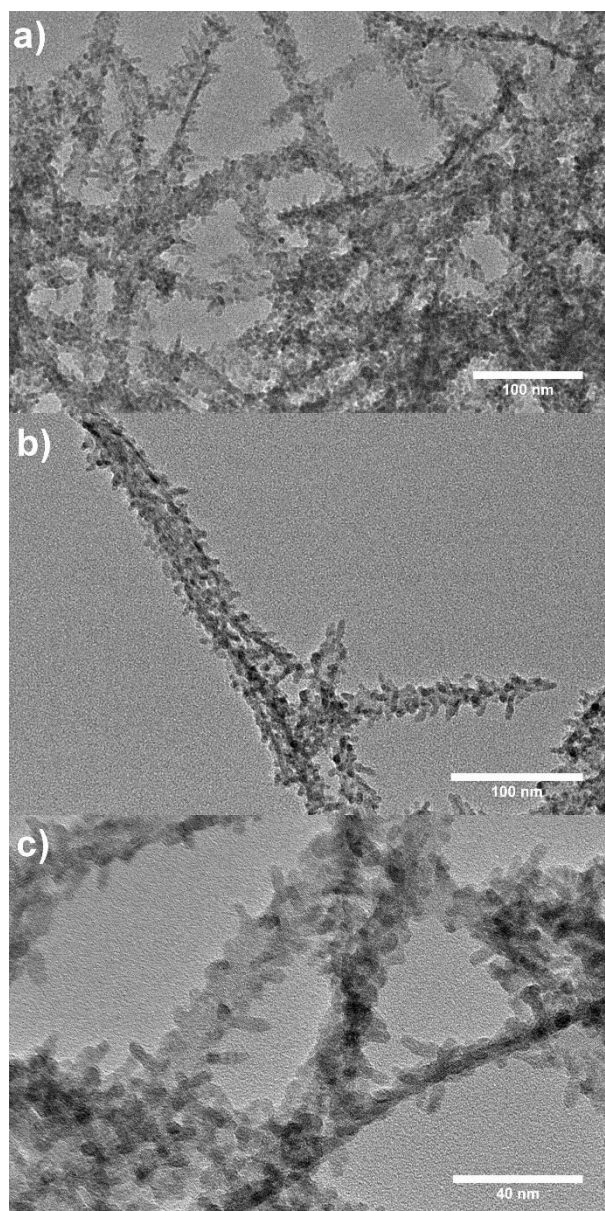
Figure 4.4   TEM images of CdSe QBs after reaction with excess Cd(PTC)$_2$ at 70 °C.

TEM images of the CdSe QBs after reaction with Cd(PTC)$_2$ at 70 °C are given in

Figure 4.4. The pseudo-one-dimensional morphologies of the CdSe QBs were evident in the

images, but with the QBs coated by spiny shells. We surmised that the shells and nodules

consisted of CdS resulting from decomposition of Cd(PTC)$_2$. Elemental analysis indicated an

S content (20.7 wt. %) dramatically higher than that consistent with Z-type Cd(PTC)$_2$

ligation. A single set of sharp wurtzite reflections was observed in the XRD pattern of the

coated QBs (Figure 4.5), which indexed to a CdSe lattice compressively strained by 2.56% in

a and 2.99% in *c*, consistent with the deposition of an epitaxial CdS shell. That the first few

layers of shell were deposited epitaxially was also indicated by the significant PL intensity

(see above and Figure 4.3c). We concluded that the epitaxial growth of the first CdS shell

layers was followed by CdS islanding in the Stranski-Krastanov mode,[39-41] and then nodule

growth from the islands. Thus, the excess of $Cd(PTC)_2$ precursor employed resulted in the

growth of thick, spiny CdS shells on the CdSe QBs. The pathway for the conversion of the

$Cd(PTC)_2$ precursor to CdS was next elucidated.
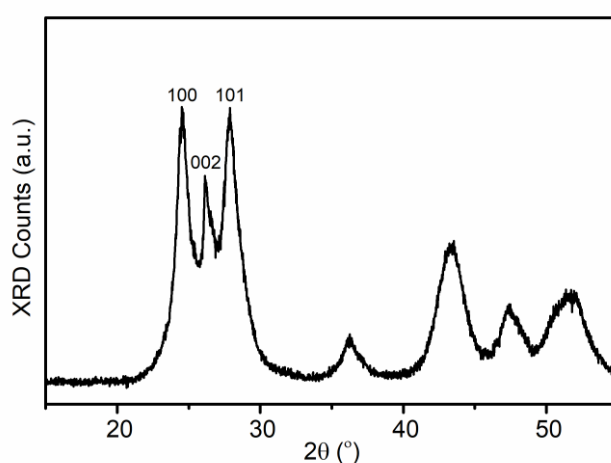
Figure 4.5   Powder XRD pattern of thick-shelled CdS-CdSe QBs displaying a single set of sharp, wurtzite peaks, consistent with epitaxial shell growth. The first three wurtzite reflections are indexed.

4.3.3   Chemical Pathway from $Cd(PTC)_2$ to CdS

We investigated the thermal decomposition of $Cd(PTC)_2$ under the conditions

described above, but in the absence of the CdSe QBs. Thermolysis of $Cd(PTC)_2$ at 70 °C in

DMSO resulted in the initial appearance of a powdery yellow precipitate within 1 h, which

appeared to become complete in about 4 h. XRD analysis gave a broadened wurtzite pattern

corresponding to CdS. Examination of the powder by energy-dispersive X-ray spectroscopy

(EDS) in the TEM gave a Cd:S ratio of 47.5:52.5. The yellow CdS powder was obtained

from the thermolysis in 94% yield.

The conversion of Cd(PTC)$_2$ to CdS was subsequently monitored by ^{1}H and ^{13}C{^{1}H} NMR spectroscopy in DMSO-d_6 at 50 °C, in the presence and absence of added n-octylamine catalyst. The results in the presence and absence of the amine catalyst were similar (see below). Spectra were recorded at 1-h intervals.

Monitoring by ^{1}H NMR in the absence of added amine catalyst established the disappearance of Cd(PTC)$_2$ over about 6 h (Figure B6). During this period, aniline (PhNH$_2$) appeared as an intermediate, and then nearly disappeared. The formation of CS$_2$ and phenylisothiocyanate was evident by ^{13}C{^{1}H} NMR within 2 h (Figure S7). The PhNCS also appeared as an intermediate species, which nearly disappeared over time. The formation of 1,3-diphenylthiourea was evident by ^{1}H NMR after 2 h, which gradually increased in concentration over the total 12 h period of monitoring. A graph showing the time-dependence of the relative concentrations of Cd(PTC)$_2$, aniline, and 1,3-diphenylthiourea, derived from integration of the ^{1}H NMR spectra, is shown in Figure 4.6.
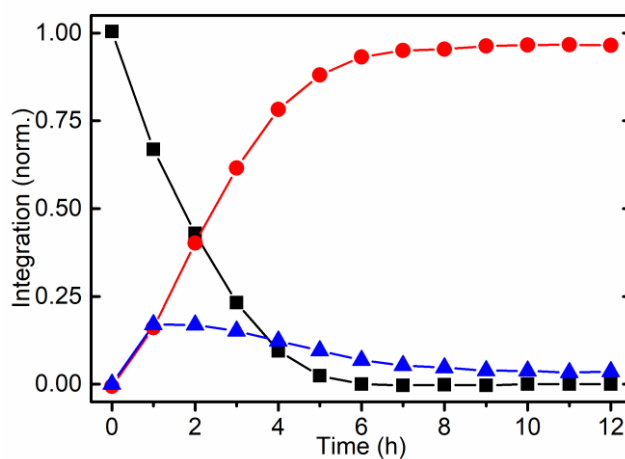
Figure 4.6   Time-dependence of the relative concentrations of Cd(PTC)$_2$ (black squares), aniline (PhNH$_2$, blue triangles), and 1,3-diphenylthiourea (red circles), monitored via ^{1}H NMR. The y-axis is the normalized integrated intensity of the N-H resonances for each. The curves are to guide the eye.

The results above established that Cd(PTC)$_2$ was ultimately converted to the persistent products CdS, CS$_2$, and 1,3-diphenylthiourea, with aniline and PhNCS participating

as intermediates. We proposed a base-catalyzed pathway (eqs 1-3) consistent with these results. Deprotonation of a Cd(PTC)$_2$ N-H group produces CdS, PhNCS, and a displaced PTC anion by eq 1. Protonation of the displaced PTC anion generates aniline and CS$_2$ by eq 2. Finally, reaction of aniline and PhNCS gives 1,3-diphenylthiourea by eq 3. The catalytic base is an adventitious species, Cd(PTC)$_2$ itself, and/or the generated aniline.

The same sequence of products and intermediates was observed by spectroscopic monitoring with added aniline to serve as the base catalyst. The initial rate with the added base was faster, but the conversion ultimately scaled to the rate of the intrinsic process (Figure B8). We note that the base-catalyzed pathway proposed in eqs 1-3 resembles corresponding pathways proposed by Caudle and coworkers,[42] but differs in the identities of some intermediates and final products.
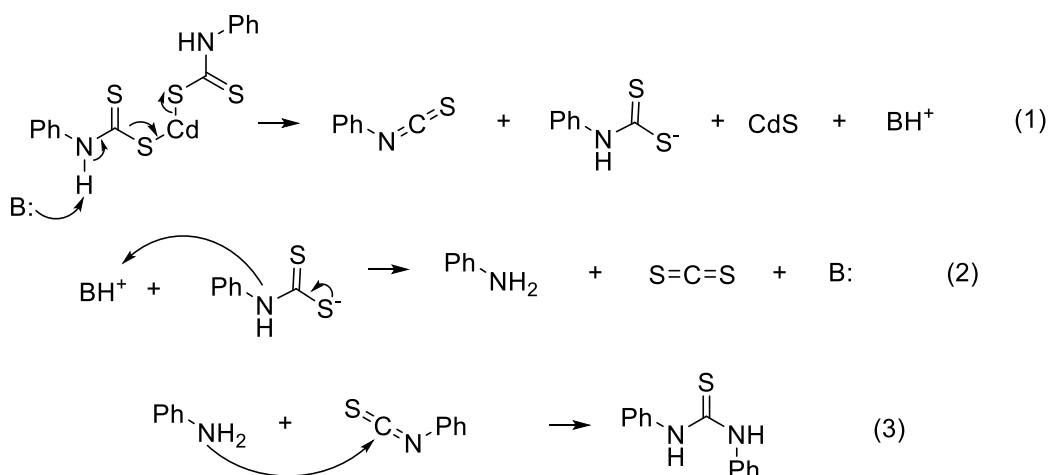
4.3.4 Controlled Growth of One-Monolayer CdS Shells on CdSe QBs

The shell-growth process described above was conducted (in THF at 66 °C) with the amount of Cd(PTC)$_2$ limited to 1.0-1.5 times that estimated to produce one-monolayer[4] CdS shells on the CdSe QBs. The resulting absorption spectrum of the core-shell QBs is shown in Figure 6, in which the lowest-energy feature in the QB spectrum was shifted by 514 meV to lower energy relative to the starting QBs. The PL spectrum was similarly shifted to lower energy, and retained significant intensity (Figure 6, PL QY = 1.53%).

85
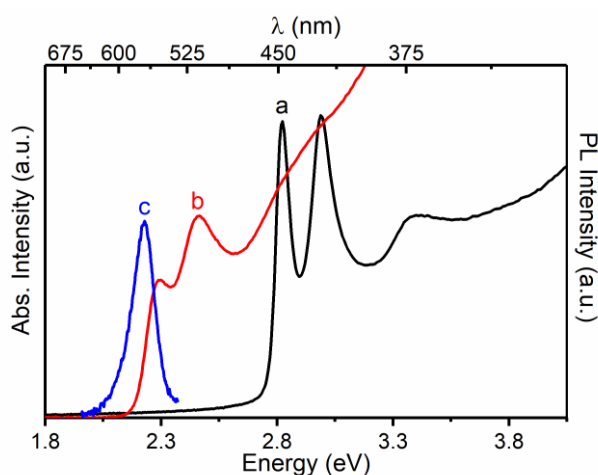
Figure 4.7   UV-visible and PL spectra of CdSe QBs. (a) UV-visible spectrum of the starting {CdSe[*n*-octylamine]$_{0.53}$} QBs (black curve); (b) UV-visible spectrum of core-shell CdSe-CdS QBs having shells of monolayer thickness (red curve); (c) PL spectrum of the specimen in b (blue curve).

The XRD pattern of the core-shell QBs again contained a single set of wurtzite reflections, consistent with the growth of epitaxial CdS shells on the CdSe QB cores. Figure 7 compares the XRD patterns of the initial, core-only QBs to the CdSe-CdS core-shell QBs produced with the limited amount of Cd(PTC)$_2$ precursor, in the region of the 100, 002, and 101 wurtzite reflections. The starting, amine-passivated CdSe QBs bundle into tight aggregates in which the broad top and bottom QB facets are stacked together.[2] These bundles are preferentially oriented, taking the 002 planes out of the condition for diffraction. Consequently, the 002 reflection is generally not visible in the XRD patterns of the as-synthesized, amine-passivated QBs, as in Figure 4.8a.[3]
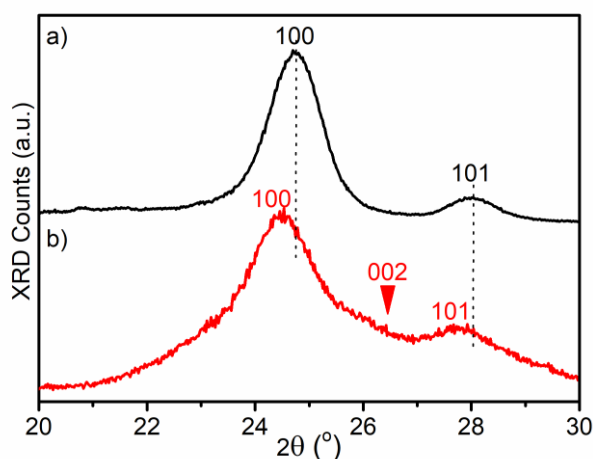
Figure 4.8 XRD patterns of CdSe QBs. (a) Bundled, starting {CdSe[*n*-octylamine]$_{0.53}$} QBs (black curve); (b) Core-shell CdSe-CdS QBs having shells of monolayer thickness (red curve).

Correspondingly, the 002 reflection in the XRD pattern of the CdSe-CdS core-shell QBs (arrow in Figure 4.8b) was extremely weak, although not completely quenched, indicating the QBs to also be largely bundled in face-to-face stacks, and preferentially oriented on the XRD substrate. The preferential orientation was not as strong in the core-shell QBs, suggesting that that the QBs had unbundled during shell growth, and incompletely re-bundled thereafter. This proposal was also supported by TEM imaging (see below).

In contrast, the spiny CdS nodules on the QBs having thick shells (Figure 3) disrupted the bundling, thus randomizing their orientations, and consequently all of the 100, 002, and 101 reflections were well resolved in the XRD patterns (Figure 4.5) of these thick-shelled QBs. Thus, the XRD data for the thin-shelled QBs strongly suggested the spiny CdS nodules to be absent.

The lattice parameters extracted from the data in Figure 4.8b established a significant lattice compression in *c* of 3.65% (relative to bulk CdSe). The *c* axis is oriented in the CdSe QBs along their long axis, and *c* is thus compressively strained by the large core-shell

87

interface lying along that direction, given the smaller *a* and *c* of CdS. Thus, these data were also consistent with the growth of an epitaxial, compressive CdS shell on the CdSe QBs.

The core-shell QBs were redispersed in *n*-octylamine, and deposited on TEM grids for imaging. Figure 8a provides a relatively low-magnification image of the QBs, which contains both bundled aggregates and individual QBs as inferred from the XRD data (Figure 7b), consistent with partial restacking after shell growth and precipitation from dispersion.

HR-TEM views of bundled stacks are shown in Figures 4.9b and B.9a, from which the edge thickness of the core-shell QBs was measured (see below). Figures 4.9c and B9b are HR-TEM images of the broad (top or bottom) facets of core-shell QBs. Notably, the lattice fringes in both the edge- and broad-facet views extended uninterrupted throughout the thickness and breadth of the core-shell QBs, as required of epitaxial shells.
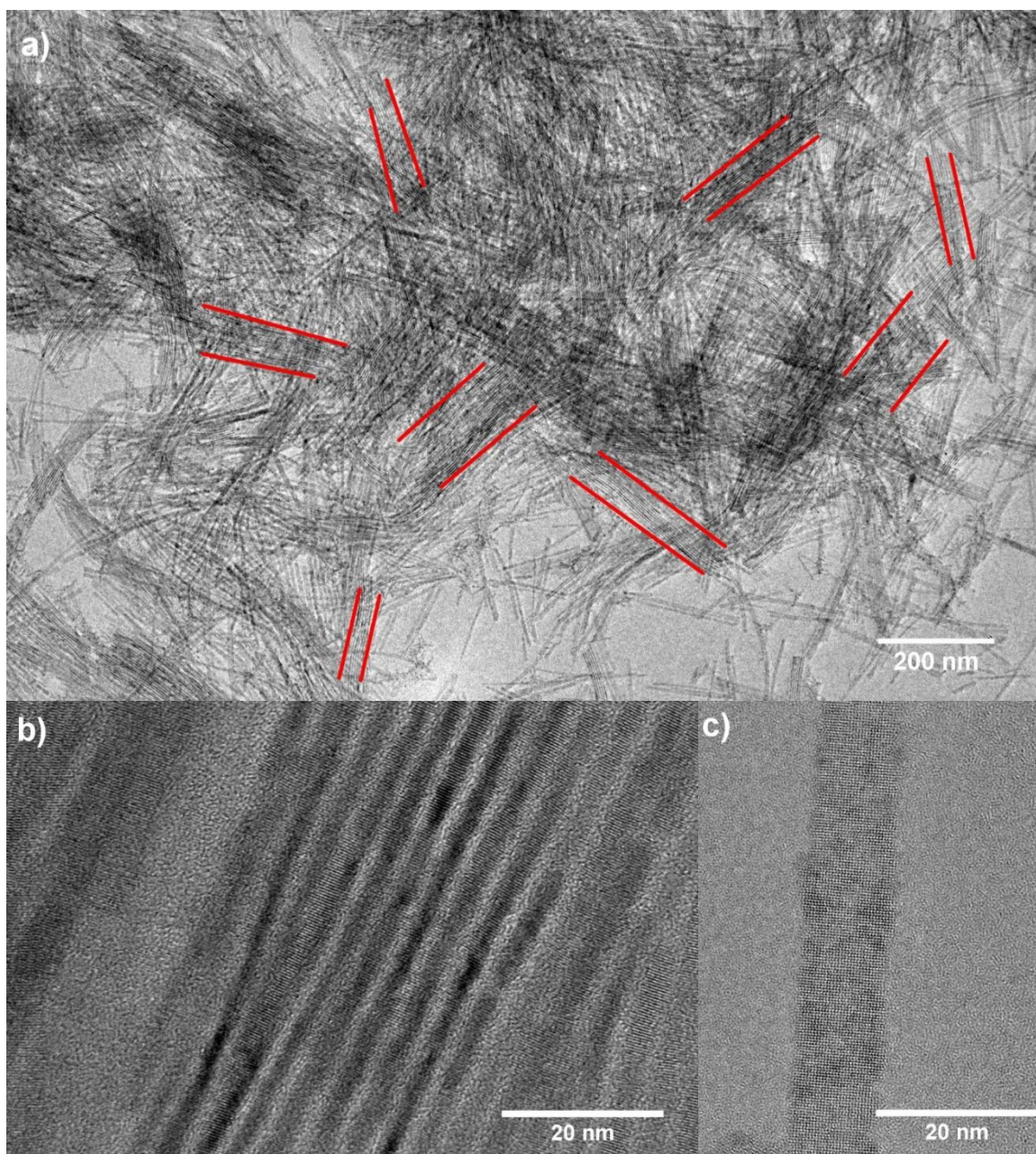
Figure 4.9 HR-TEM images of core-shell CdSe-CdS QBs having shells of monolayer thickness. (a) Low-magnification image; QB bundles marked by red lines. (b) Higher-magnification image of a bundled QB stack revealing the thickness dimension of the QBs. (c) Higher-magnification image of a single QB revealing its broad top surface.

The mean thickness of the core-shell QBs was obtained from approximately 300

measurements from Figures 4.9b, B8a, and related images providing edge views of stacked

bundles. The value so obtained was a mean thickness of 2.5 ± 0.2 nm. The total shell

thickness was determined to be 0.7 ± 0.2 nm by subtracting the discrete 1.8-nm thickness of

the CdSe QB cores.[2] Given the known crystallographic orientation of the QBs, and thus the

epitaxial shells, a monolayer shell thickness corresponded to the lattice parameter of wurtzitic

CdS, $a = 0.412$ nm.[4] Consequently, the experimentally determined total shell thickness was

within experimental error of a one-monolayer CdS shell on the top and bottom surfaces of the

CdSe QBs.

4.4   Discussion

4.4.1   "L-to-Z-to-Shell."

The results above suggest the shell-growth pathway depicted in Scheme 2. Addition

of $Cd(PTC)_2$ to the amine-ligated CdSe QBs (Scheme 4.2a) results in an L-type to Z-type

ligand exchange, affording CdSe QBs with $Cd(PTC)_2$ passivation (Scheme 4.2b). Although

we did not observe the expected spectral shift upon L-type to Z-type exchange, the enhanced

DMSO dispersibility of the QBs in the presence of $Cd(PTC)_2$ suggests that it occurred. The

exchange process liberates *n*-octylamine, which subsequently base-catalyzes the breakdown

of $Cd(PTC)_2$ to CdS according to eqs 1-3, forming an epitaxial shell. In the presence of

excess $Cd(PTC)_2$, the cycle repeats, thickening the shell. At a critical shell thickness, the

growth transitions to island, nodule, and spine formation according to the Stranski-Krastanov

mode.[39-41] When the amount of $Cd(PTC)_2$ is restricted, CdS deposition is limited to a

monolayer shell.

Scheme 4.2 Proposed CdS Shell-Growth Pathway. (a) *n*-octylamine-ligated CdSe QB; (b) Cd(PTC)₂-ligated QB; (c) CdSe QB with a monolayer CdS shell; (d) CdSe QB with a thicker CdS shell grown in the Stranski-Krastanov mode.
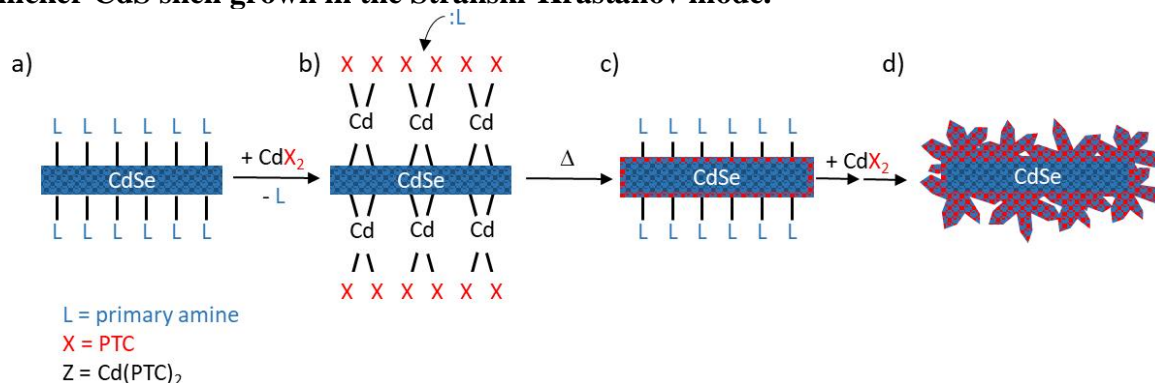
Ample precedent exists for the conversion of surface-bound Cd(PTC)$_2$ ligands to a CdS shell as described here (Scheme 4.2). Munro, Kilina, and coworkers reported ligand-exchange reactions of 3,5-dimethylphenyldithiocarbamate ligands and CdSe nanocrystals, which, in addition to simple exchange, produce ligand-breakdown byproducts analogous to those we observed in eqs 1-3.[43] They found 3,5-dimethylphenyldithiocarbamate to be unstable in solution and in the coordination shell of CdSe nanocrystals. Kelley and coworkers examined the breakdown of *p*-methoxyphenyldithiocarbamate ligands in the coordination shell of CdSe nanocrystals, finding evidence by Raman spectroscopy for the formation of CdS shells.[44] Gladfelter, Norris and coworkers employed the thermolysis of octyldithiocarbamate ligands to form CdS matrices encapsulating films of PbSe-CdSe nanocrystals.[23] Finally, Caudle and coworkers studied the thermal decomposition of alkyldithiocarbamate complexes Cd(S$_2$CNHR)$_2$ at temperatures of 110 – 140 °C, which afford CdS and byproducts related to those we have reported here.[42]

Although several methods exist for deposition of heterostructure shells on semiconductor nanocrystals (colloidal quantum dots),[45] the low-temperature method described here appears to be particularly promising for nanocrystals having an extended length dimension, such as QBs, and quantum wires or nanowires. Interfacial misfit strain accumulates along the long dimension in core-shell QBs and nanowires, which may be

partially relaxed by surface (shell-thickness) modulations.[46-47] However, shell breakage or islanding occurs when such modulations are extreme. Consequently, the shells deposited on nanowires are frequently roughened, cracked, and nonepitaxial. [39, 48-49]

Because of the (thermal) instability of the core-shell interface in QBs and quantum wires, the (high-temperature) SILAR method,[50] which is exceptionally successful for shell growth on small nanoncrystals and colloidal quantum dots, does not in our hands produce epitaxial shells on semiconductor QBs and quantum wires. The room-temperature, biphasic c-ALD method[21] also fails in our hands due to difficulty transferring long-dimension nanocrystals between the polar and nonpolar phases employed. We previously reported an oxidative-substitution method for forming monolayer CdS shells on CdTe quantum wires,[51] but the method does not appear to be generalizable. Thus, the single-source-precursor method developed here, which produces intact, epitaxial, controlled-thickness shells on CdSe QBs at low temperatures, may have niche applications.

4.5 Conclusions

L- to Z-type ligand exchange of amine-ligated {CdSe[n-octylamine]$_{0.53}$} QBs with the dithiocarbamate complex Cd(PTC)$_2$ produces reactive passivation layers on the QBs that readily convert to epitaxial CdS shells. The chemical pathway for this conversion has been elucidated, and is consistent with related literature studies. Stoichiometric control results in CdSe QBs having intact, monolayer, epitaxial CdS shells.

Associated Content can be found in Appendix B

4.6   References

1.   Morrison, C. E.; Wang, F.; Rath, N. P.; Wieliczka, B. M.; Loomis, R. A.; Buhro, W. E., Cadmium *Bis*(phenyldithiocarbamate) as a Nanocrystal Shell-Growth Precursor. *Inorg. Chem.* **2017,** *56* (21), 12920-12929.

2.   Liu, Y.-H.; Wayman, V. L.; Gibbons, P. C.; Loomis, R. A.; Buhro, W. E., Origin of High Photoluminescence Efficiencies in CdSe Quantum Belts. *Nano Lett.* **2010,** *10* (1), 352-357.

3.   Zhou, Y.; Wang, F.; Buhro, W. E., Large Exciton Energy Shifts by Reversible Surface Exchange in 2D II–VI Nanocrystals. *J. Am. Chem. Soc.* **2015,** *137* (48), 15198-15208.

4.   Wang, F.; Wang, Y.; Liu, Y.-H.; Morrison, P. J.; Loomis, R. A.; Buhro, W. E., Two-Dimensional Semiconductor Nanocrystals: Properties, Templated Formation, and Magic-Size Nanocluster Intermediates. *Acc. Chem. Res.* **2015,** *48* (1), 13-21.

5.   Anderson, N. C.; Hendricks, M. P.; Choi, J. J.; Owen, J. S., Ligand Exchange and the Stoichiometry of Metal Chalcogenide Nanocrystals: Spectroscopic Observation of Facile Metal-Carboxylate Displacement and Binding. *J. Am. Chem. Soc.* **2013,** *135* (49), 18536-18548.

6.   Evans, C. M., Love, A.M.,Weiss, E.A., Semiconductor Clusters Polymerize to Quantum Dots through Competing Step-Growth Mechanisms. *J. Am. Chem. Soc.* **2012,** *134*, 17298-17305.

7.   Knowles, K. E.; Frederick, M. T.; Tice, D. B.; Morris-Cohen, A. J.; Weiss, E. A., Colloidal Quantum Dots: Think Outside the (Particle-in-a-)Box. *J. Phys. Chem. Lett.* **2012,** *3* (1), 18-26.

8. von Holt, B.; Kudera, S.; Weiss, A.; Schrader, T. E.; Manna, L.; Parak, W. J.; Braun, M., Ligand Exchange of CdSe Nanocrystals Probed by Optical Spectroscopy in the Visible and Mid-IR. *J. Mater. Chem.* **2008,** *18* (23), 2728-2732.

9. Frederick, M. T.; Amin, V. A.; Cass, L. C.; Weiss, E. A., A Molecule to Detect and Perturb the Confinement of Charge Carriers in Quantum Dots. *Nano Lett.* **2011,** *11* (12), 5455-5460.

10. Frederick, M. T.; Amin, V. A.; Weiss, E. A., Optical Properties of Strongly Coupled Quantum Dot–Ligand Systems. *J. Phys. Chem. Lett.* **2013,** *4* (4), 634-640.

11. Morris-Cohen, A. J.; Frederick, M. T.; Lilly, G. D.; McArthur, E. A.; Weiss, E. A., Organic Surfactant-Controlled Composition of the Surfaces of CdSe Quantum Dots. *J. Phys. Chem. Lett.* **2010,** *1* (7), 1078-1081.

12. Frederick, M. T.; Weiss, E. A., Relaxation of Exciton Confinement in CdSe Quantum Dots by Modification with a Conjugated Dithiocarbamate Ligand. *ACS Nano* **2010,** *4* (6), 3195-3200.

13. Zhang, Y. C.; Wang, G. Y.; Hu, X. Y., Solvothermal Synthesis of Hexagonal CdS Nanostructures from a Single-Source Molecular Precursor. *J. Alloys Compd.* **2007,** *437* (1–2), 47-52.

14. Zhang, H.; Yang, D.; Ma, X., Synthesis of Flower-like CdS Nanostructures by Organic-free Hydrothermal Process and Their Optical Properties. *Mater. Lett.* **2007,** *61* (16), 3507-3510.

15. Malik, M. A.; Saeed, T.; O'Brien, P., The Synthesis and Characterization of Cadmium and Zinc Complexes with Dithiocarbamate Derivatives of Diamines. *Polyhedron* **1993,** *12* (12), 1533-1538.

16. Trindade, T.; O'Brien, P., Synthesis of CdS and CdSe Nanoparticles by Thermolysis of Diethyldithio-or Diethyldiseleno-Carbamates of Cadmium. *J. Mater. Chem.* **1996,** *6* (3), 343-347.

17. Green, M.; O'Brien, P., The Use of an Adduct in Improved Syntheses of Nanoparticulate Chalcogenide Semiconductors Containing Cadmium. *Adv. Mater. Opt. Electron.* **1997,** *7* (6), 277-279.

18. Nyamen, L. D.; Revaprasadu, N.; Pullabhotla, R. V. S. R.; Nejo, A. A.; Ndifon, P. T.; Malik, M. A.; O'Brien, P., Synthesis of Multi-Podal CdS Nanostructures Using Heterocyclic Dithiocarbamato Complexes as Precursors. *Polyhedron* **2013,** *56*, 62-70.

19. Ludolph, B.; A. Malik, M., Novel Single Molecule Precursor Routes for the Direct Synthesis of Highly Monodispersed Quantum Dots of Cadmium or Zinc Sulfide or Selenide. *Chem. Commun.* **1998,** (17), 1849-1850.

20. Barreca, D.; Gasparotto, A.; Maragno, C.; Tondello, E.; Sada, C., CVD of Nanophasic (Zn, Cd)S Thin Films: From Multi-Layers to Solid Solutions. *Chem. Vap. Deposition* **2004,** *10* (4), 229-236.

21. Ithurria, S.; Talapin, D. V., Colloidal Atomic Layer Deposition (c-ALD) using Self-Limiting Reactions at Nanocrystal Surface Coupled to Phase Transfer between Polar and Nonpolar Media. *J. Am. Chem. Soc.* **2012,** *134* (45), 18585-18590.

22. Onwudiwe, D. C.; Strydom, C. A., The Bipyridine Adducts of *N*-Phenyldithiocarbamato Complexes of Zn(II) and Cd(II); Synthesis, Spectral, Thermal Decomposition Studies and Use as Precursors for ZnS and CdS Nanoparticles. *Spectrochim. Acta A* **2015,** *135*, 1080-1089.

23. Wills, A. W.; Kang, M. S.; Khare, A.; Gladfelter, W. L.; Norris, D. J., Thermally Degradable Ligands for Nanocrystals. *ACS Nano* **2010,** *4* (8), 4523-4530.

24. Polovitsyn, A.; Dang, Z.; Movilla, J. L.; Martin-Garcia, B.; Khan, A. H.; Bertrand, G. H. V.; Brescia, R.; Moreels, I., Synthesis of Air-Stable CdSe/ZnS Core-Shell Nanoplatelets with Tunable Emission Wavelength. *Chem. Mater.* **2017**.

25. Nan, W.; Niu, Y.; Qin, H.; Cui, F.; Yang, Y.; Lai, R.; Lin, W.; Peng, X., Crystal Structure Control of Zinc-Blende CdSe/CdS Core/Shell Nanocrystals: Synthesis and Structure-Dependent Optical Properties. *J. Am. Chem. Soc.* **2012**, *134* (48), 19685-19693.

26. Revaprasadu, N.; Azad Malik, M.; O'Brien, P.; Wakefield, G., A Simple Route to Synthesise Nanodimensional CdSe-CdS Core-Shell Structures from Single Molecule Precursors. *Chem. Commun.* **1999**, (16), 1573-1574.

27. Abdelhady, A. L.; Afzaal, M.; Malik, M. A.; O'Brien, P., Flow Reactor Synthesis of CdSe, CdS, CdSe/CdS and CdSeS Nanoparticles from Single Molecular Precursor(s). *J. Mater. Chem.* **2011**, *21* (46), 18768-18775.

28. Wessels, J. M.; Nothofer, H.-G.; Ford, W. E.; von Wrochem, F.; Scholz, F.; Vossmeyer, T.; Schroedter, A.; Weller, H.; Yasuda, A., Optical and Electrical Properties of Three-Dimensional Interlinked Gold Nanoparticle Assemblies. *J. Am. Chem. Soc.* **2004**, *126* (10), 3349-3356.

29. Hursthouse, M. B.; Malik, M. A.; Motevalli, M.; O'Brien, P., The Crystal and Molecular Structure of *N,N*-Diethyldiselenocarbamatocadmium(II): Cadmium and Zinc Diethyldiselenocarbamates as Precursors for Selenides. *Polyhedron* **1992**, *11* (1), 45-48.

30. Humeres, E.; Debacher, N. A.; Franco, J. D.; Lee, B. S.; Martendal, A., Mechanisms of Acid Decomposition of Dithiocarbamates. 3. Aryldithiocarbamates and the Torsional Effect. *J. Org. Chem.* **2002**, *67* (11), 3662-3667.

31. Onwudiwe, D. C.; Arfin, T.; Strydom, C. A.; Kriek, R. J., A Study of the Thermal and AC Impedance Properties of *N*-Phenyldithiocarbamate Complexes of Zn(II). *Electrochim. Acta* **2013**, *109*, 809-817.

32. Onwudiwe, D. C.; Arfin, T.; Strydom, C. A.; Kriek, R. J., Synthesis, spectroscopic characterization and behavior of AC impedance spectroscopy of Cd(II) bis(N-para-methylphenyl dithiocarbamate). *Electrochimica Acta* **2013,** *104*, 19-25.

33. Srinivasan, N., Synthesis and Characterization of Functionalized Dithiocarbamates: New Single-Source Precursors for CdS. *Superlattices Microstruct.* **2014,** *65*, 227-239.

34. Ferreira, I. P.; de Lima, G. M.; Paniago, E. B.; Pinheiro, C. B.; Wardell, J. L.; Wardell, S. M. S. V., Study of Metal Dithiocarbamate Complexes, Part V. Metal Complexes of [S$_2$CN(CH$_2$CH(OMe)$_2$)]: A Standard Dimeric Zinc Dithiocarbamate Structural Motive, a Rare Cadmium Dithiocarbamate Coordination Polymer, and a Hydrated Sodium Dithiocarbarmate Complex, with a[Na$_2$O$_2$] Core and Chain. *Inorg. Chim. Acta* **2016,** *441*, 137-145.

35. *APEX II*, Bruker Analytical X-Ray: Madison, WI, 2016.

36. *SAINT*, Bruker Analytical X-ray: Madison, WI, 2016.

37. *SADABS*, Bruker Analytical X-ray: Madison, WI, 2014.

38. Sheldrick, G., A Short History of SHELX. *Acta Crystallogr. Sect. A: Found. Crystallogr.* **2008,** *64* (1), 112-122.

39. Goebl, J. A.; Black, R. W.; Puthussery, J.; Giblin, J.; Kosel, T. H.; Kuno, M., Solution-Based II−VI Core/Shell Nanowire Heterostructures. *J. Am. Chem. Soc.* **2008,** *130* (44), 14822-14833.

40. Pan, L.; Lew, K.-K.; Redwing, J. M.; Dickey, E. C., Stranski−Krastanow Growth of Germanium on Silicon Nanowires. *Nano Lett.* **2005,** *5* (6), 1081-1085.

41. Jiang, Z.-J.; Kelley, D. F., Stranski–Krastanov Shell Growth in ZnTe/CdSe Core/Shell Nanocrystals. *J. Phys. Chem. C* **2013,** *117* (13), 6826-6834.

42. van Poppel, L. H.; Groy, T. L.; Caudle, M. T., Carbon−Sulfur Bond Cleavage in *Bis*(*N*-alkyldithiocarbamato)cadmium(II) Complexes: Heterolytic Desulfurization Coupled to Topochemical Proton Transfer. *Inorg. Chem.* **2004,** *43* (10), 3180-3188.

43. Munro, A. M.; Chandler, C.; Garling, M.; Chai, D.; Popovich, V.; Lystrom, L.; Kilina, S., Phenyldithiocarbamate Ligands Decompose During Nanocrystal Ligand Exchange. *J. Phys. Chem. C* **2016,** *120* (51), 29455-29462.

44. Grenland, J. J.; Lin, C.; Gong, K.; Kelley, D. F.; Kelley, A. M., Resonance Raman Investigation of the Interaction between Aromatic Dithiocarbamate Ligands and CdSe Quantum Dots. *J. Phys. Chem. C* **2017,** *121* (12), 7056-7061.

45. Reiss, P.; Protière, M.; Li, L., Core/Shell Semiconductor Nanocrystals. *Small* **2009,** *5* (2), 154-168.

46. Wang, H.; Upmanyu, M.; Ciobanu, C. V., Morphology of Epitaxial Core−Shell Nanowires. *Nano Lett.* **2008,** *8* (12), 4305-4311.

47. Schmidt, V.; McIntyre, P. C.; Gösele, U., Morphological instability of misfit-strained core-shell nanowires. *Phys. Rev. B* **2008,** *77* (23), 235302.

48. Jiang, F.; Liu, J.; Li, Y.; Fan, L.; Ding, Y.; Li, Y., Ultralong CdTe Nanowires: Catalyst-Free Synthesis and High-Yield Transformation into Core–Shell Heterostructures. *Adv. Funct. Mater.* **2012,** *22* (11), 2402-2411.

49. Liu, S.; Zhang, W.-H.; Li, C., Colloidal synthesis and characterization of CdSe/CdTe core/shell nanowire heterostructures. *J. Cryst. Growth* **2011,** *336* (1), 94-100.

50. Li, J. J.; Wang, Y. A.; Guo, W.; Keay, J. C.; Mishima, T. D.; Johnson, M. B.; Peng, X., Large-Scale Synthesis of Nearly Monodisperse CdSe/CdS Core/Shell Nanocrystals Using Air-Stable Reagents via Successive Ion Layer Adsorption and Reaction. *J. Am. Chem. Soc.* **2003,** *125* (41), 12567-12575.

51. Liu, Y.-H.; Wang, F.; Hoy, J.; Wayman, V. L.; Steinberg, L. K.; Loomis, R. A.; Buhro, W. E., Bright Core–Shell Semiconductor Quantum Wires. *J. Am. Chem. Soc.* **2012,** *134* (45), 18797-18803.

Chapter 5. Stable Metal Dithiocarbamates for Ligand Exchange

5.1   Introduction

L-type (neutral, two-electron donor) for Z-type (neutral, two-electron acceptor) ligand exchange has proven to be a facile way of modifying the surface of wurtzite CdSe quantum belts (QBs).[1-2] Experiments have demonstrated that Z-type, or MX_2 ligation, completely displaces L-type primary amine ligation and produces large energetic shifts in the absorption spectra (up to 215 meV). These exchanges are almost completely reversible meaning that the Z-type ligation can be replaced by L-type primary amine ligation, leaving the original CdSe QB structure intact.

In recent years, there has been significant interest in the installation of "functional organic ligands," with the goal of manipulating charge carrier dynamics and optoelectronic properties of semiconducting nanocrystals.[3-7] Phenyldithiocarbamate (PTC), an X-type (anionic, one electron donor) ligand, garnered ample attention for its ability to induce large energetic shifts (up to 1 eV) of the absorption spectrum when coordinated to the surface of II-VI quantum dots.[3-5, 7] It was later determined that PTC and its para-substituted derivatives are susceptible to both acid- and base- catalyzed decomposition.[8-10] In Chapter 4, we described the synthesis and characterization of $Cd(PTC)_2$, the MX_2 or Z-type derivative of PTC. L-for-Z-type ligand exchange experiments were attempted on the surface of CdSe QBs, but $Cd(PTC)_2$ also decomposed under the reaction conditions necessary for ligand exchange. The efficiency of the displacement of the L-type n-alkylamine native ligand by $Cd(PTC)_2$ could not be determined. However, the n-alkylamine native ligand catalyzed the decomposition of $Cd(PTC)_2$ into CdS on the surface of the CdSe QBs, with CS_2 and aniline as by-products. Thus, $Cd(PTC)_2$ was shown to be a good single-source precursor for the low-temperature deposition of epitaxial CdS shells on

the surface of CdSe QBs.[10] In light of these results, we suspect that the PTC ligands utilized in

Weiss' experiments also deposited a shell or a shell-like layer on the surface of the QDs. A

shell-growth explanation matches the magnitude of the energetic shift observed in the absorption

spectra.
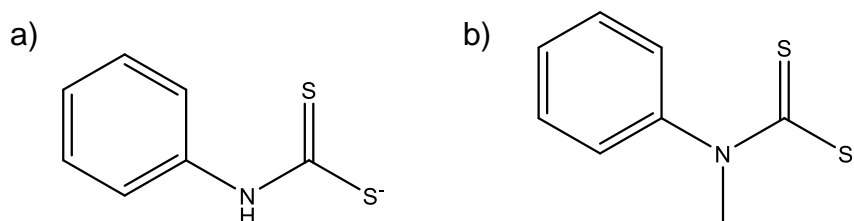
Figure 5.1   (a) Phenyldithiocarbamate (PTC) is a dithiocarbamate derived from a primary amine and is sucesptible to acid- and base- catalyzed decomposition. (b) *N*-methyl-*n*-phenyldithiocarbamate (MePhDTC), derived from a secondary amine, is only susceptible to acid-catalyzed decomposition.

PTC and Cd(PTC)$_2$ belong to a class of compounds more generally known as

dithiocarbamates (DTCs). As mentioned, dithiocarbamates synthesized from primary amines,

such as aniline, are known to decompose under both acidic and basic conditions. When

dithiocarbamate compounds are synthesized from secondary amines, they are no longer

susceptible to base-catalyzed decomposition.[9] Examples of dithiocarbamates derived from

primary and secondary amines are shown in Figure 5.1. By replacing the hydrogen on the

nitrogen of the DTC functional group with an organic substituent, the base-catalyzed degradation

pathway is eliminated (eq 1, Chapter 4). If kept under neutral or basic conditions, we suspected

that metal dithiocarbamates (M(DTC)$_2$s; see List of Abbreviations on pg. ix) derived from

secondary amines could be installed as Z-type ligands in a facile, reversible L-for-Z ligand

exchange on the surface of wurtzite CdSe QBs, analogous to previous ligand exchange

experiments conducted with Cd(oleate)$_2$.
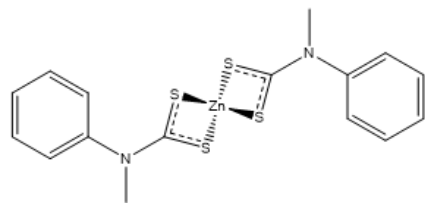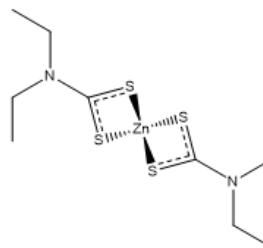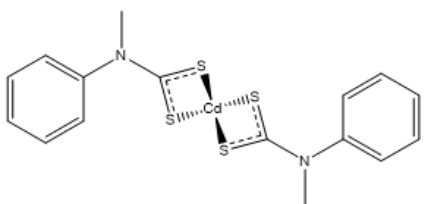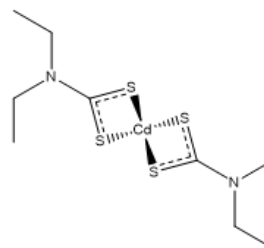
Figure 5.2 Metal Dithiocarbamates for study as Z-type Ligands. M(DTC)$_2$ refers to the general structure of metal dithiocarbamates and is pluralized M(DTC)$_2$s to refer to multiple ligands of this classification. (See List of Abbreviations on pg. ix in the front matter of this dissertation.)

We prepared four M(DTC)$_2$s from secondary amines, shown in Figure 5.2: zinc diethyldithiocarbamate (Zn(Et$_2$DTC)$_2$), zinc *n*-methyl-*n*-phenyldithiocarbamate (Zn(MePhDTC)$_2$), cadmium diethyldithiocarbamate (Cd(Et$_2$DTC)$_2$, and cadmium *n*-methyl-*n*-phenyldithiocarbamate (Cd(MePhDTC)$_2$). These ligands were prepared with the intention of installing them as Z-type ligands on the surface of wurtzite CdSe QBs, via L-for-Z ligand exchange. These complexes were deliberately chosen to compare the effects of the organic substituents on the energies of the features in the absorption spectra of wurtzite CdSe QBs. DFT calculations performed on PTC, an X-type ligand, predicted that PTC would be an effective hole delocalizing ligand when installed on the surface of zinc blende CdSe QDs.[3, 11] This installation

would result in the features of the absorption spectrum of the QDs shifting to lower energy relative to their original positions. These calculations predicted that the phenyl group significantly contributed to the hole-delocalized effect.[3] Thus, we hypothesized that the $M(MePhDTC)_2$ ligands in our series would result in larger bathochromic shifts relative to their $M(Et_2DTC)_2$ counterparts.

We chose to test both $Cd(DTC)_2$ and $Zn(DTC)_2$ derivatives because of the experiments conducted by Zhou et al.[2] In that study, the effects of replacing primary amine-native ligation with two Z-type ligands, $Cd(oleate)_2$ and $Zn(oleate)_2$, on the spectral properties of wurtzite CdSe QBs were investigated. The installation of both Z-type ligands resulted in bathochromic shifts of the features of wurtzite CdSe QBs in the absorption spectra. The shifts observed in the spectra of $Cd(oleate)_2$ ligated belts, however, were far greater in magnitude compared to those observed in $Zn(oleate)_2$ ligated belts (140 ± 20 meV compared to 30 ± 20 meV, respectively). Zhou et al stated that, once installed on the surface of the CdSe QBs, the cadmium ions of the $Cd(oleate)_2$ ligands were able to effectively extend the crystal lattice of the CdSe belts, thus enlarging the quantum-confined dimension of the CdSe QBs, whereas the Zn ions of $Zn(oleate)_2$ ligands were not able to extend the lattice.[2] The shifting observed in the absorption spectra of the $Zn(oleate)_2$ ligated QBs was attributed to changes in the lattice strain state, relative to the strain state of the $\{CdSe[n\text{-alkylamine}]_{0.53}\}$ QBs.[2]

Given the body of literature devoted to the delocalizing capacity of PTC[3-5, 7, 11] and the dramatic shifts to lower energies observed in the absorption spectra of ligand exchange experiments with $Cd(oleate)_2$,[2] we anticipated that exchange with $Cd(MePhDTC)_2$ would result in the largest shifts to lower energies in the absorption and photoluminescence spectra, compared to other $M(DTC)_2$s in Figure 5.2. This ligand shares characteristics with $Cd(oleate)_2$ and PTC.

Cd(MePhDTC)$_2$ and Cd(oleate)$_2$ contain a cadmium metal center, while Cd(MePhDTC)$_2$ and PTC are fully conjugated dithiocarbamates, which is predicted to be an important contributor to the hole-delocalizing capacity.[3, 11] Ultimately, the results obtained from ligand exchanges performed with M(DTC)$_2$s do not follow many of the trends evident in other MX$_2$ exchange experiments,[1-2] nor does Cd(MePhDTC)$_2$ appear to more dramatically affect the optoelectronic behavior of CdSe QBs when compared to other M(DTC)$_2$ utilized in this chapter. We discuss key differences between the M(DTC)$_2$ ligands used in these experiments and other Z-type ligands that appear in the literature and scrutinize possibilities regarding the nature of the ligand – nanocrystal interaction.

5.2   Experimental

5.2.1   Materials and General Procedures

All experimental procedures were performed under ambient conditions unless otherwise specified. Deuterated solvents were purchased from Cambridge Isotope Laboratories, Inc. Ammonium *n*-methyl-*n*-phenyldithiocarbamate NH$_4$MePTC,[5, 12] and wurtzite{CdSe[*n*-octylamine]$_{0.53}$} QBs[13] were synthesized according to literature procedures. Diethylammonium dithiocarbamate was purchased from TCI. Solvents were dried and prepared according to procedures outlined in Chapter 2.

5.2.2   Preparation of Metal Dithiocarbamate Compounds

The syntheses of bis(*n*-methyl-*n*-phenydithiocarbamato) cadmium(II) (Cd(MePhDTC)$_2$), bis(*n*-methyl-*n*-phenydithiocarbamato) zinc(II) (Zn(MePhDTC)$_2$), and bis(diethyldithiocarbamato) cadmium(II) (Cd(Et$_2$DTC)$_2$) were adapted from literature procedures.[14] Bis(diethyldithiocarbamato) zinc(II) (Zn(Et$_2$DTC)$_2$) was purchased and used as

received. In brief, a solution of Cd(acetate)$_2$·2H$_2$O (802 mg, 3.0 mmol) or Zn(acetate)$_2$·2H$_2$O (568 mg, 2.6 mmol) in methanol (25 mL) was added dropwise to a continuously stirred solution of NH$_4$MePhDTC (1.000 mg, 5.0 mmol) in methanol (50 mL) or diethylammonium diethyldithiocarbamate (1.5264 mg, 6.8 mmol) in methanol. A white or off-white precipitate formed shortly after addition. The solutions were stirred for 30 min at 0 °C. At that time, the precipitate was vacuum filtered and washed with ice-chilled water (25 mL × 1) and ice-chilled ethanol (200 proof, 25 mL × 3). The products, Cd(MePhDTC)$_2$, Zn(MePhDTC)$_2$, and Cd(Et$_2$DTC)$_2$, white and off-white powders, were dried under vacuum (8 h).

Cd(Et$_2$DTC)$_2$ Yield 1.187 g (2.9 mmol, 96%). UV-Visible (THF) λ_{max}, nm: 260 (Figure C.1 in Appendix C). IR, cm^{-1}: 1491 ν_s(C=N), 1143 σ(C-N-C), 986 ν_{as}(C-S) (Figure C.2 in Appendix C). ^{1}H NMR (500 MHz, DMSO-*d6*, δ) 3.830 (q, *J* = 7.00, 8H); 1.22 (t, *J* = 7.05 Hz, 12H). ^{13}C{^{1}H} NMR (125 MHz, DMSO-*d6*, δ) 203.8, 50.5, 12.4. Lit: IR, cm^{-1}: 1495 υ (C = N); 970 υ (C = S).[15]

Cd(MePhDTC)$_2$. Yield 0.825 g (1.7 mmol, 69%). UV-Visible (THF) λ_{max}, nm: 263 (Figure C.1). IR, cm^{-1}: 1489 ν_s(C=N), 1198 σ(C-N-C), 962 ν_{as}(C-S) (Figure C.2). ^{1}H NMR (500 MHz, DMSO-*d6*, δ) 3.79 (q; *J* = 7.1 Hz, 4H), (t, *J* = 7.34 Hz, 2H). ^{13}C{^{1}H} NMR (125 MHz, DMSO-*d6*, δ) 208.9, 148.6, 129.6, 126.4, 48.7. *Lit:* ^{1}H NMR (DMSO-*d6*, δ) 7.46–7.19 (m, 10H, -C6H5), 3.64 (s, 6H, -CH3). ^{13}C{^{1}H} NMR (DMSO-*d6*, δ) 148.55, 129.39, 128.79, 126.44 (-C6H5), 45.40 (-CH3), 202.10 (-CS2).[16]

Zn(MePhDTC)$_2$ Yield 0.712 g (1.7 mmol, 67%). UV-Visible (THF) λ_{max}, nm: 266 (Figure C.1). IR, cm^{-1}: 1491 ν_s(C=N), 1108 σ(C-N-C), 966 ν_{as}(C-S) (Figure C.2). ^{1}H NMR (500 MHz, DMSO-*d6*, δ) 7.55 (d, *J* = 7.34 Hz, 4H), 7.35 (t; *J* = 7.58 Hz, 4H), 7.18 (t, *J* = 7.34 Hz, 2H). ^{13}C{^{1}H} NMR (125 MHz, DMSO-*d6*, δ) 207.5, 147.5, 129.7, 128.2, 126.4., 47.5. *Lit*: ^{1}H

NMR (DMSO-d_6, δ) 7.46 – 7.19 (m, 10H, –C6H5), 3.64 (s, 6H, –CH3). ^{13}C{^{1}H NMR (DMSO-d_6, δ) 147.17, 129.55, 127.81, 126.31(-C6H5), 47.24(-CH3), 190.51(-CS2).[16]

5.2.3   Monitoring the Stability and Solubility of Metal Dithiocarbamates

The stability of each M(DTC)$_2$ compound was investigated by ^{1}H NMR and ^{13}C NMR in toluene, dichloromethane, dimethylformamide and dimethyl sulfoxide prior to ligand exchange. NMR spectra were acquired from freshly prepared solutions of M(DTC)$_2$s. NMR spectra were acquired again after 12h and inspected for signs of decomposition. The experiment was repeated with new solutions, which were held at 40 °C for 4h. (See Table C.1 in Appendix C).

5.2.4   Ligand Exchange Procedures.

Preparation of Stock Solutions. Stock solutions (25 – 50 mL) of M(DTC)$_2$ were prepared at concentrations of 10 mg/mL in dry toluene, dichloromethane, dimethylsulfoxide, or dimethylformamide, according to solubility (see Table C.1). Solutions were sonicated for 15 minutes prior to use to ensure dissolution.

Direct Exchange. An aliquot (0.20 mL) of crude (as-synthesized, unpurified) {CdSe[n-octylamine]$_{0.53}$} QB solution was unbundled according to literature procedures[13] using n-oleylamine to yield {CdSe[n-alkylamine]$_{0.53}$}. The amine-passivated QB solution was washed via centrifugation 4-6× in dry toluene, and resuspended in an aliquot (1 mL) of M(DTC)$_2$ stock solution. The mixture was allowed to sit at ambient temperature for 5 min, at which time the {CdSe[n-alkylamine]$_x$[M(DTC)]$_y$} were precipitated from solution via centrifugation (2500 RPM, 3 min). The supernatant was discarded and the pellet of {CdSe[n-alkylamine]$_x$[M(DTC)]$_y$} QBs was then resuspended in another aliquot of M(DTC)$_2$ stock solution. The process was repeated until the 1$_B$-1$_e$ and 1$_A$-1$_e$ transitions in the absorption spectra ceased to shift to lower energies. The final pellet was resuspended and stored in dry toluene for all cases. All

spectroscopic measurements were performed in dry toluene. All samples were stored in test tubes capped with a rubber stopper, purged with N_2, and wrapped in parafilm when not in use.

Step-wise $L \rightarrow Z_1 \rightarrow Z_2$. An aliquot (0.20 mL) of crude {CdSe[n-octylamine]$_{0.53}$} belt solution was unbundled according to literature procedures[13] using n-oleylamine to yield {CdSe[n-alkylamine]$_{0.53}$}. The QB solution was washed three times in dry toluene and resuspended in a solution of 0.11 M Cd(oleate)$_2$ (Z_1) in n-octadecene to produce {CdSe[Cd(oleate)$_2$]$_{0.26}$} QBs.[2, 17] The {CdSe[Cd(oleate)$_2$]$_{0.26}$} QBs were washed three times via centrifugation (2500 RPM, 3 min) using dry toluene (1 mL) and methanol (0.5 mL) as flocculants. After the final wash, the {CdSe[Cd(oleate)$_2$]$_{0.26}$} QBs were resuspended in an aliquot of M(DTC)$_2$ (Z_2) stock solution to produce {CdSe[Cd(oleate)$_2$]$_{(x-y)}$[M(DTC)]$_y$} QBs. The {CdSe[Cd(oleate)$_2$]$_{(x-y)}$[M(DTC)]$_y$} QBs were isolated via centrifugation (2500 RPM, 3 min) and resuspended in an additional aliquot of M(DTC)$_2$ stock solution. For dichloromethane mixtures, an addition of heptane (up to 50% of the total volume) was necessary to precipitate the belts. The process was repeated until the 1_B-1_e and 1_A-1_e transitions in the absorption spectra ceased to shift to lower energies. Final solutions were prepared for spectroscopy in dry toluene. All samples were stored in test tubes capped with a rubber stopper, purged with N_2, and wrapped in parafilm when not in use.

Back Exchange to Primary Amine. The reversibility of the direct and step-wise exchanges described above were tested by modified literature procedures.[2] Neat n-octylamine (0.5 mL) was added to an aliquot (0.5 mL) of the {CdSe[M(DTC)$_2$]} solution. A single centrifugation step (2500 RPM, 3 min) was undertaken to isolate the CdSe QBs, which were then resuspended in dry toluene. Absorption and PL spectra were collected. The exchange was

considered reversible if the features in the absorption and photoluminescence spectra returned to the energies observed in the as-synthesized {CdSe[n-octylamine]$_{0.53}$} QBs.

5.3   Results

5.3.1   Solubility and Stability of M(DTC)$_2$s

Prior to conducting any exchange experiments, the solubility and stability characteristics of all M(DTC)$_2$ ligands were established. Experiments were conducted to test the solubility of each M(DTC)$_2$ in a variety of anhydrous solvents and to ensure that all four ligands were stable for the duration of the spectroscopic investigation. M(DTC)$_2$ compounds were determined to be sufficiently soluble at concentrations $\geq$10 mg/mL. Zn(Et$_2$DTC)$_2$ and Cd(Et$_2$DTC)$_2$ were found to be soluble in toluene, dichloromethane, dimethyl formamide, dimethylsulfoxide. Zn(MePhDTC)$_2$ and Cd(MePhDTC)$_2$ were found to only be sufficiently soluble in dimethylformamide and dimethylsulfoxide. The stability of each of the M(DTC)$_2$ compounds in each solvent system was investigated by ^{1}H NMR and ^{13}C NMR prior to ligand exchange. NMR spectra were acquired from freshly prepared solutions of M(DTC)$_2$s in toluene, dichloromethane, dimethylformamide and dimethyl sulfoxide, according to the solubility described earlier in this paragraph. NMR spectra were acquired again after 12h and inspected for signs of decomposition, the products of which would appear as unidentified or new signals in the NMR spectra. The experiment was repeated with new solutions, which were held at 40 °C for 4h. No evidence of decomposition was found, and the results are summarized in Table C.1 in Appendix C.

5.3.2   Direct Exchange

Direct-exchange experiments were undertaken to investigate the replacement of primary amines on the surface of CdSe QBs with M(DTC)$_2$s. The goal of these experiments was to achieve complete M(DTC)$_2$ ligation while introducing as few other species as possible (to

mitigate any complication from additional variables). M(DTC)$_2$ stock solutions were prepared with concentrations of 10 mg/mL in toluene, dichloromethane, dimethylformamide, and dimethylsulfoxide, as permitted by the solubility of each M(DTC)$_2$. {CdSe[n-octylamine]$_{0.53}$} QBs were prepared according to a previously reported synthesis.[13] An aliquot (0.2 mL) of the crude QB solution was washed 4-6× in anhydrous toluene to remove excess amine. The QBs were resuspended in 1 mL of M(DTC)$_2$ stock solution and allowed to react for 5 min. A concentration of 10 mg/mL M(DTC)$_2$ and 0.2 mL of crude stock solution ensures there are roughly 20-30 times the number of M(DTC)$_2$ ligand per surface binding site (assuming one M(DTC)$_2$ for each surface selenium).[2] Initial attempts showed no change in the absorption spectra, despite repeated efforts, and minimal change in the FT-IR spectra.
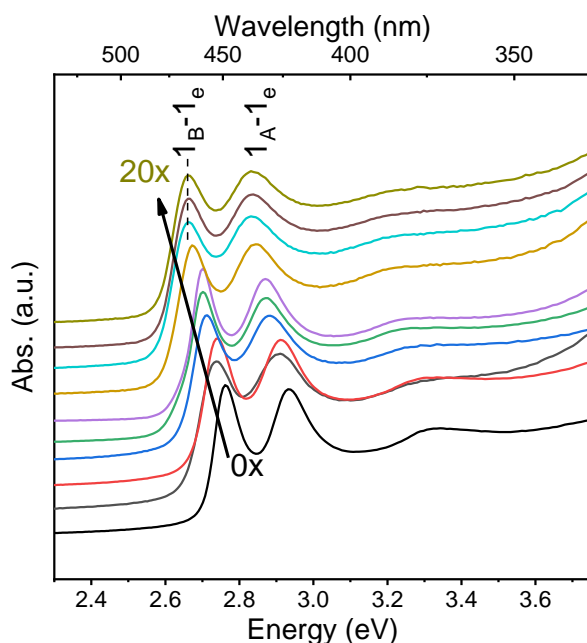
Figure 5.3   Gradual shifting of the absorption spectra upon repeated exposure of unbundled CdSe[n-alkylamine]$_{0.53}$ to Zn(Et$_2$DTC)$_2$ solution.

Experiments were undertaken to test the direct-exchange procedure with unbundled CdSe QBs. {CdSe[n-octylamine]$_{0.53}$} QBs were unbundled overnight using n-oleylamine, according to

literature procedures.[13] The surface composition of the "unbundled QBs" was a mixture of *n*-oleylamine and *n*-octylamine, referred to hereafter as *n*-alkylamine. The QBs were washed in toluene 4-6× to remove excess, unbound primary amine,[2] and resuspended in 1 mL of $M(DTC)_2$ stock solution. The mixture allowed to react for 5 min, and then precipitated via centrifugation. The supernatant was removed, and the QBs were resuspended in a fresh aliquot (1 mL) of stock solution. This constituted one "cycle" of ligand exchange. Modest shifts of the two lowest-energy features in the absorption spectra, the 1_B-1_e and 1_A-1_e transitions, to lower energies were observed after each cycle of ligand replacement. Figure 5.3 includes the absorption spectra of the exchange of *n*-alkylamine for $Zn(Et_2DTC)_2$, with the ligand replacement procedure performed 20 times. The exchange was considered complete when repeated attempts produced no further changes in the shapes or energetic positions of the peaks. The gradual shifting of the first and second absorption feature observed upon exchange of *n*-alkylamines for $Zn(Et_2DTC)_2$ is also observed for amine-to-$M(DTC)_2$ replacement with $Zn(MePTC)_2$, $Cd(Et_2DTC)_2$, and $Cd(MePTC)_2$.

Representative absorbance and PL spectra in Figures 5.4a and 5.4b illustrate the reversibility of the exchange of primary amine for $M(DTC)_2$ ligands using $Zn(Et_2DTC)_2$ in this example. In Figure 5.4a, the absorption spectrum of the unbundled, amine-passivated QBs is shown in black. After 20 cycles of ligand exchange (red), the lowest energy peak has shifted to lower energy by 100 eV. Upon a single exposure to *n*-octylamine, the 1_B-1_e and 1_A-1_e peaks shift back to their original positions (blue). Normalized PL spectra of the CdSe QBs are shown in Figure 5.4b. The emission spectrum of {CdSe[*n*-alkylamine]$_{0.53}$} is shown in black. After 20× exchange with $Zn(Et_2DTC)_2$, the PL spectrum ceased to move to lower energy, and appeared broadened relative to the initial, amine-ligated QB PL spectrum (blue). Notably, there is minimal

trap emission. Upon exposure to 0.5 mL n-octylamine, the peak returns to its original position with no trap emission, demonstrating the full reversibility of the reaction. Trap emission refers to emission below the band-edge,[18-20] which arises from an unintentionally introduced defects. Trap emission commonly, but not always, arises from potential energy minima on the surface created by 'dangling bonds,' as described in the Chapter 1 (Section 1.3.1). The absence of trap emission is an indirect indicator of the 'completeness' of the ligand exchange reaction. The absence of trap emission in the PL spectra presented in 5.4b indicates few dangling bonds are present on the surface of the CdSe QBs in these experiments. Stated differently, the majority of available coordination sites on the surface of the QBs are occupied.

Figure 5.4c displays the absorption spectra of all four M(DTC)$_2$-ligated QBs, with features shifted to lower energies relative to the features of{CdSe[n-octylamine]$_{0.53}$} QBs. A representative TEM image of {CdSe[Zn(Et$_2$DTC)$_2$]$_x$} is shown in Figure 5.4d, illustrating that the overall belt-like morphology was retained. The thickness and width of the QB structures were retained in all cases of M(DTC)$_2$ exchange, although some breakage was observed, shortening the average length of the QBs compared to their as-synthesized, primary amine-ligated counterparts. The shortening of the QBs is expected with repeated flocculation cycles, because of the mechanical agitation inherent to the process of centrifugation.

The repeated flocculation of the QBs and replacement of the M(DTC)$_2$ solution was necessary to achieve the maximum magnitude of energetic shifting in the optical spectra. Simply soaking the {CdSe[n-alkylamine]$_x$} QBs in a concentrated solution of M(DTC)$_2$ (for up to 12 h) failed to produce significant shifting in the absorption spectra, indicating that removal of free n-alkylamine (primary amine that had been liberated from the surface of the CdSe QB) was necessary to drive the exchange. Modest heating (40 °C) was found to slightly encourage ligand

replacement, but higher temperatures (>50 °C) led to inconsistent results, including shifting of the features in the absorption spectra to higher and lower energy. Heating dithiocarbamates accelerates decomposition,[9] thus all trials included in the data presented within this chapter were conducted at room temperature.
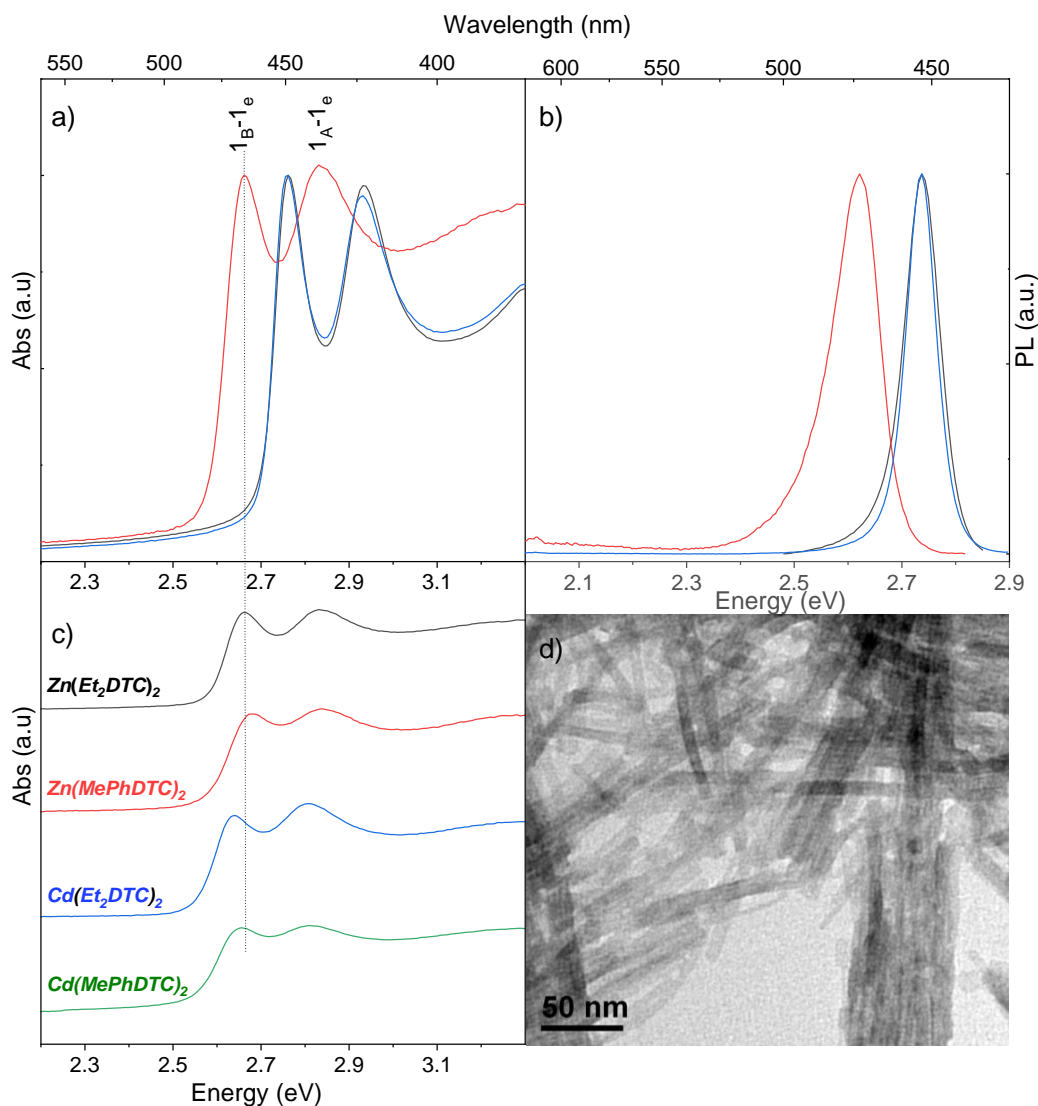
Figure 5.4 Absorption, PL Spectra and TEM images of $Zn(Et_2DTC)_2$ Ligated QBs. (a) Normalized UV-Vis absorption spectra of unbundled {$CdSe[n\text{-alkylamine}]_{0.53}$} QBs prior to exchange (black), 20× ligand cycles with $Zn(Et_2DTC)_2$ (red), and upon reverse-exchange with *n*-octylamine (blue). (b) Normalized PL spectra of unbundled $CdSe[n\text{-alkylamine}]_{0.53}$ QBs prior to exchange (black), 20× ligand cycles with $Zn(Et_2DTC)_2$ (red), and upon reverse-exchange with *n*-octylamine (blue). (c) Absorption spectra of $CdSe[M(DTC)_x]$ QBs obtained via direct exchange (d) representative TEM images of {$CdSe[Zn(Et_2DTC)_2]_x$}. Additional TEMs are in Figure C.3 of Appendix C.

111

5.3.3 L-Z_1-Z_2 Exchange

While the single-step L-Z_1 direct-replacement experiments were successful, the procedure was slow and inefficient for all four of the $M(DTC)_2$ ligands. With the goal of improving the efficiency of the ligand exchange, we undertook two-step L-Z_1-Z_2 ligand-replacement experiments. In 2015, Yang et al reported primary amine molecules bound to the surface of wurtzite CdSe QBs are rapidly and completely replaced by $Cd(oleate)_2$ (Z_1).[2] In the L-Z_1-Z_2 experiments described herein, we utilized the facile, immediate replacement of *n*-alkylamine with $Cd(oleate)_2$ (Z_1), which was then replaced by $M(DTC)_2$ (Z_2) in a second step. We used the energetic shifting 1_A-1_e and 1_B-1_e absorption features as evidence for ligand exchange. The $\{CdSe[Cd(oleate)_2]\}$ QBs underwent multiple exposures of Z_2 until no additional shifting was observed. Each exposure and subsequent purification constituted a "ligand-exchange" cycle. Three ligand-exchange cycles were generally sufficient, but as many as five cycles were utilized when exchanging $Cd(oleate)_2$ for $Cd(Et_2DTC)_2$.

In the experiments performed for this chapter, the 1_B-1_e feature observed in the spectrum of $\{CdSe[Cd(oleate)_2]_{0.26}\}$ QBs (red spectra in Figure 5.5a and 5.5b) was shifted to lower energies by 151 ± 5 eV relative to the 1_B-1_e feature in the spectrum of $\{CdSe[n\text{-alkylamine}]_{0.53}\}$ QBs, which is within the error of the 140 ± 20 meV previously reported.[2] Successful L-Z_1-Z_2 exchange with $Zn(Et_2DTC)_2$ resulted in the spectral features shifting to higher energies (blue), relative to the spectra of the intermediate $\{CdSe[Cd(oleate)_2]_x\}$ QB species. The spectra of the $\{CdSe[Zn(Et_2DTC)_2]_x\}$ QBs obtained via direct exchange (green) and CdSe[*n*-alkylamine]$_{0.53}$ QBs (black) are shown for comparison.
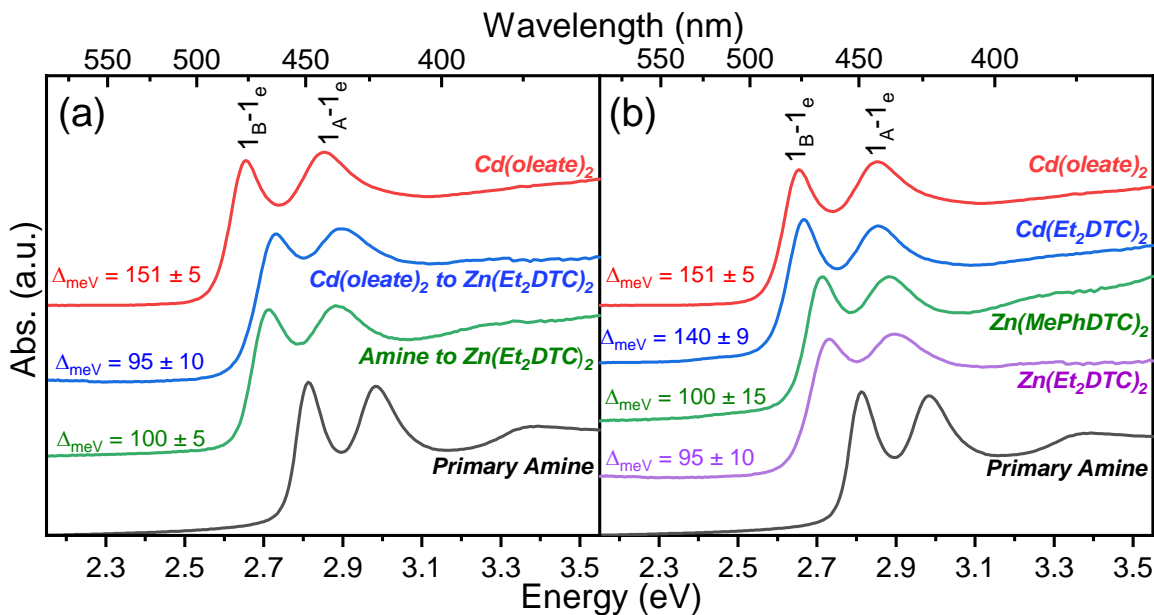
Figure 5.5 L-Z_1-Z_2 exchange. (a) Example of L-Z_1-Z_2 ligand exchange with L = n-alkylamine, Z_1 = Cd(oleate)$_2$ and Z_2 = Zn(Et$_2$DTC)$_2$. Δ_{meV} is the change in energy of the 1_B-1_e feature of ligand-exchanged belts relative to the energetic position of the 1_B-1_e feature in the absorption spectrum of {CdSe[n-octylamine]$_{0.53}$} QBs. Initially, n-alkylamine is exchanged for Cd(oleate)$_2$ on the surface of the CdSe QBs (black and red spectra, respectively). The 1_B-1_e feature shifts by 151 meV to lower energies. Cd(oleate)$_2$ is exchanged for Zn(Et$_2$DTC)$_2$, which shifts to higher energies relative to Cd(oleate)$_2$. Absorption spectrum of {CdSe[Zn(Et$_2$DTC)$_2$]$_x$} (green) QBs obtained via direct exchange is shown for comparison. (b) Spectra obtained from L-Z_1-Z_2 ligand exchange with L = n-alkylamine (black), Z_1 = Cd(oleate)$_2$ (red) and Z_2 = Cd(Et$_2$DTC)$_2$, Zn(MePhDTC)$_2$, and Zn(Et$_2$DTC)$_2$. Errors were obtained from the standard deviation of the average of three trials of the procedure.

L-Z_1-Z_2 exchanges were reproducible using the Z_2 ligands Zn(Et$_2$DTC)$_2$, Zn(MePhDTC)$_2$ and Cd(Et$_2$DTC)$_2$, meaning that multiple trials of each L-Z_1-Z_2 exchange yielded absorption spectra with features of similar shapes and energies. In each case, the features in the absorption spectra of {CdSe[M(DTC)$_2$]} QBs shifted to higher energies relative to the features observed in the absorption spectrum of {CdSe[Cd(oleate)$_2$]}, and produced absorption spectra comparable to the absorption spectra obtained via direct exchange. These similarities suggest that the two ligand-exchange methods, direct and L-Z_1-Z_2, of M(DTC)$_2$ yield comparable results. Additional evidence and more detail for this claim are given in Section 5.3.4 and 5.3.5.

The exchange of $Cd(oleate)_2$ (Z_1) for $Cd(MePhDTC)_2$ (Z_2) resulted in inconsistent energetic shifting of the 1_B-1_e feature observed in the absorption spectra. In some trials, the 1_B-1_e feature in the absorption spectrum of $\{CdSe[Cd(MePhDTC)_2]\}$ QBs was shifted to lower energies relative to the 1_B-1_e feature in the spectrum $\{CdSe[Cd(oleate)_2]\}$ QBs. In other trials, the 1_B-1_e feature in the spectrum of $\{CdSe[Cd(MePhDTC)_2]\}$ QBs was shifted to higher energies relative to the 1_B-1_e feature in the spectrum of $\{CdSe[Cd(oleate)_2]\}$. Still yet, other trials failed to produce a shift at all, relative to the energies of the 1_B-1_e feature observed in the spectrum of $\{CdSe[Cd(oleate)_2]\}$. For that reason, the L-Z_1-Z_2 experiments with $Z_2 = Cd(MePhDTC)_2$ are excluded from our analysis.

5.3.4   Comparing Direct and L-Z_1-Z_2 exchange in the UV-Vis Absorption Spectra

Comparisons of the shifting of the absorption spectra observed in direct and L-Z_1-Z_2 exchanges are shown in Figure 5.6 for the four $\{CdSe[M(DTC)_2]_x\}$ cases. Table 5.1 lists values of the shifts observed in the absorption spectra of $\{CdSe[M(DTC)_2]_x\}$ obtained via direct and L-Z_1-Z_2 exchange, as well as the values of the shifts obtained from a global fit of the direct-exchange data (Section C.1 in Appendix C). In Figure 5.6, the energies of the 1_B-1_e and 1_A-1_e transitions are shown by the black squares and red circles, respectively, for the $\{CdSe[M(DTC)_2]\}$ QBs obtained via direct exchange. We observe a gradual shift to lower energies with increasing exposure to $M(DTC)_2$. In each of the direct $M(DTC)_2$ exchange experiments, the position of the 1_B-1_e peak asymptotically approaches ~2.65 eV, while the position of the 1_A-1_e peak approach 2.83 and 2.80 eV in the $Zn(DTC)_2$ and $Cd(DTC)_2$ exchange experiments, respectively.

114
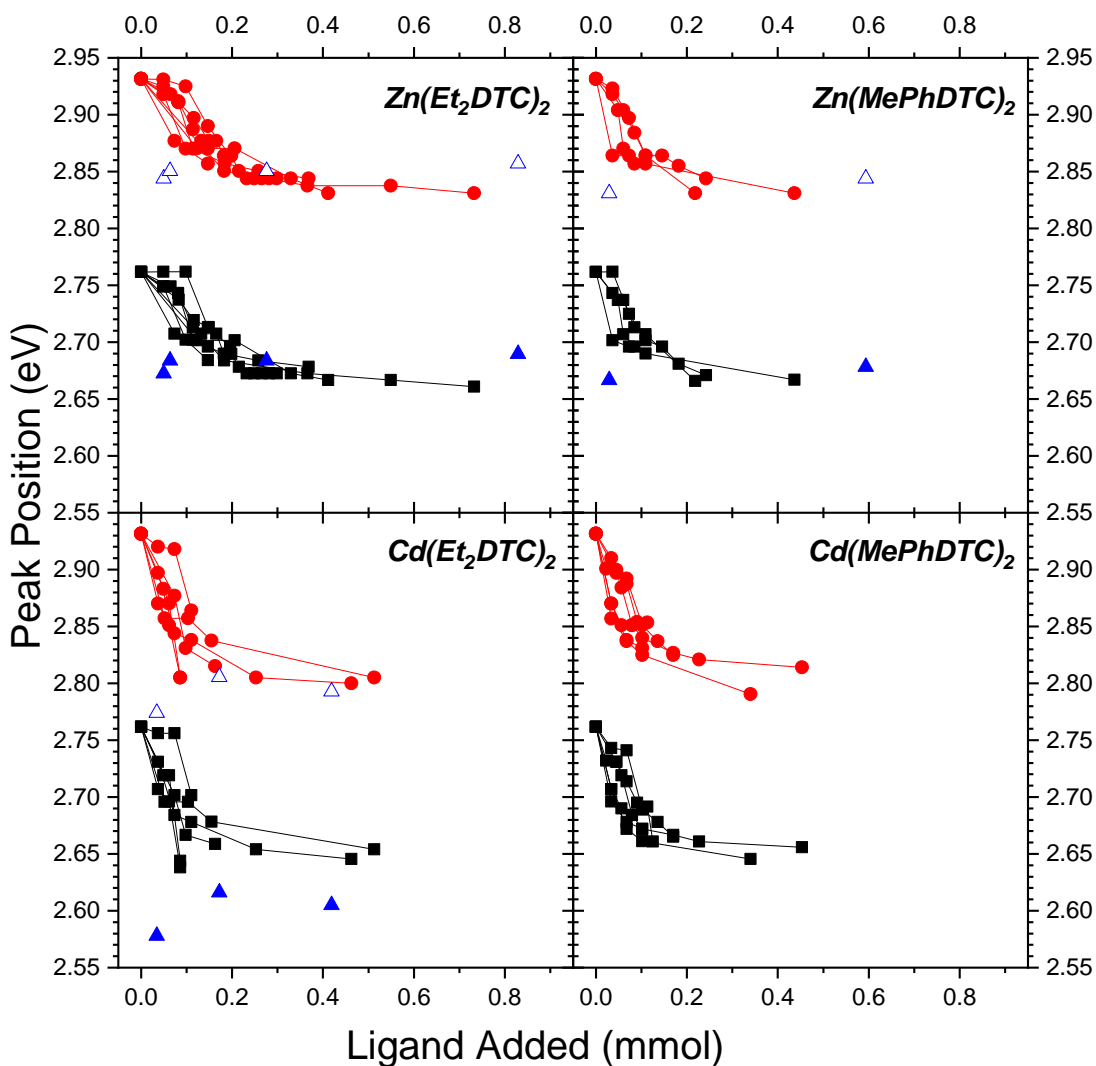
Figure 5.6   Energetic shifting of the 1_B-1_e and 1_A-1_e transitions of CdSe QBs as a function of ligand added. For the direct exchange, the energies of the 1_B-1_e and 1_A-1_e peaks are shown by the black squares and red circles, respectively, showing a gradual shift to lower energies with increasing exposure to $M(DTC)_2$. For the L-Z_1-Z_2 exchange, the energies of the 1_B-1_e and 1_A-1_e peaks are represented by the solid and open blue triangles, respectively.

In the L-Z_1-Z_2 exchange, the locations of the 1_B-1_e and 1_A-1_e are shown by blue closed

and open triangles in Figure 5.6, respectively. Compared to the direct exchanges, lower

concentrations of $M(DTC)_2$ were required to perform the L-Z_1-Z_2. exchanges. The energies of the

1_B-1_e and 1_A-1_e peaks obtained via direct and L-Z_1-Z_2 exchange are comparable in each case,

except for the $Cd(Et_2DTC)_2$ sample. The values obtained for the shift of the 1_B-1_e feature of the

$\{CdSe[Cd(Et_2DTC)_2]_x\}$ QBs for L-Z_1-Z_2 and direct exchange are not within error of each other.

The absorption spectra are sensitive to the presence of any remaining $Cd(oleate)_2$ ligand,[2] which

may suggest that $Cd(Et_2DTC)_2$ does not efficiently replace $Cd(oleate)_2$. This matches well with

the result that more exposure to $Cd(Et_2DTC)_2$ was required to complete the exchange (Section

5.3.3). In the next section, 5.3.5, residual $Cd(oleate)_2$ is evident in the FT-IR spectra of the final

$\{CdSe[Cd(Et_2DTC)_x]$ QBs obtained via L-Z_1-Z_2 exchange, further supporting this conclusion.

Because quantitative elemental analysis data were not obtained, it is not possible to quantify

relative displacement efficiencies, or determine the completeness of the L-Z_1-Z_2 exchanges. The

remainder of the discussion will focus on the data obtained for $Cd(Et_2DTC)_2$ obtained via direct

exchange.

Table 5.1 Energetic Shifting in Absorption spectra

Ligand	Direct Exchange Δ_{max}(meV)[a]		Direct Exchange Δ_{fit}(meV)[b]		L-Z_1-Z_2 Exchange Δ_{ave} (meV)[c]	
	1_B-1e	1_A-1_e	1_B-1e	1_A-1_e	1_B-1e	1_A-1_e
$Zn(Et_2DTC)_2$	100	100	100 ± 10	100 ± 10	95 ± 10	90 ± 13
$Zn(MePhDTC)_2$	95	100	100 ± 10	100 ± 10	100 ± 15	100 ± 15
$Cd(Et_2DTC)_2$	128	140	100 ± 10	120 ± 10	140 ± 9	126 ± 15
$Cd(MePhDTC)_2$	116	131	110 ± 10	120 ± 10	--	--

[a] maximum red-shift observed in the absorption spectra
[b] value obtained from exponential decay fit (Section C.2 in Appendix C)
[c] value given relative to peak positions observed in $\{CdSe[n\text{-}octylamine]_{0.53}\}$; errors were
obtained from the standard deviation of the average of three trials.

Unlike previous studies,[1-2, 21] the magnitude of the 1_B-1_e shift appears insensitive to the

identity of the metal center (Table C.2 in Appendix C). In previous studies on 1.8 nm thick

wurtzite CdSe QBs,[1-2, 21] the difference in energies of the 1_B-1_e feature between Cd and Zn

analogs (for example, $CdCl_2$ and $ZnCl_2$) ranged from 56-215 meV; in this study, the difference in

energy obtained from the maximum values of the shift between Cd and Zn analogs is 33 meV.

116

Global fitting of the direct-exchange data presented in Figure 5.6 reveals that all of the energies of the 1_B-1_e peaks fall within error of each other (see Section C.1 in Appendix C). This point will be addressed again in the Discussion Section.

The organic substituents (diethyl and methylphenyl) also seem to have minimal effect on the magnitude of the shift to lower energies observed in the absorption spectra. The maximum shifts obtained for the diethyl substituent were within error when compared to the shifts obtained for the methyl phenyl substituents. This is unexpected given the body of literature devoted to the charge delocalizing capacity of phenyldithiocarbmate[3-5] and will be revisited in Section 5.3.5.
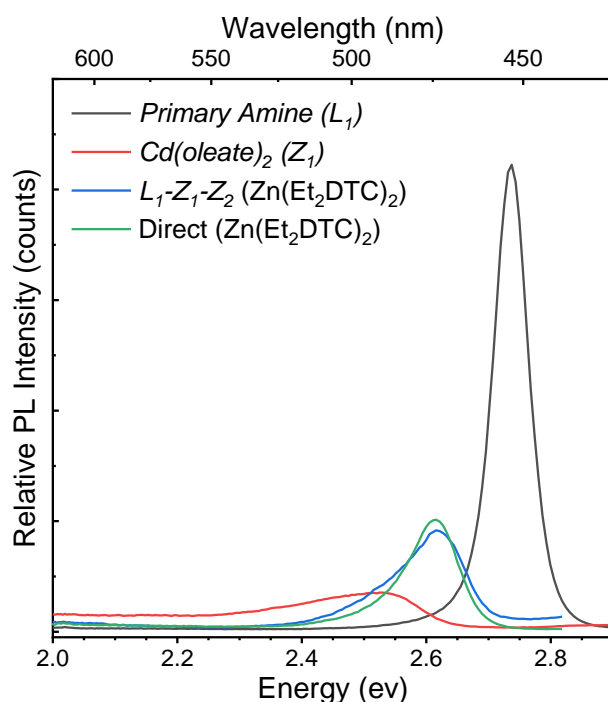
Figure 5.7   Dependence of the PL spectra on ligand and ligand-exchange method. The PL spectrum of {CdSe[n-alkylamine]$_{0.53}$} QBs (black), {CdSe[Cd(oleate)$_2$]$_{0.26}$} QBs (red), {CdSe[Zn(Et$_2$DTC)$_2$]$_x$} obtained via L-Z_1-Z_2 exchange (blue), and {CdSe[Zn(Et$_2$DTC)$_2$]$_x$} obtained via direct exchange (green).

The energy, intensity and shape of the PL peak of the {CdSe[Zn(DTC)$_2$]$_x$} QBs obtained by L-Z_1-Z_2 exchange closely approximates that of the PL peak of the {CdSe[Zn(DTC)$_2$]$_x$} QBs obtained by direct exchange. Figure 5.7 displays representative PL spectra {CdSe[n-

alkylamine]$_{0.53}$} QBs (black), {CdSe[Cd(oleate)$_2$]$_{0.26}$} QBs (red), {CdSe[Zn(Et$_2$DTC)$_2$]$_x$} QBs obtained via L-Z$_1$-Z$_2$ exchange (blue), and {CdSe[Zn(Et$_2$DTC)$_2$]$_x$} QBs obtained via direct exchange (green). The spectra have been normalized by the absorbance value at the excitation wavelength (3.31 eV, 375 nm) to show the relative emission intensities. The PL spectrum of {CdSe[n-alkylamine]$_{0.53}$} QBs is narrow and intense, with minimal trap emission. The PL spectrum of {CdSe[Cd(oleate)$_2$]$_{0.26}$} QBs (red) is characterized by its low intensity and broad low energy trap emission. The PL spectrum of {CdSe[Zn(Et$_2$DTC)$_2$]$_x$} QBs obtained via L-Z$_1$-Z$_2$ exchange shifts to higher energies relative to the PL spectrum of {CdSe[Cd(oleate)$_2$]$_x$}. The large trap emission associated with Cd(oleate)$_2$ ligation is diminished, and in the case of ligation with Zn(DTC)$_2$s, is fully reversible. The similarity of the PL spectra of {CdSe[Zn(Et$_2$DTC)$_2$]$_x$} QBs obtained via direct and L-Z$_1$-Z$_2$ ligand exchange supports the assertion that the methods yield comparable final products when Zn(DTC)$_2$s are utilized as the Z-type ligand.

5.3.5   Investigating Ligand Exchange and Surface Binding via FT-IR

The extent of direct and L-Z$_1$-Z$_2$ exchange was also monitored using FT-IR spectroscopy. The results are shown in Figure 5.8. In the cases of direct exchange, the absence of N-H stretches at ~3200 cm^{-1} and the presence of sharp, intense peaks in the fingerprint region indicate the exchange of primary amine for M(DTC)$_2$.

Cd(oleate)$_2$ ligation (purple) is easily recognized in the FT-IR by the intense symmetric and asymmetric stretches of the carboxylate group at 1536 and 1412 cm^{-1}, respectively. M(DTC)$_2$s (blue, green, purple) are characterized by sharp, intense peaks in the fingerprint region. Diminished carboxylate stretches and the appearance of sharp features in the fingerprint region indicate Z$_1$-Z$_2$ ligand replacement on the surface of the CdSe QBs. Some residual Cd(oleate)$_2$ does appear to remain bound to the surface of the QBs.
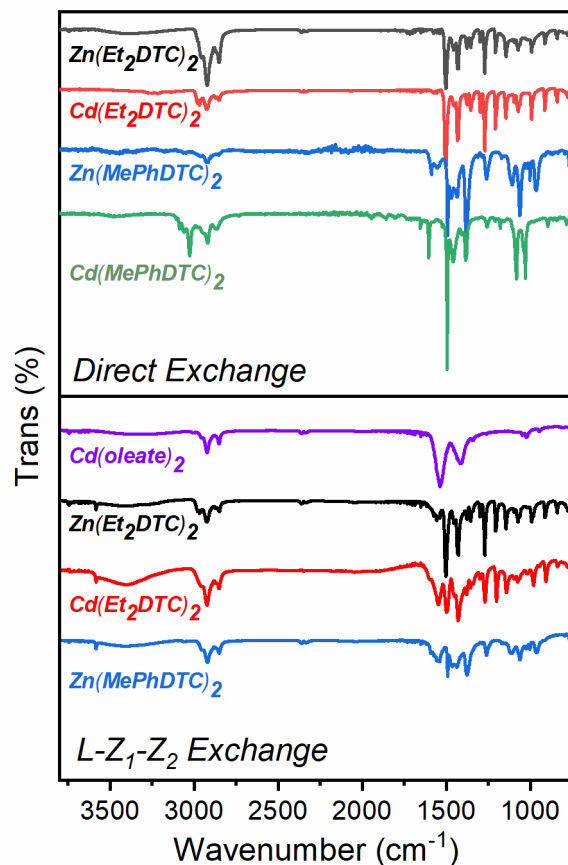
Figure 5.8 FT-IR Spectra of {Cd[M(DTC)$_2$]$_x$} QBs. (a) FT-IR spectra of {CdSe[M(DTC)$_2$]$_x$} QBs obtained via direct exchange. (b) FT-IR spectra of {CdSe[M(DTC)$_2$]$_x$} QBs obtained via L-Z$_1$-Z$_2$ exchange.

Analysis of the 'fingerprint' region of the FT-IR spectra of the M(DTC)$_2$s provides insight into how the M(DTC)$_2$ ligands change upon surface binding, and how the organic substituents of the dithiocarbamate functional group contribute to the electronic character of the ligand. Figure 5.9a displays the region of the FT-IR spectra of Zn(Et$_2$DTC)$_2$-ligated QBs obtained via direct exchange (black), L-Z$_1$-Z$_2$ exchange (red), L-Z$_1$-Z$_2$ exchange (Cd(oleate)$_2$ removed) (blue), and neat powder of Zn(Et$_2$DTC)$_2$. The highlighted regions are attributed to the C=N stretching (1500 cm^{-1}), C-N-C bending (1207 cm^{-1}) and C-S stretching modes (991 cm^{-1}) of Zn(Et$_2$DTC)$_2$.[22-23]

119
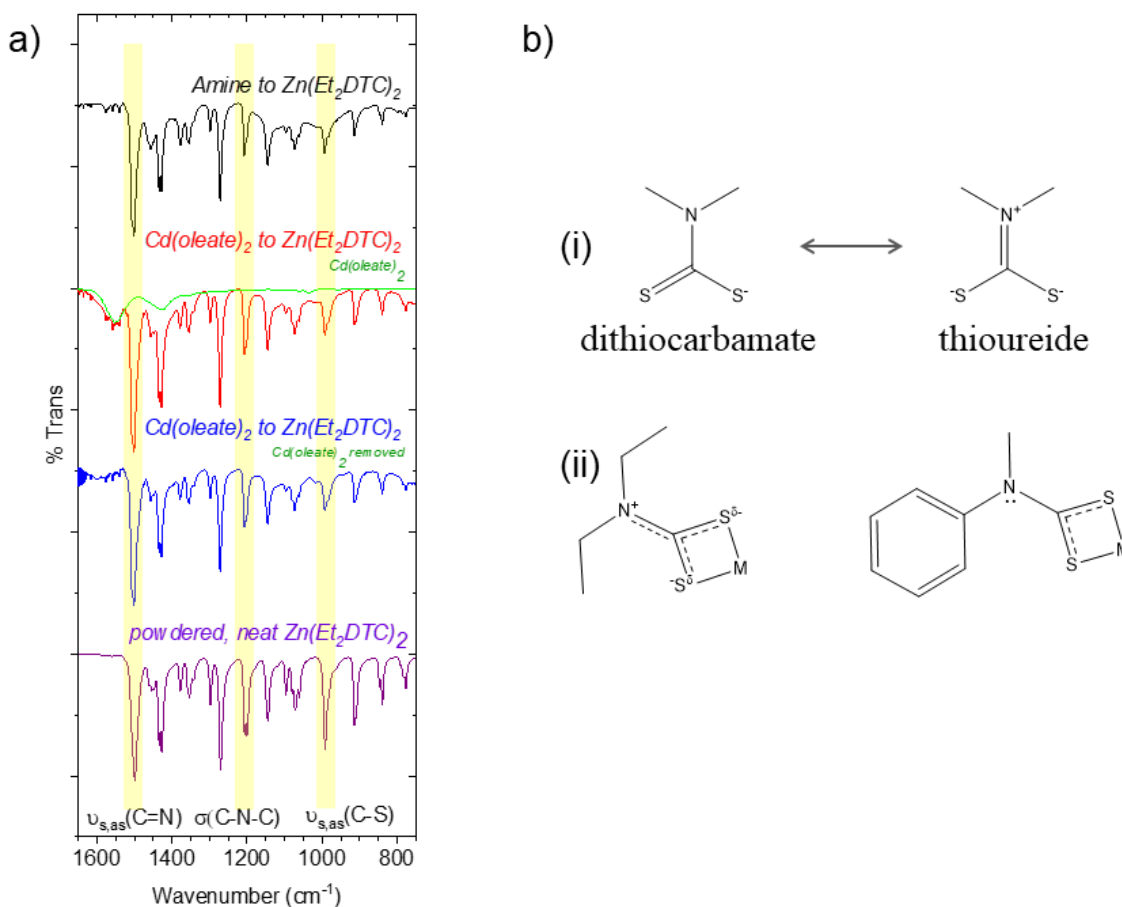
Figure 5.9 FT-IR Spectra of Zn(Et$_2$DTC)$_2$ exchanged QBs and resonance structure contributions. (a) Spectra of QBs obtained via direct exchange (black), L-Z$_1$-Z$_2$ exchange (red), L-Z$_1$-Z$_2$ exchange (Cd(oleate)$_2$ removed) (blue), and neat powder of Zn(Et$_2$DTC)$_2$. (b) (i) Dithiocarbamate and thioureide resonance structures; (ii) Thioureide resonance structure of M(Et$_2$DTC)$_2$ and dithiocarbamate resonance structure of M(MePhDTC)$_2$.

A comparison of the integrated intensities of C=N and C-N-C peaks provides insight into the relative contributions from the thioureide (C=N) and dithiocarbamate (C-N-C) resonance structures (Figure 5.9b). Table 5.2 summarizes the ratio of the integrated areas of the C-N-C/C=N peaks for all four M(DTC)$_2$ cases tested. Compared to the powdered, unbound form of Zn(Et$_2$DTC)$_2$ (purple), both direct (black) and L-Z$_1$-Z$_2$ exchange (red) QB samples show a significantly greater contribution from the thioureide resonance structure. While the mechanism

of ligand replacement in direct and L-Z_1-Z_2 exchanged samples is different (L-for-Z vs. Z-for-Z'), the method of installation of Zn(Et$_2$DTC)$_2$ does not appear to affect how the ligand ultimately binds to the surface.

Similar results are observed for exchanges performed with Cd(Et$_2$DTC)$_2$ and Zn(MePhDTC)$_2$, summarized in Table 5.2. Since the L-Z_1-Z_2 exchange conducted with Cd(MePhDTC)$_2$ was not reproducible, only the FT-IR spectra obtained from the neat powder and the direct exchange can be compared. The results follow the general trend for all four ligand cases: the thioureide resonance structure contributes more to the character of each of the ligands when they are bound to the surface of the CdSe QBs.

Table 5.2   Relative FT-IR peak intensities of C-N-C and C=N in the spectra of free and Bound M(DTC)$_2$s

	(C-N-C)/(C=N) Integrated Peak Area Ratio		
	Powdered, Neat	Direct Exchange[a]	L-Z_1-Z_2[a]
Zn(Et$_2$DTC)$_2$	0.55 ± 0.05	0.23 ± 0.09	0.29 ± 0.11
Zn(MePhDTC)$_2$	2.16 ± 0.08	1.29 ± 0.21	1.21 ± 0.26
Cd(Et$_2$DTC)$_2$	0.80 ± 0.03	0.55 ± 0.10	0.52 ± 0.14
Cd(MePhDTC)$_2$	1.86 ± 0.06	1.91 ± 0.18	***

[a] Average ± sample standard deviation of integrated area.

A third highlighted region is shown in Figure 5.9. In the spectra of the M(DTC)$_2$s, the peak at 1000 ± 70 cm^{-1} corresponds to the asymmetric C-S stretch. The band is sharp and intense in the spectrum of the powdered ligand form of Zn(Et$_2$DTC)$_2$ (purple), and diminished in intensity in the spectrum of the bound ligands (black and blue spectra). Some sources have stated that a sharp, symmetric peak, like that seen in the spectrum of the neat powdered Zn(Et$_2$DTC)$_2$ (purple), indicates symmetric bonding (bidentate) around the metal center of the ligand, whereas a doublet would indicate monodentate chelation.[24-25] However, Kellner et al. states that it is not possible to determine binding modes from splitting in the peak at 1000 ± 70 cm^{-1} in the solid

phase; X-ray diffraction data demonstrated that the metal centers of $M(DTC)_2$ ligands, regardless of ligand bonding type, are sites of C_1 symmetry.[26] The peak and its shoulder should be attributed to ν_{as}(C-S) modes and intramolecular ν_{as}(C-S) couplings. The diminished intensity of this peak is expected because intramolecular coupling of the surface-bound $Zn(Et_2DTC)_2$ ligands is considerably less likely.

Comparison of the C-N-C/C=N peak ratio in the spectra of the neat powders of $M(Et_2DTC)_2$ and $M(MePhDTC)_2$ ligands is useful for determining how the organic substituents of the dithiocarbamate functional group contribute to the electronic character of the ligands. The spectra of $M(Et_2DTC)_2$ ligands show greater contribution from the C=N resonance structure (lower C-N-C/C=N) ratio when compared to the spectra of $M(MePhDTC)_2$ ligands (Figure 5.8b (ii)). The diethyl groups of the $M(Et_2DTC)_2$ are *slightly* electron donating, allowing the nitrogen in those ligands to take on significant sp^2 character. The phenyl rings of the $M(MePhDTC)_2$ behave as electron withdrawing groups (EWD) thus the nitrogen in those ligands to retain comparatively more sp^3 character.

We note that, according to this analysis, a significant increase in thioureide character is observed in the FT-IR spectra of CdSe QB samples ligated with $M(Et_2DTC)_2$ and $M(MePhDTC)_2$. We postulate that the $\pi-$system delocalization throughout the dithiocarbamate functional group is more important than either the identity of the metal center or the individual organic substituents (diethyl or methylphenyl groups) of the ligands for determining the behavior observed in the FT-IR spectra. The absorption spectral data (Section 5.4.1) support this assertion: the values of Δ_{1B-1e} obtained from the fits of the direct exchange data of $M(Et_2DTC)_2$- and $M(MePhDTC)_2$-exchanged QBs are within error.

The bands associated with the M-S bonds of the M(DTC)$_2$ ligands may provide additional information regarding the nature of the ligand-nanocrystal interactions, but those bands appear in the far infrared, ~250-400 cm^{-1}.[27-28] Due to instrument limitations and significant scattering from vibrations within the crystal lattice,[29] this spectral region cannot be accessed.

5.4 Discussion

5.4.1 The Nature of M(DTC)$_2$ Binding: Changes in the FT-IR and the Importance of the Thioureide Resonance Structure

The nature of M(DTC)$_2$ surface binding is difficult to fully elucidate given the data collected within this work. Nevertheless, it is important to consider various possibilities in an effort to explain apparent differences in the time scales of ligand replacement when compared to other Z-type ligands, the trends observed in the absorption and photoluminescence spectra, and changes to the FT-IR spectra.

As discussed numerous times throughout this Dissertation, the surface of wurtzite CdSe QBs is neutral and corrugated, and defined by two, broad facets (1-120) (see Figures 1.6 and 1.7 in Chapter 1). The Cd and Se atoms in the valley positions are tetrahedrally coordinated, while the Cd and Se in the ridge positions have only three occupied coordination sites. In 2015, Zhou et al[2] proposed a binding scheme in which the metal center of M(oleate)$_2$ (M = Cd, Zn) is coordinated to two ridge-position selenium atoms, and the oleates are bridged between the metal center of the ligand and the two surface cadmiums. Theoretically, this coordination scheme yields a stoichiometry of {CdSe[M(oleate)$_2$]$_{0.26}$}, which aligns nicely with results obtained from elemental analysis data.[2, 17]

A similar coordination scheme would seem possible, and perhaps likely, for M(DTC)$_2$ on the surface of wurtzite CdSe QBs, but the spectral data for the samples with M(DTC)$_2$ ligands presented here do not follow the same displacement or shifting patterns observed in other L-to-Z

ligand studies.[1-2, 21] In contrast to all previous L-for-Z studies utilizing wurtzite CdSe QBs,[1-2, 21] we have observed that (1) the exchange of L-type primary amine ligands with Z-type $M(DTC)_2$s ligands is gradual rather than instantaneous, and it requires up to 20× the concentration of Z-type ligands utilized in other studies; and (2) the shifts of the 1_B-1_e features to lower energies observed in the absorption spectra upon ligand exchange do not significantly vary with the identity of the metal center of the $M(DTC)_2$s or the identity of the organic substituents. Consequently, we suggest that the coordination scheme of $M(DTC)_2$ ligands may be quite variable.

Changes in the FT-IR spectra demonstrate increased contributions from the thioureide resonance structure upon surface binding. A single dithiocarbamate functional group is capable of coordinating between one to four metals, as shown in Figure 5.10.[9] When the ligand settles onto the surface of a CdSe QB, more electron density is pushed towards the sulfurs of the dithiocarbamate, and the simple bidentate chelation of the metal center of the $M(DTC)_2$ ligands may not be retained. From our analyses, we gather that eight of the nine known coordination modes of $M(DTC)_2$s may exist on the surface of the QB (of those shown in Figure 5.10, only 'i' is impossible). The different coordination modes may interact with the surface of the QB with varying degrees of efficiency, but are likely close in binding energy.[9] We also consider that the coordination modes of the $M(DTC)_2$ on the surface may be dynamic,[30] especially in solution. This dynamic coordination environment may make it difficult to discern a definitive nanocrystal-ligand stoichiometry, unlike other Z-type ligand studies. Elemental analysis data is necessary to make any further determinations.

.
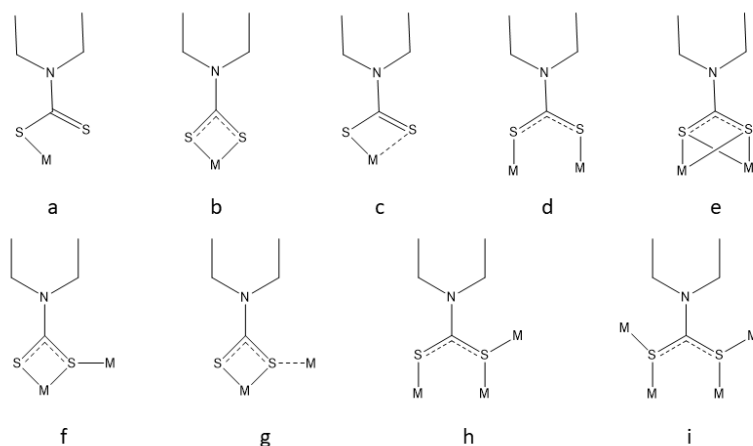
Figure 5.10   Coordination Modes of M(DTC)$_2$. M(DTC)$_2$ ligands are capable of coordinating between 1-4 metals simultaneously.[9]

5.4.2   Efficacy and Timescale of Primary Amine Displacement

We attribute the differences in the efficacy of displacement of the primary amines with Cd(oleate)$_2$ (facile, expedient) verses M(DTC)$_2$ (difficult, tedious) to several key differences between the ligands. These characteristics of M(DTC)$_2$s that sterically hinder, or physically prevent interaction with the surface include the extent of oligomerization, solubility in noncoordinating solvents, and the relative Lewis acidity of the metal centers of M(DTC)$_2$ ligands in comparison to Cd(oleate)$_2$.

Exchange with Cd(oleate)$_2$ is generally performed using a freshly prepared, anhydrous octadecene solution, in which the Cd(oleate)$_2$ is unlikely to be significantly oligomerized. M(DTC)$_2$ solutions are prepared from powders in anhydrous solvents. M(DTC)$_2$s are oligomerized in their powdered form,[9] and due to their low solubility, they are less likely to fully dissolve to monomers in solution.[31-32] We postulate that these oligomers are less likely to displace primary amines for two reasons. First, oligomerized M(DTC)$_2$s would experience significant steric hindrance when approaching the surface of the wurtzite CdSe QB, and the likelihood of a bonding event is reduced. Second, the metal center of monomeric Cd(oleate)$_2$ has

125

at least two, and as many as four, vacant bonding sites before achieving octahedral coordination. Amines in solution are known to form adducts with both $Cd(oleate)_2$ and $M(DTC)_2$ compounds.[33] In the case of ligand exchange with $Cd(oleate)_2$, the formation of these adducts encourages surface exchange by reducing the amount of free primary amine in solution. The equilibrium of the ligand-exchange reaction shifts to favor amine displacement from the surface of the QB.[1-2] The metal centers of $M(DTC)_2$ oligomers achieve tetrahedral and octahedral coordination without additional ligation from primary amines, and the equilibrium remains in favor of primary amines bound to the surface of the QBs. Thus, a driving force of the displacement reaction is reduced.

Furthermore, $Cd(oleate)_2$ is fully soluble in noncoordinating solvents such as octadecene and toluene. $M(DTC)_2$s are most soluble in coordinating solvents such as DMSO and DMF. While dissolution in a coordinating solvent may reduce the degree of oligomerization, the solvent then competes for coordination sites and reduces the amount of amine-$M(DTC)_2$ interaction. Finally, the metal centers of both $Cd(oleate)_2$ and $M(DTC)_2$ ligands behave as Lewis acids. The oxygen of the oleate ligand is smaller, less polarizable and more electronegative than the sulfur of the dithiocarbamate ligand. In comparison to $Cd(oleate)_2$, the extent of sharing of electron density reduces the Lewis acidity of the $M(DTC)_2$.[34] Due to the extent of oligomerization, reduced solubility in noncoordinating solvents, and the relative Lewis acidity of $M(DTC)_2$ ligands in comparison to $Cd(oleate)_2$, the direct exchange of primary amine to $M(DTC)_2$ is a significantly slower process than the exchange of primary amine to $Cd(oleate)_2$.

5.4.3   Source of the Shifting in the Absorption and PL Spectra

A major spectroscopic finding in these studies is that the 1_B-1_e and 1_A-1_e transitions in the absorption spectra shift together and maintain the same relative intensities in all four direct

M(DTC)$_2$ exchange studies (Figure 5.6 and Table 5.1). To explain this behavior and determine the source of the energetic shifting in the optical spectra, we examined the effects of preferential interaction of the ligands with the conduction and/or valence bands using the perspective of a simple quantum-mechanical Particle in a Well (PIW) model.

To employ this model, it was necessary to make certain assumptions regarding the CdSe QBs and their interactions with the ligands. As discussed in Chapter 1, {CdSe[n-alkylamine]$_{0.53}$} QBs are particle-in-a-well-like systems, described by the PIW equation:

$$E_g = E_{g,Bulk} + \Delta E_g \tag{5.1}$$

where

$$\Delta E_g = \frac{h^2}{8L^2\left(\frac{1}{m_e^*}+\frac{1}{m_h^*}\right)} - 4E_b^{Bulk} + \Delta_{cf,Bulk} \tag{5.2}$$

Equations 5.1 and 5.2 are modifications to equations 1.1 and 1.2, discussed in detail in Section 1.2.2 of this Dissertation. In the case of the CdSe[n-alkylamine]$_{0.53}$ QBs, the length of quantum confined dimension (L) is 1.8 nm.[13, 19] In order to fully describe the difference in energies between the 1$_B$-1$_e$ and 1$_A$-1$_e$ transitions, it is necessary to account for the effective masses of the electron and holes, m_e^* and m_h^*,[35] as well as the energy difference between the n$_B$ and n$_A$ states within the VB due to anisotropy within the crystalline lattice, or crystal field splitting, $\Delta_{cf,Bulk}$.[35-36] In CdSe, the effective mass of the electron is $m_e^* = 0.12 \cdot m_e$.[35] The holes formed in the 1$_B$ and 1$_A$ states are in different potentials (different bands), and have different effective masses: the $m_{h,B}^* = 0.92 \cdot m_e$, while $m_{h,A}^* = 0.45 \cdot m_e$.[35] The 1$_B$ and 1$_A$ states are separated by 26-39 meV in bulk CdSe, due to crystal field splitting ($\Delta_{cf,Bulk}$).[35-36] When eq 5.1 and eq 5.2 are used to predict the locations of the 1$_B$-1$_e$ and 1$_A$-1$_e$ transitions in CdSe{n-octylamine}$_{0.53}$ QBs, excellent fits are obtained. The experimentally determined values for the 1$_B$-1$_e$ and 1$_A$-1$_e$ transitions are 2.762 eV

and 2.931 eV, respectively; the calculated values are 2.786 eV and 2.942 eV, respectively. The agreement of the experimental and calculated values lends validity to the use of the PIW model.

The qualitative results of our PIW model analysis are shown in Figure 5.11, which is a graphical explanation of the effects of allowing the potential within the valence and conduction bands to vary independently from one another. Each panel will be discussed in detail in the following paragraphs. Figure 5.11a portrays the defined, PIW system observed in the as-synthesized {CdSe[n-octylamine]$_{0.53}$} QBs. In this model, we assume that the 1_A and 1_B hole states do not mix, but do share the same length of the confined dimension. As the length of the confined dimension increases, the confinement energies associated with the electron and hole states decrease (Appendix C, Section C.4, Figure C.5). By exchanging the surface ligands, the confining potential experienced by charge carriers within the system is relaxed, and the absorbance and PL spectra shift to lower energies. This model is overly simplistic; however, it still allows for the examination of the effects of preferential interaction of the ligands with the conduction and/or valence bands. We modify the CB or VB potential by adjusting the effective thickness or "length" parameter (L_{eff}) of the quantum-confinement dimension, assuming that the 1_B and 1_A feature share the same L_{eff}. In reality, it is likely that the shape and length of the confinement potentials change.
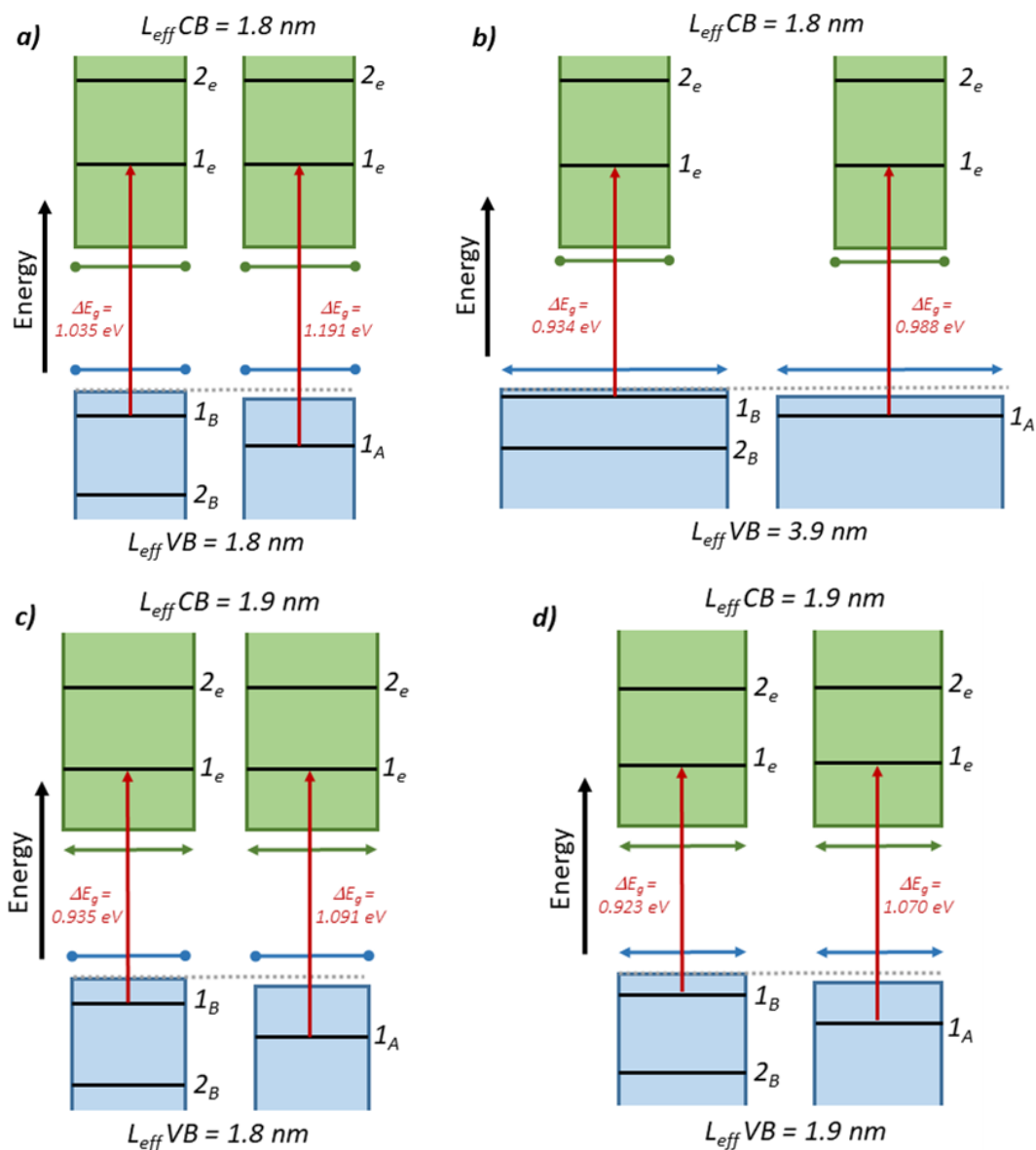
Figure 5.11   Perturbation of the bands with the conduction bands (CB) and valence bands (VB) shown in green and blue, respectively. The n_B and n_A levels are shown in separate potentials, energetically separated by 26-39 meV.[35-36] a) Transitions observed in {CdSe(n-octylamine)$_{0.53}$}; b) Scenario I: transitions shifting due to modification of valence band potential only; c) Scenario II: conduction band potential only; and d) Scenario III: transitions shifting as a result of conduction and valence band potential varying together.

Some assumptions regarding the ligands were also necessary. Using the crystal structure of the analogous structure Cd(PTC)$_2$[10] and tables of covalent bond radii,[37] we estimated the length of the ligands from the metal center (the bonding site of a Z-type ligand) to the furthest

129

atom in the compound. Cd(MePTC)$_2$ is the largest and most conjugated structure utilized in this study. As shown in Figure 5.12, the length of the ligand is approximately 0.9 nm from the metal center to the carbon in the *para*-position of the phenyl ring. Adding a full monolayer of Cd(MePTC)$_2$ to each side of the surface of the CdSe QB would result in an increase of 1.8 nm in the effective length (L_{eff}) of the confined dimension of the QB, if the charge carriers could completely delocalize into the ligand layer. This would result in a maximum value of L_{eff} = 3.6 nm. Complete delocalization into the ligand layer is an unlikely condition, and we expect an L_{eff} that results from the addition of a single ligand layer to fall well below 3.6 nm.

0.9 nm
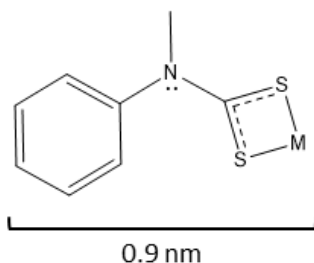
Figure 5.12   Approximate distance from the metal center (Z-type ligand bonding site) of Cd(MePTC)$_2$ to the *para* position carbon of the phenyl ring.

An energetic shift of the 1$_B$-1$_e$ feature of 100 ± 10 meV to lower energies was observed in the spectra obtained from the ligand exchange experiments (Table 5.1). In the ligand exchange experiments that utilized Zn(DTC)$_2$, the 1$_A$-1$_e$ feature also shifted by 100 ± 10 meV. In the ligand exchange experiments that utilized Cd(DTC)$_2$, the 1$_A$-1$_e$ feature shifted by 120 ± 10 meV. We now consider three explanations of the source of the shifting: 1) perturbation of the confinement potential in the valence band only via preferential interaction of the ligands with the valence band states (Figure 5.11b); 2) perturbation of the confinement potential in the conduction band only via preferential interaction of the ligands with the conduction band states (Figure 5.11c);

and 3) equal perturbation of the confinement potentials in the conduction and valence bands via interaction of the ligands with both band states (Figure 5.11d).

First, we consider preferential perturbation of the valence band potential (Figure 5.11b). In Scenario I, the confinement potential in the conduction band is held constant, and the potential of the valence band is perturbed by increasing L_{eff}. The 1_e state does not shift, while the 1_B and 1_A hole states shift to higher energies relative to their original energetic positions, i.e., there is less quantum confinement of the holes. This would result in the optically observed transitions shifting to lower energies. There are two strong arguments against this scenario. According to PIW calculations (Appendix C, Section C.2, Figure C.6), the hole in the 1_B state experiences 128 meV of confinement energy when L_{eff}=1.8 nm, which corresponds to the length of the quantum-confined dimension of the {CdSe[n-alkylamine]$_{0.53}$} QBs.[13, 19] In order to observe a shift to lower energy of 100 meV, the L_{eff} of the valence band *alone* would have to be 3.9 nm. This is not attainable via the addition of a single layer M(DTC)$_2$ ligands to the surface of the QBs, as it far exceeds the maximum attainable value of L_{eff} = 3.6 nm. Secondly, the holes formed in the 1_B and 1_A states are in different potentials (different bands) and have different effective masses. The 1_B-1_e and 1_A-1_e features are separated by approximately 130 meV in the {CdSe[n-octylamine]$_{0.53}$} QBs. Due to its lighter mass, the hole in the 1_A state is more confined than the hole in the 1_B state ($E_{c,1A}$ = 258 meV compared to $E_{c,1B}$ = 128 meV, Figure C.7 in Appendix C). If the shifting were due entirely to perturbation of the valence band, we would anticipate that the 1_A-1_e feature would energetically shift *more* than the 1_B-1_e feature. The two features would grow increasingly closer in energy, until the separation between the two peaks was ~54 meV (Figure C.7 in Appendix C). This is not observed in any of the {CdSe[M(DTC)$_2$]$_x$} QBs, therefore we reject Scenario I.

Next we consider preferential perturbation of the PIW potential in the conduction band (Figure 5.11c). In Scenario II, the confinement potentials in the 1_A and 1_B valence band states are held constant while the L_{eff} of the conduction band is increased (Appendix C, Section C.4, Figure C.7). To achieve a shift of 100 meV to lower energy, the L_{eff} of the conduction band only needs to reach 1.9 nm (an increase of 1 Å), an achievable increase with the addition of a single ligand layer. In this scenario, the 1_B-1_e and 1_A-1_e transitions would shift to lower energy by equal amounts. The total observed shift in the $\{CdSe[Zn(DTC)_2]_x\}$ QB experiments is 100 ± 10 meV for both the 1_B-1_e and 1_A-1_e transitions. We suggest that $\{CdSe[Zn(DTC)_2]_x\}$ QBs primarily experience preferential perturbation of the conduction band potential.

In the Scenario III, shown in Figure 5.11d, the valence and conduction bands are perturbed together (L_{eff} increased equally). In this case, the 1_B-1_e transition shifts 107 meV to lower energies with an increase in L_{eff} to 1.9 nm, a reasonable increase in L_{eff} for the addition of a single layer of $M(DTC)_2$ ligands (Appendix C, Section C.4, Figure C.8). The calculations indicate that the 1_A-1_e transition would shift approximately 126 meV to lower energy, approximately 19 meV more than the 1_B-1_e transition (Figure 5.11d), and the features would appear slightly closer together in the absorption spectrum of $\{CdSe[M(DTC)]_x\}$ QBs. This behavior is observed in the $Cd(DTC)_2$ ligated belts. We suggest that in the case of $Zn(DTC)_2$ ligation, only the confinement potential in the conduction band is perturbed. In the case of $Cd(DTC)_2$ ligation, the confinement potential in the conduction band and valence band are perturbed together.

The magnitude of the energetic shifts of the 1_B-1_e transition observed in the absorption spectra recorded for the samples of the $Zn(DTC)_2$ and $Cd(DTC)_2$ exchange reactions are within error of each other. This is in contrast to other reported L-for-Z exchanges, in which the

difference in energy between the 1_B-1_e transition of Zn- and Cd-analogue ligands ranges from 55-210 meV.[1-2] Energetically, the frontier orbitals of the metal centers of $Zn(DTC)_2$ and $Cd(DTC)_2$ ligands are likely far apart. The electron-accepting orbitals of the metal centers of the $Zn(DTC)_2$ and $Cd(DTC)_2$ ligands are likely similar in size and energy to 4s and 5s atomic orbitals, respectively. The difference in energy between 4s and 5s atomic orbitals is likely reflected in the energies of the frontier orbitals of $Zn(DTC)_2$ and $Cd(DTC)_2$ ligands. It would be unlikely for two orbitals with differing energies to produce similar changes in the absorption spectra of $\{CdSe[Zn(DTC)_2]_x\}$ and $\{CdSe[Zn(DTC)_2]_x\}$ QBs. The frontier orbitals of the sulfur atoms of $Zn(DTC)_2$s and $Cd(DTC)_2$s may be significantly closer in energy, similar in size and energy to 3p atomic orbitals, and thus interact with the electronic states of the CdSe QBs in a similar fashion. If the $Zn(DTC)_2$ and $Cd(DTC)_2$ ligands modify the potentials of the conduction band and valence band of the CdSe QBs in a comparable way, then we would expect to observes similar energetic shifts in the absorption spectra of $\{CdSe[Zn(DTC)_2]_x\}$ and $\{CdSe[Zn(DTC)_2]_x\}$ QBs. This aligns with our experimental observations. From this analysis, we find additional support for the assertion that the interaction of sulfur atoms of the dithiocarbamate with the surface of the CdSe QB may contribute more to the observed behaviors than the interaction of the metal center (cadmium or zinc) with the surface of the CdSe QB.

5.5   Conclusions

We have investigated the exchange of primary amines on the surface of wurtzite CdSe QBs with four $M(DTC)_2$s. This study was conducted in order to compare the effects of the organic substituents of the dithiocarbamate functional group and metal centers of the dithiocarbamate complex on the energies of the features in the absorption spectra of wurtzite CdSe QBs. By synthesizing DTCs from a secondary amine, we show these ligands are stable for

the time scale of the experiments conducted in this paper. We have also demonstrated the reversibility of the exchange. Our results indicate that neither the identity of the metal center nor the identity of the organic substituents are the determining factor in the magnitude of the bathochromic shifting of features in the absorption or PL spectra; rather, π system delocalization in the dithiocarbamate group defines the extent of the energetic changes.

Due to differences in the rate of L-type ligand displacement, energetic shifting in the absorbance and PL spectra, retention of PL intensities, and changes observed in the FT-IR upon binding, we postulate that the primary coordination interaction is not between the metal center of the $M(DTC)_2$ and the surface selenium atoms, but rather between the sulfur of the DTC functional group and the surface cadmiums.

Remaining experiments to conclude this study include quantitative elemental analysis of $M(DTC)_2$ exchanged QBs, computational modeling of the HOMO/LUMO gap of the frontier orbitals of $M(DTC)_2$ ligands and computational modeling of the lowest energy states in the valence band and conduction band. These experiments are important to assessing true structure-function relationships between the nanocrystal and the ligands employed for charge separation.

5.6   References

1.   Yao, Y.; Zhou, Y.; Sanderson, W. M.; Loomis, R. A.; Buhro, W. E., Metal-Halide-Ligated Cadmium Selenide Quantum Belts by Facile Surface Exchange. *Chem. Mater.* **2018,** *30* (8), 2848-2857.

2.   Zhou, Y.; Wang, F.; Buhro, W. E., Large Exciton Energy Shifts by Reversible Surface Exchange in 2D II–VI Nanocrystals. *J. Am. Chem. Soc.* **2015,** *137* (48), 15198-15208.

3.   Frederick, M. T.; Amin, V. A.; Cass, L. C.; Weiss, E. A., A Molecule to Detect and Perturb the Confinement of Charge Carriers in Quantum Dots. *Nano Lett.* **2011,** *11* (12), 5455-5460.

4.   Frederick, M. T.; Amin, V. A.; Weiss, E. A., Optical Properties of Strongly Coupled Quantum Dot–Ligand Systems. *J. Phys. Chem. Lett.* **2013,** *4* (4), 634-640.

5.   Frederick, M. T.; Weiss, E. A., Relaxation of Exciton Confinement in CdSe Quantum Dots by Modification with a Conjugated Dithiocarbamate Ligand. *ACS Nano* **2010,** *4* (6), 3195-3200.

6.   Buckley, J. J.; Couderc, E.; Greaney, M. J.; Munteanu, J.; Riche, C. T.; Bradforth, S. E.; Brutchey, R. L., Chalcogenol Ligand Toolbox for CdSe Nanocrystals and Their Influence on Exciton Relaxation Pathways. *ACS Nano* **2014,** *8* (3), 2512-2521.

7.   Harris, R. D.; Amin, V. A.; Lau, B.; Weiss, E. A., Role of Interligand Coupling in Determining the Interfacial Electronic Structure of Colloidal CdS Quantum Dots. *ACS Nano* **2016,** *10* (1), 1395-1403.

8.   Grenland, J. J.; Lin, C.; Gong, K.; Kelley, D. F.; Kelley, A. M., Resonance Raman Investigation of the Interaction between Aromatic Dithiocarbamate Ligands and CdSe Quantum Dots. *J. Phys. Chem. C* **2017,** *121* (12), 7056-7061.

9.   Hogarth, G., Transition Metal Dithiocarbamates: 1978–2003. In *Progress in Inorganic Chemistry*, Karlin, K., Ed. Vol. 53, pp 71-561.

10.   Morrison, C. E.; Wang, F.; Rath, N. P.; Wieliczka, B. M.; Loomis, R. A.; Buhro, W. E., Cadmium *Bis*(phenyldithiocarbamate) as a Nanocrystal Shell-Growth Precursor. *Inorg. Chem.* **2017,** *56* (21), 12920-12929.

11.   Knowles, K. E.; Frederick, M. T.; Tice, D. B.; Morris-Cohen, A. J.; Weiss, E. A., Colloidal Quantum Dots: Think Outside the (Particle-in-a-)Box. *J. Phys. Chem. Lett.* **2012,** *3* (1), 18-26.

12.   Wessels, J. M.; Nothofer, H.-G.; Ford, W. E.; von Wrochem, F.; Scholz, F.; Vossmeyer, T.; Schroedter, A.; Weller, H.; Yasuda, A., Optical and Electrical Properties of Three-Dimensional Interlinked Gold Nanoparticle Assemblies. *J. Am. Chem. Soc.* **2004,** *126* (10), 3349-3356.

13.   Liu, Y.-H.; Wayman, V. L.; Gibbons, P. C.; Loomis, R. A.; Buhro, W. E., Origin of High Photoluminescence Efficiencies in CdSe Quantum Belts. *Nano Lett.* **2010,** *10* (1), 352-357.

14.   Onwudiwe, D. C.; Arfin, T.; Strydom, C. A.; Kriek, R. J., Synthesis, Spectroscopic Characterization and Behavior of AC Impedance Spectroscopy of Cd(II) *Bis*(*n*-Para-Methylphenyl Dithiocarbamate). *Electrochim. Acta* **2013,** *104*, 19-25.

15.   Ketchemen, K. I. Y.; Mlowe, S.; Nyamen, L. D.; Ndifon, P. T.; Revaprasadu, N.; O'Brien, P., CdS Thin Films Deposition by AACVD: Effect of Precursor Type, Decomposition Temperature and Solvent. *J. Mater. Sci. - Mater. El.* **2018,** *29* (17), 14462-14470.

16.   Onwudiwe, D. C. A., P.A, Synthesis, Characterization and Thermal Studies of Zn(II), Cd(II) and Hg(II) Complexes of *N*-Methyl-*N*-Phenyldithiocarbamate: The Single Crystal Structure of [(C$_6$H$_5$)(CH$_3$)NCS$_2$]4Hg$_2$. *Int. J. Mol. Sci.* **2011,** *12*, 1964-1978.

17. Morrison, C.; Sun, H.; Yao, Y.; Loomis, R. A.; Buhro, W. E., Methods for the ICP-OES Analysis of Semiconductor Materials. *Chem. Mater.* **2020,** *32* (5), 1760-1768.

18. Zou, H.; Dong, C.; Li, S.; Im, C.; Jin, M.; Yao, S.; Cui, T.; Tian, W.; Liu, Y.; Zhang, H., Effect of Surface Trap States on Photocatalytic Activity of Semiconductor Quantum Dots. *J. Phys. Chem. C* **2018,** *122* (17), 9312-9319.

19. Wang, F.; Wang, Y.; Liu, Y.-H.; Morrison, P. J.; Loomis, R. A.; Buhro, W. E., Two-Dimensional Semiconductor Nanocrystals: Properties, Templated Formation, and Magic-Size Nanocluster Intermediates. *Acc. Chem. Res.* **2015,** *48* (1), 13-21.

20. Smith, A. M.; Nie, S., Semiconductor Nanocrystals: Structure, Properties, and Band Gap Engineering. *Acc. Chem. Res.* **2010,** *43* (2), 190-200.

21. Yao, Y.; DeKoster, G. T.; Buhro, W. E., Interchange of L-, Z-, and Bound-Ion-Pair X-Type Ligation on Cadmium Selenide Quantum Belts. *Chem. Mater.* **2019,** *31* (11), 4299-4312.

22. Costa Jr, A. C.; Ondar, G. F.; Versiane, O.; Ramos, J. M.; Santos, T. G.; Martin, A. A.; Raniero, L.; Bussi, G. G. A.; Téllez Soto, C. A., DFT: B3LYP/6-311G (d, p) Vibrational Analysis of *Bis*(Diethyldithiocarbamate)Zinc (II) and Natural Bond Orbitals. *Spectrochim. Acta A* **2013,** *105*, 251-258.

23. Zeleňák, V.; Vargová, Z.; Györyová, K., Correlation of Infrared Spectra of Zinc(II) Carboxylates with Their Structures. *Spectrochim. Acta A* **2007,** *66* (2), 262-272.

24. Bonati, F.; Ugo, R., Organotin(IV) *N,N*-Disubstituted Dithiocarbamates. *J. Organomet. Chem.* **1967,** *10* (2), 257-268.

25. Onwudiwe, D. C.; Ajibade, P. A., Synthesis and Characterization of Metal Complexes of *N*-Alkyl-*N*-Phenyl Dithiocarbamates. *Polyhedron* **2010,** *29* (5), 1431-1436.

26.   Kellner, R.; St. Nikolov, G.; Trendafilova, N., Detecting the Bonding Type of Dithiocarbamate Ligands in Their Complexes as Inferred from the Asymmetric CS Mode. *Inorg. Chim. Acta* **1984,** *84* (2), 233-239.

27.   Kellner, R.; St. Nikolov, G., Far IR Spectra of Dithiocarbamate Complexes Correlations with Structure Parameters. *J. Inorg. Nucl. Chem.* **1981,** *43* (6), 1183-1188.

28.   Mikosch, H.; Bauer, G.; Kellner, R.; Trendafilova, N. S.; St. Nikolov, G., Structure Sensitive Normal Coordinate Analysis of Metal-Diethyldithiocarbamate - Complexes. *J. Mol. Struct.* **1986,** *142*, 473-476.

29.   Vasiliev, R. B.; Vinogradov, V. S.; Dorofeev, S. G.; Kozyrev, S. P.; Kucherenko, I. V.; Novikova, N. N., IR-active Vibrational Modes of CdTe and CdSe Colloidal Quantum Dots and CdTe/CdSe Core/Shell Nanoparticles and Coupling Effects. *Phys. Solid State* **2007,** *49* (3), 547-551.

30.   McBride, J. R.; Pennycook, T. J.; Pennycook, S. J.; Rosenthal, S. J., The Possibility and Implications of Dynamic Nanoparticle Surfaces. *ACS Nano* **2013,** *7* (10), 8358-8365.

31.   Malik, M. A.; Saeed, T.; O'Brien, P., The Synthesis and Characterization of Cadmium and Zinc Complexes with Dithiocarbamate Derivatives of Diamines. *Polyhedron* **1993,** *12* (12), 1533-1538.

32.   Manar, K. K.; Yadav, M. K.; Anamika; Drew, M. G. B.; Singh, N., Influence of Functionalities Over Polymer, Trimer, Dimer Formation and Optical Properties of Cadmium Dithiocarbamates. *Polyhedron* **2016,** *117*, 592-599.

33.   Onwudiwe, D. C.; Strydom, C. A., The Bipyridine Adducts of *N*-Phenyldithiocarbamato Complexes of Zn(II) and Cd(II); Synthesis, Spectral, Thermal Decomposition Studies and Use as Precursors for ZnS and CdS Nanoparticles. *Spectrochim. Acta A* **2015,** *135*, 1080-1089.

34.   Ray, K.; Petrenko, T.; Wieghardt, K.; Neese, F., Joint SPectroscopic and Theoretical Investigations of Transition Metal Complexes Involving Non-innocent Ligands. *Dalton Trans.* **2007,** (16), 1552-1566.

35.   *Semiconductors - Basic Data*. 2nd revised edition ed.; Springer: Berlin, 1996.

36.   Lew Yan Voon, L. C.; Willatzen, M.; Cardona, M.; Christensen, N. E., Terms Linear in k in the Band Structure of Wurtzite-Type Semiconductors. *Phys. Rev. B* **1996,** *53* (16), 10703-10714.

37.   Cordero, B.; Gómez, V.; Platero-Prats, A. E.; Revés, M.; Echeverría, J.; Cremades, E.; Barragán, F.; Alvarez, S., Covalent radii revisited. *Dalton Trans.* **2008,** (21), 2832-2838.

Chapter 6: Conclusions and
Future Directions

This work discussed in this dissertation has demonstrated the following: 1) ICP-OES can be used as a high-throughput, accurate way to determine semiconductor nanocrystal (SCNC) stoichiometry and, in conjunction with other methods, to determine extent of ligand exchange on the surface of SCNCs; 2) L-for-Z ligand exchange technology can be used to install degrading ligands and grow shells on the surface of CdSe quantum belts (QBs); and 3) metal dithiocarbamate ($M(DTC)_2$) ligands synthesized from secondary amines can installed in an 'L-for-Z'-like fashion, but $M(DTC)_2$s do not follow the trends of other Z-type ligands.

Accurate determination of SCNC stoichiometry is critical for determining structure – function relationships. Because the work discussed in Chapter 3 details an experimental method, the future applications are broad. The protocols can be applied to the extensive library of II-VI semiconductor materials described in the literature. The two-step digestion technique described in Chapter 3 could be tested and qualified for the analysis of materials outside the realm of II-VI semiconductors as well. Many of the techniques described in this chapter could be adapted for ICP-MS (inductively coupled plasma mass spectrometry).

Chapter 4 discussed the utility of $Cd(PTC)_2$ as low-temperature, single-source CdS shell growth precursor for CdSe QBs. Modification of these experiments could entail development of other $M(PTC)_2$ (such as $Zn(PTC)_2$) as a single-source shell-growth precursors. This shell-growth technique could be modified and generalized to other nanostructures (CdTe QBs, CdSe QDs).

Chapter 5 demonstrated that $M(DTC)_2$ ligands synthesized from secondary amines can installed in an 'L-for-Z'-like fashion, but $M(DTC)_2$s do not follow the trends of other Z-type

ligands. Elemental analysis data, both from combustion elemental analysis and ICP-OES, would help make further determinations regarding how the $M(DTC)_2$s are binding to the surface. Additional routes for installing $M(DTC)_2$ ligands could be investigated, including using A^+X^- ligands as an intermediate. Investigations could be conducted to identify the isotherm model that best describes the adsorption of $M(DTC)_2$s to the surface of CdSe QB. The use of advanced spectroscopies to determine how the dynamics change would yield insight into the nature of the ligand-nanocrystal electronic interaction.

Appendix A:

Associated Content for Chapter 3

Methods for the ICP-OES Analysis of Semiconductor Materials

Figure A1. Polypropylene and high-density polyethylene centrifuge tubes (15 ml) appropriate for the digestion steps in the procedure described in the main text.

Table A1. Instrumentation Details**.** PerkinElmer ICP-OES PE Optima 7300DV with Syngistix for ICP, Version 2.0.0.22336 software.

Gas Flow	
Plasma	15 L/min
Auxiliary	0.2 L/min
Nebulizer	0.70 L/min
RF Power	1300 Watts
Pump Flow Rate	1.5 mL/min

Spectrometer	
Resolution	High (0.0035 nm)
Read Time (sec)	Min 5; Max 20
Delay Time	60
Replicates	3
Calibration	Hg Realignment at 253 nm

Plasma	
Conditions	Same for all elements
Plasma View	Axial
Source Equilibration Delay	15 sec

Peristaltic Pump	
Sample Flow Rate	1.50 mL/min
Flush Time	60 sec

Note A1. This note regards the concentration units employed in ICP-OES analyses. ICP-OES standards are commonly produced and sold in units of mg/L or (equivalently) μg/mL. These units are often referred to as "parts per million" or "ppm" by ICP-OES practitioners, but such usage is an approximation that assumes a solution density of 1 g/mL. Certain instrumentation software packages have users select units when setting up their analyses. Units of ppm are not SI or IUPAC units and are somewhat ambiguous. In order to *accurately* present concentration data in ppm, the density of the solution must be known.[1] This adds extra steps both experimentally and when propagating the overall error in concentration. Throughout this paper, we have chosen to use unambiguous, IUPAC units of mg/L. Ultimately, the final results are given as molar ratios.

Figure A2. Example of a septum-capped polypropylene centrifuge tube under vacuum.
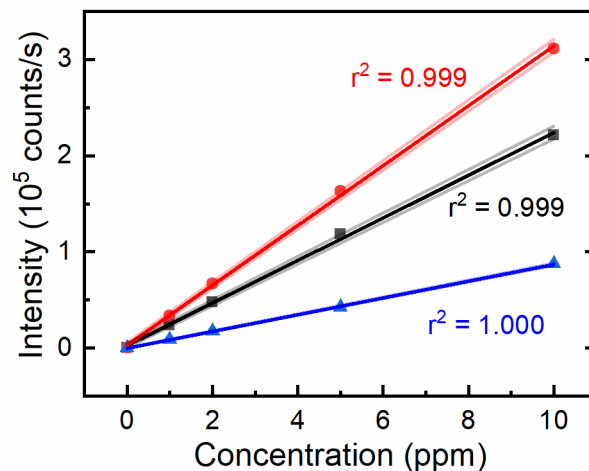
Figure A3. Linear Fit of Cd Emission Data. Emission intensity from cadmium at 214.438 nm (blue), 226.502 nm (red), and 228.802 nm (black), over a concentration range of 0-10 ppm. The solid lines are linear fits of the data points for each set. The lighter lines represent errors in the fit. Numerical values for the slope and intercept and their respective errors are given in the table below.

	Intercept Value	Intercept Standard Error	Slope Value	Slope Standard Error
Cd 228.802	2600	2300	22110	440
Cd 214.440	-140	430	8700	83
Cd 226.502	3100	2300	31080	450

Example A1. Propagation of error example.

Below is an example of the error-propagation[2-3] procedure used to determine the overall errors in molar ratio presented in the main text. For clarity, the example begins with one dilution and with data collected at a single wavelength of a single element. The steps of error propagation must be completed at each dilution, at each wavelength, and for each element.

Step 1: Propagating the error of the linear fit to find error of a given concentration in mg/L (x). (Note: additional figures are retained to avoiding rounding errors.) A detailed explanation of this equation and the values used can be found in Ref. 3.[3]

$$Uncertainty\ in\ x\ (s_x) = \frac{s_y}{|m|}\sqrt{\frac{1}{k} + \frac{1}{n} + \frac{(y - \bar{y})^2}{m^2 \sum(x_i - \bar{x})^2}}$$

Cd 228.802	Value	Error (δ)
Intensity (CPS) (y)	18172	32
Intercept (b)	2450	922
Slope (m)	8095	98
Standard deviation of y values (s_y)	1668	--
Average of y values ($\bar{y}$) collected for calibration line	53717	--
Average of x values ($\bar{x}$) collected for calibration line	6.33	--
Number of replicate measurements of unknown (k)	3	--
Number of data points for calibration line (n)	6	--

Concentration (x) = 1.94 mg/L; s_x = 0.15

Step 2: Convert mg/L to mol/L (c) and propagate the error (δc). (Note: since the final result is given as molar ratios, the conversion of g/mol to mg/mol can be neglected. The error in this step is calculated as a relative error and will propagate correctly. The conversion is shown below for clarity.) The example for Cd 228.802 is shown below. The molar mass (m) of Cd is 112.414 $\pm$ 0.004 g/mol. Repeat for all wavelengths.

$$1.94 \left(^{mg}/_L\right) \div \left[112.414 \left(^{g}/_{mol}\right) \times 1000 \left(^{mg}/_g\right)\right] = 1.73^{-5}\ M\ or\ 0.0173\ mM$$

$$\frac{\delta c}{c} = \sqrt{\left(\frac{\delta x}{x}\right)^2 + \left(\frac{\delta m}{m}\right)^2} \qquad \frac{\delta c}{0.0173} = \sqrt{\left(\frac{0.15}{1.94}\right)^2 + \left(\frac{0.004}{112.414}\right)^2}$$

$$\delta c = 0.0013\ mM$$

$$c = 0.0173 \pm 0.0013\ mM$$

Step 3: Calculate the most probable mean concentration (μ_c) of the dilution at each wavelengths of a given element and propagate error ($\delta\mu_c$).

Cd Line (nm)	Concentration (*c*) (mM)	Error (δc) (mM)
228.802	0.0173	0.0013
226.502	0.0170	0.0012
214.440	0.0169	0.0013

$$\mu_c = \frac{\sum \frac{c_i}{\delta c_i^2}}{\sum \frac{1}{\delta c_i^2}} \qquad \mu_c = \frac{\frac{0.0173}{0.0013^2} + \frac{0.0170}{0.0012^2} + \frac{0.0169}{0.0013^2}}{\frac{1}{0.0013^2} + \frac{1}{0.0012^2} + \frac{1}{0.0013^2}} = 0.0171 \text{ mM}$$

$$\delta\mu_c = \sqrt{\frac{1}{\sum 1/\delta c_i^2}} \qquad \delta\mu_c = \sqrt{\frac{1}{\frac{1}{0.0013^2} + \frac{1}{0.0012^2} + \frac{1}{0.0013^2}}} = 0.0007 \text{ mM}$$

Step 4: Calculate molar ratio (R_c) and propagate error.

Element	Most Probable Mean Concentration (μ_c) (mM)	Error ($\delta\mu_c$) (mM)
Cd	0.0171	0.0007
Se	0.0172	0.0008

$$R_c = \frac{0.0171}{0.0172} = 0.994$$

$$\frac{\delta R_c}{0.994} = \sqrt{\left(\frac{0.0007}{0.0171}\right)^2 + \left(\frac{0.0008}{0.0172}\right)^2}$$

$$\delta R_c = 0.062$$

Step A5: Calculate the molar ratio at other dilutions, find the most probable mean ratio (μ_R) and propagate error ($\delta\mu_R$).

Dilution	Ratio (R_c)	Error (δR_c)
1 (shown above)	0.994	0.062
2	1.023	0.082
3	1.003	0.027
Most Probable Mean Ratio (μ_R)	1.004	0.024

$$\mu_R = \frac{\sum \dfrac{R_{c_i}}{\delta R_{c_i}{}^2}}{\sum \dfrac{1}{\delta R_{c_i}{}^2}}$$

$$\mu_c = \frac{\dfrac{0.994}{0.062^2} + \dfrac{1.023}{0.082^2} + \dfrac{1.003}{0.027^2}}{\dfrac{1}{0.062^2} + \dfrac{1}{0.082^2} + \dfrac{1}{0.027^2}} = 1.004$$

$$\delta\mu_R = \sqrt{\frac{1}{\sum 1/\delta R_{c_i}{}^2}}$$

$$\delta\mu_c = \sqrt{\frac{1}{\dfrac{1}{0.062^2} + \dfrac{1}{0.082^2} + \dfrac{1}{0.027^2}}} = 0.024$$

Final Result: Molar Ratio of Cd/Se in {CdSe[n-octylamine]$_{0.53}$}

QBs: $\mu_R = 1.00 \pm 0.02$.
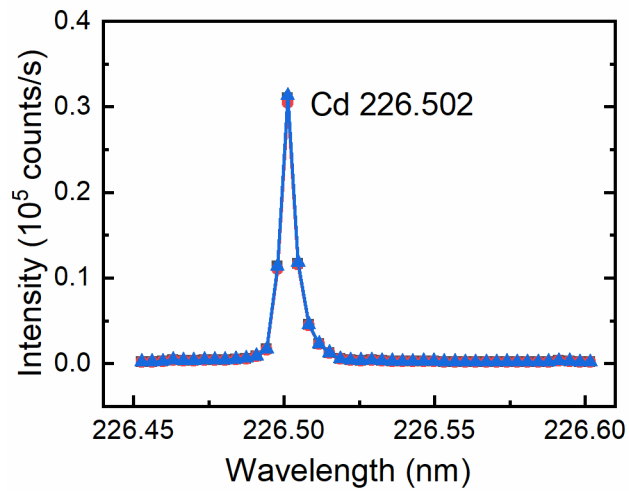
Figure A4. An example of an emission line of Cd with no spectral overlaps or interferences. The peak appears symmetrical and the background intensity is minimal with no apparent sloping.

References

1.   Gaines, P. ICP Operations Guide: Part 3, Handling, Calculations, Preparation and Storage of Standards. https://www.inorganicventures.com/icp-guide/handling-calculations-preparation-and-storage-of-standards (accessed December 31, 2019).

2.   Bevington, P. R.; Robinson, D. K., *Data Reduction and Error Analysis for the Physical Sciences, 2nd ed*. McGraw-Hill Companies, Inc.: 1992.

3.   Harris, D. C., *Quantitative Chemical Analysis*. W. H. Freeman: 2010.

Appendix B:

Associated Content for Chapter 4

Cadmium Bis(phenyldithiocarbamate) as a Nanocrystal Shell-Growth Precursor

Figure B.1 FT-IR spectrum of $Cd(PTC)_2$. Assignments were made using the literature assignments for $Zn(PTC)_2$.[1] The $\nu(C=N)$ s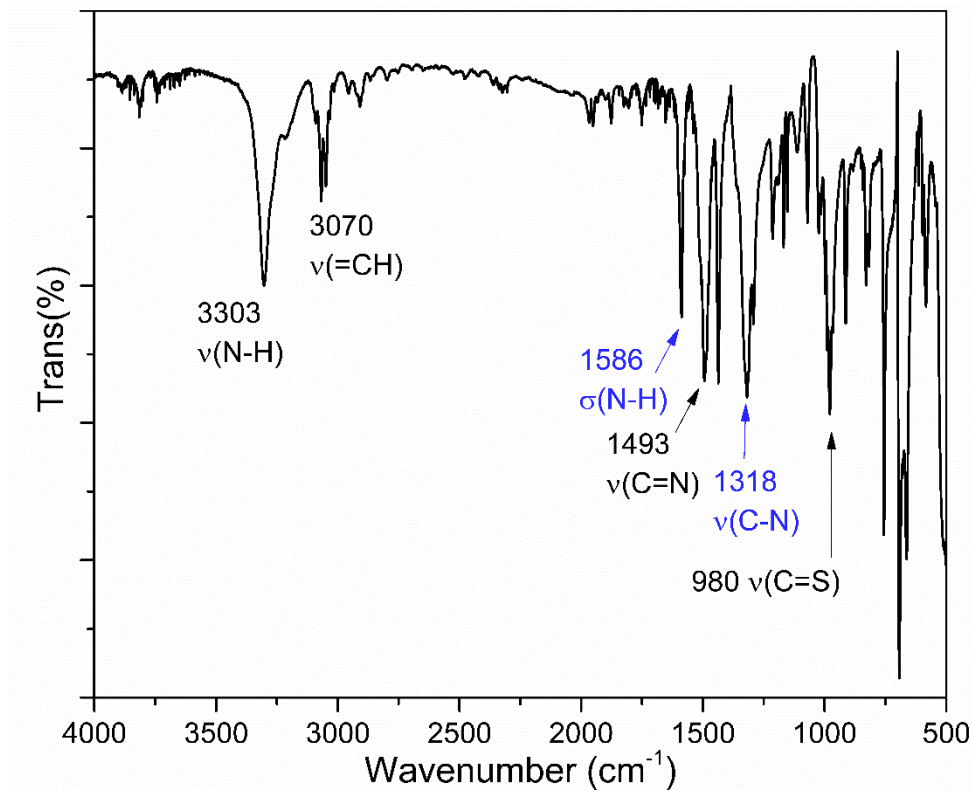tretch at 1493 cm^{-1} suggests the pseudo-sp[2] hybridization of the nitrogen in the dithiocarbamate group and significant contribution of the fully conjugated resonance structure.[1]

Table B.1 Atomic coordinates ($\times$ 10^4) and equivalent isotropic displacement parameters (Å^2 $\times$ 10^3) for Cd(PTC)$_2$. U(eq) is defined as one third of the trace of the orthogonalized U^{ij} tensor.

	x	y	z	U(eq)
Cd(1)	4726(1)	2453(1)	4664(1)	10(1)
S(1)	5053(1)	5824(1)	3986(1)	10(1)
S(2)	3327(1)	4254(1)	4304(1)	14(1)
S(3)	5094(1)	852(1)	3308(1)	11(1)
S(4)	6164(1)	483(1)	4751(1)	10(1)
N(1)	3616(1)	7477(1)	3630(1)	11(1)
N(2)	6642(1)	-756(1)	3407(1)	10(1)
C(1)	3935(1)	5954(1)	3945(1)	10(1)
C(2)	2763(1)	8078(1)	3483(1)	11(1)
C(3)	2668(1)	9932(1)	3344(1)	13(1)
C(4)	1868(1)	10645(2)	3144(1)	17(1)
C(5)	1159(1)	9512(2)	3072(1)	18(1)
C(6)	1254(1)	7669(2)	3214(1)	17(1)
C(7)	2049(1)	6937(2)	3423(1)	14(1)
C(8)	6003(1)	81(1)	3763(1)	10(1)
C(9)	6713(1)	-1140(1)	2603(1)	10(1)
C(10)	7498(1)	-744(1)	2264(1)	13(1)
C(11)	7621(1)	-1144(2)	1487(1)	17(1)
C(12)	6964(1)	-1938(2)	1053(1)	17(1)
C(13)	6187(1)	-2345(1)	1397(1)	15(1)
C(14)	6054(1)	-1956(1)	2175(1)	13(1)
O(1S)	8243(1)	8548(1)	4137(1)	17(1)
C(1S)	8376(1)	8663(2)	4958(1)	16(1)
C(2S)	8951(1)	7070(2)	5155(1)	18(1)
C(3S)	9554(1)	7056(2)	4465(1)	21(1)
C(4S)	8972(1)	7675(2)	3795(1)	16(1)

Table B.2 Anisotropic displacement parameters ($\mathring{A}^2 \times 10^3$) for Cd(PTC)$_2$. The anisotropic displacement factor exponent takes the form: $-2\pi^2\,[h^2\,\text{a*}^2 U^{11} + ... + 2\,\text{h k a* b*}\,U^{12}]$

	U^{11}	U^{22}	U^{33}	U^{23}	U^{13}	U^{12}
Cd(1)	10(1)	9(1)	12(1)	0(1)	1(1)	1(1)
S(1)	8(1)	9(1)	12(1)	0(1)	1(1)	0(1)
S(2)	9(1)	11(1)	22(1)	5(1)	2(1)	-1(1)
S(3)	9(1)	12(1)	11(1)	0(1)	0(1)	2(1)
S(4)	9(1)	10(1)	10(1)	0(1)	1(1)	0(1)
N(1)	9(1)	10(1)	14(1)	1(1)	0(1)	0(1)
N(2)	8(1)	13(1)	10(1)	-1(1)	0(1)	2(1)
C(1)	10(1)	9(1)	10(1)	-1(1)	0(1)	0(1)
C(2)	10(1)	13(1)	10(1)	0(1)	0(1)	1(1)
C(3)	12(1)	14(1)	14(1)	2(1)	1(1)	2(1)
C(4)	16(1)	19(1)	15(1)	4(1)	2(1)	6(1)
C(5)	12(1)	28(1)	15(1)	4(1)	0(1)	6(1)
C(6)	10(1)	26(1)	15(1)	-1(1)	-1(1)	-1(1)
C(7)	11(1)	16(1)	16(1)	-1(1)	-1(1)	0(1)
C(8)	9(1)	9(1)	11(1)	0(1)	2(1)	-1(1)
C(9)	11(1)	10(1)	11(1)	0(1)	2(1)	1(1)
C(10)	11(1)	14(1)	14(1)	-1(1)	3(1)	0(1)
C(11)	16(1)	18(1)	16(1)	-1(1)	6(1)	1(1)
C(12)	22(1)	17(1)	12(1)	-2(1)	3(1)	3(1)
C(13)	17(1)	14(1)	14(1)	-3(1)	-1(1)	2(1)
C(14)	12(1)	13(1)	13(1)	-2(1)	1(1)	0(1)
O(1S)	12(1)	25(1)	14(1)	-1(1)	-1(1)	7(1)
C(1S)	16(1)	19(1)	14(1)	-1(1)	0(1)	3(1)
C(2S)	15(1)	23(1)	17(1)	4(1)	1(1)	4(1)
C(3S)	13(1)	30(1)	20(1)	2(1)	1(1)	6(1)
C(4S)	13(1)	18(1)	16(1)	0(1)	2(1)	3(1)

Table B.3 Hydrogen coordinates ($\times 10^4$) and isotropic displacement parameters ($\mathring{A}^2 \times 10^3$) for Cd(PTC)$_2$

	x	y	z	U(eq)
H(1)	4017(10)	8200(20)	3520(10)	24(4)
H(2)	7092(9)	-980(20)	3664(9)	17(4)
H(3)	3153	10711	3386	16
H(4)	1806	11910	3057	20
H(5)	613	9994	2927	22
H(6)	767	6895	3168	21
H(7)	2106	5676	3523	17
H(10)	7948	-203	2562	16
H(11)	8155	-874	1253	20
H(12)	7045	-2202	520	20
H(13)	5740	-2896	1099	18
H(14)	5523	-2244	2410	15
H(1SA)	7824	8573	5232	20
H(1SB)	8659	9820	5101	20
H(2SA)	8619	5929	5188	22
H(2SB)	9271	7268	5649	22
H(3SA)	10040	7905	4546	25
H(3SB)	9783	5825	4371	25
H(4SA)	9282	8533	3457	19
H(4SB)	8784	6623	3479	19

Table B.4 Hydrogen bonds for Cd(PTC)$_2$ [Å and °].

D-H...A	d(D-H)	d(H...A)	d(D...A)	<(DHA)
N(1)-H(1)...S(3)#3	0.847(14)	2.603(14)	3.4396(9)	170.0(16)
N(2)-H(2)...O(1S)#4	0.841(13)	1.984(13)	2.8195(12)	172.1(16)
C(3)-H(3)...S(3)#3	0.95	3.02	3.8342(11)	144.0
C(7)-H(7)...S(2)	0.95	2.54	3.1760(11)	124.6
C(1S)-H(1SA)...S(2)#1	0.99	2.87	3.6577(12)	137.0

Symmetry transformations used to generate equivalent atoms:

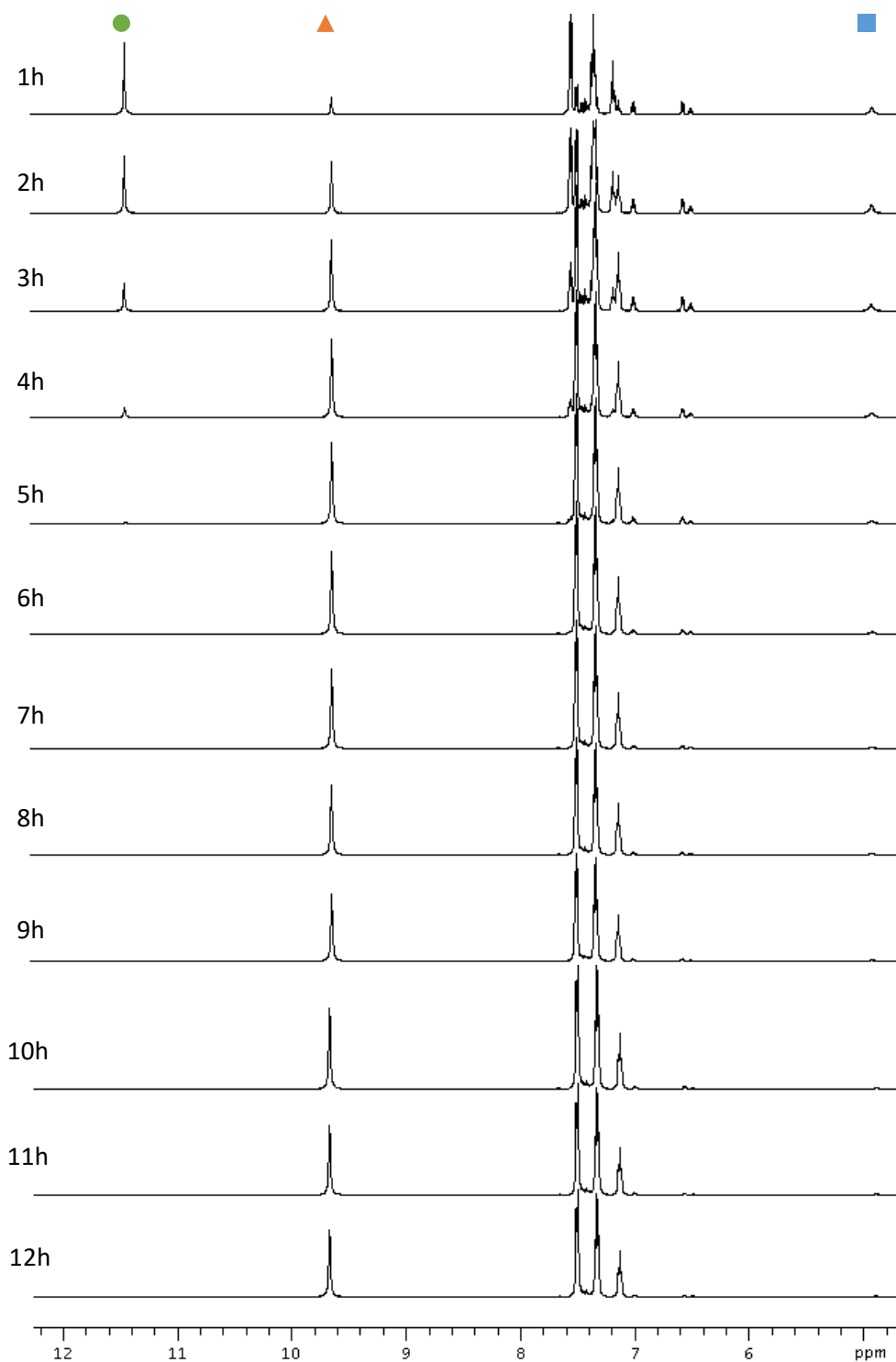#1 -x+1,-y+1,-z+1   #2 -x+1,-y,-z+1   #3 x,y+1,z

#4 x,y-1,z

Figure B.2 Conversion of Cd(PTC)$_2$ as monitored by ^{1}H NMR. The decomposition of Cd(PTC)$_2$ in DMSO was monitored at 50 °C for 12 h. The N-H of Cd(PTC)$_2$ (11.2 ppm, green circle) gradually disappeared. The N-H of the aniline intermediate (5.0 ppm, blue square) was observed at 1 h, and was nearly gone by 7 h. The N-H of 1,3-diphenylthioruea (9.8 ppm, orange triangle) appeared at 1 h, and grew in as a final product.
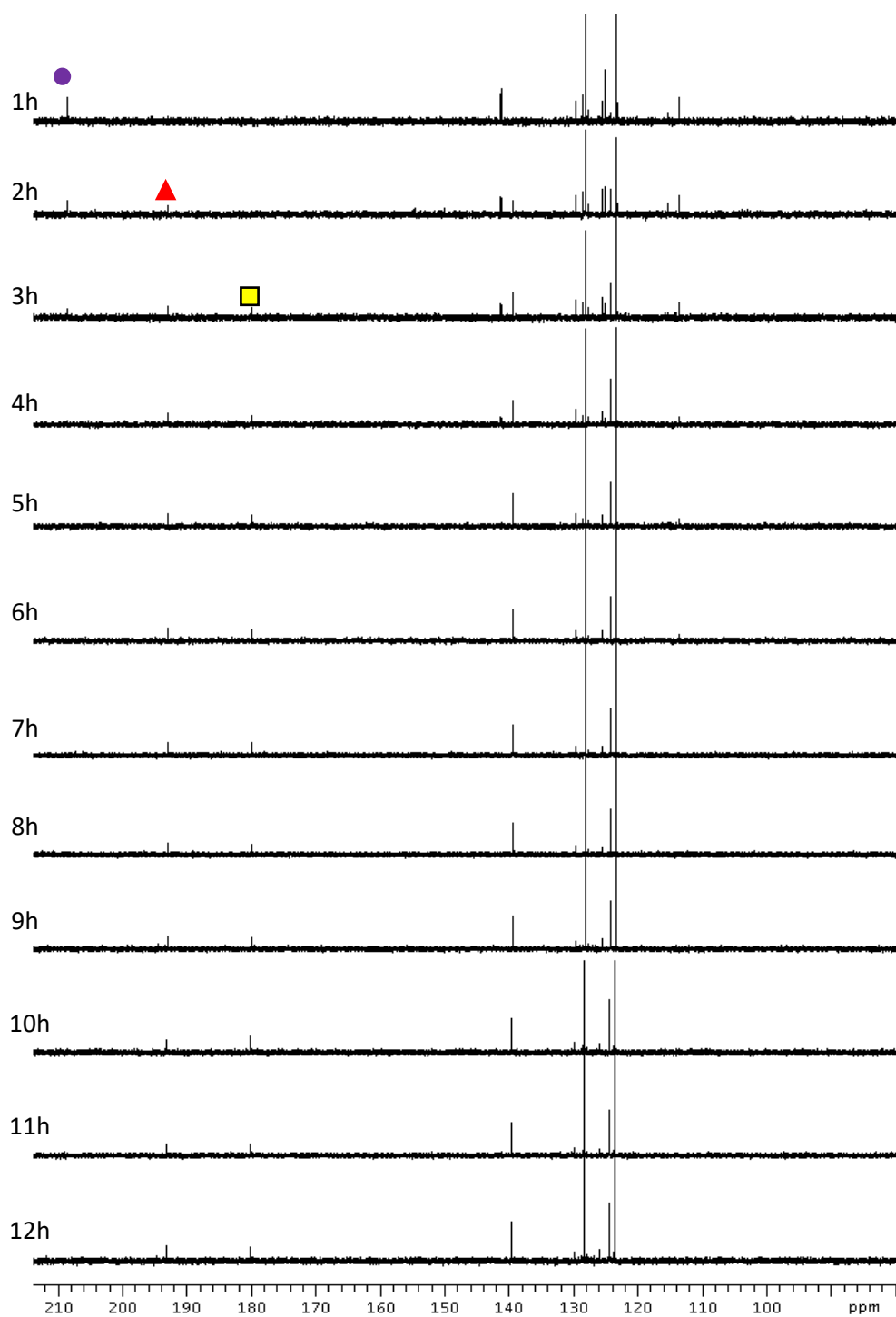
Figure B.3 Conversion of Cd(PTC)$_2$ as monitored by ^{13}C{^{1}H} NMR. The decomposition of Cd(PTC)$_2$ in DMSO was monitored at 50 °C for 12 h. The dithiocarbamate carbon of Cd(PTC)$_2$ (209 ppm, purple circle) gradually disappeared. The CS$_2$ appeared at 193 ppm (red triangle) and increased in intensity as the reaction progressed. The peak indicative of 1,3-diphenylthioruea (180 ppm, yellow square) appeared at 1 h, and grew in as a final product.
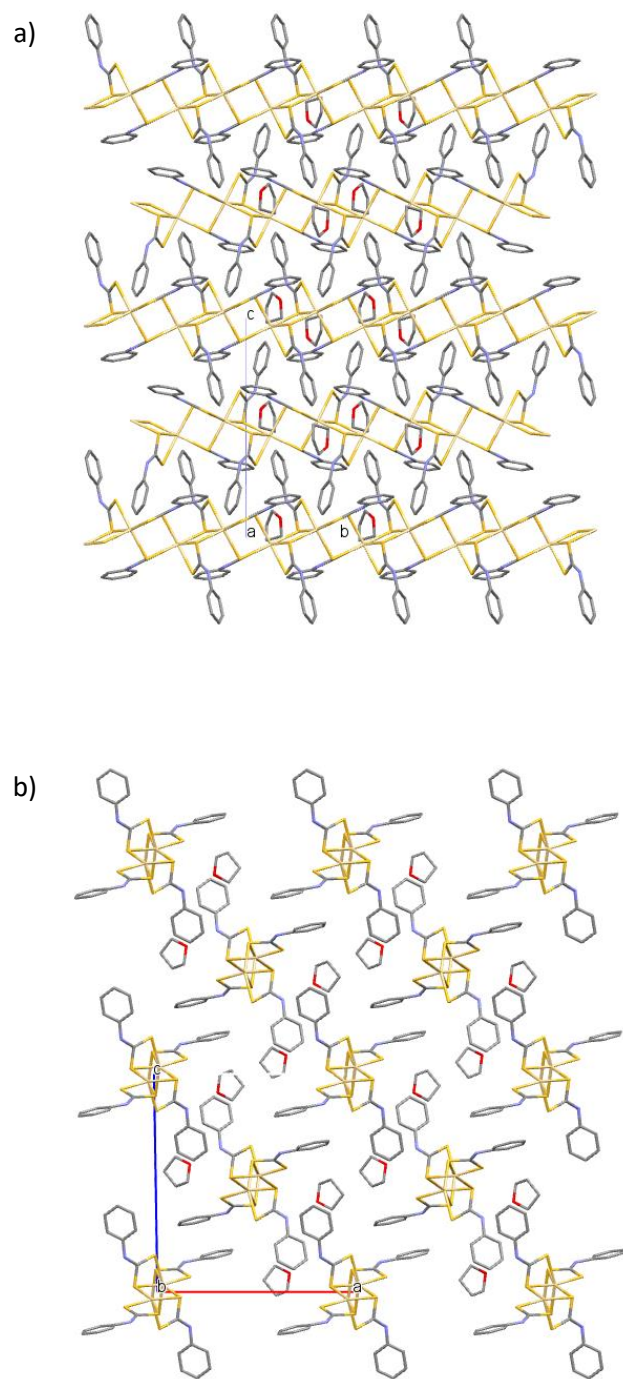
Figure B.4 Packing Diagrams of Cd(PTC)$_2$, in two orientations. Note the THF solvate molecules.
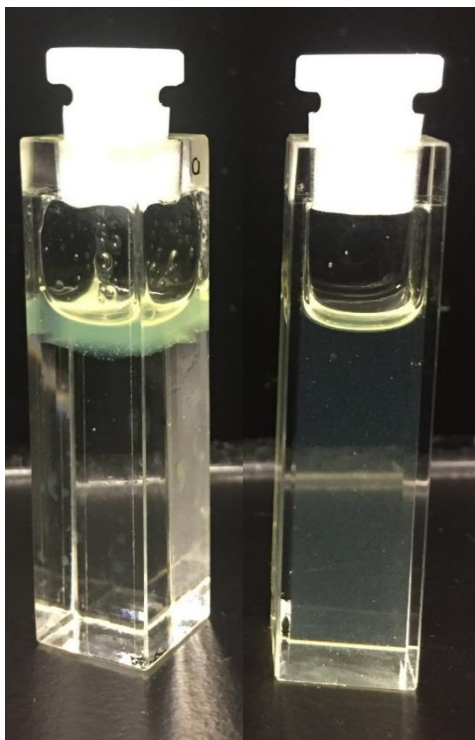
Figure B.5 Dispersibilities of as-synthesized amine-ligated (L-type) and Cd(PTC)$_2$-ligated (Z-type) CdSe QBs. The as-synthesized QBs are not dispersible in neat DMSO (left; see yellow layer separated at the top). The as-synthesized QBs readily disperse in a Cd(PTC)$_2$/DMSO solution (right), suggesting that the L-type amine ligation has been replaced by Z-type Cd(PTC)$_2$ ligation.

Table B.5 Elemental-analysis data for CdSe QBs after reaction with excess Cd(PTC)$_2$. The results for these thick-shelled QBs revealed far higher sulfur content than would have been expected if the Cd(PTC)$_2$ had remained intact as Z-type ligation.[2]

	Trial 1	*Trial 2*	*Trial 3*
%C	2.83	2.41	2.47
%H	0.61	<0.5	0.50
%N	<0.5	<0.5	<0.5
%S	21.32	-	20.01

Calculation of expected %S in CdSe[Cd(PTC)$_2$]$_{0.19}$:

191.37 g sample of CdSe

191.37 g / 191.37 g/mol = 1 mol CdSe

1 mol CdSe / 0.19 mol Cd(PTC)$_2$

0.19 mol Cd(PTC)$_2$ * 448.92 g/mol = 85.29 g Cd(PTC)$_2$

191.37 g CdSe + 85.29 g Cd(PTC)$_2$ = 276.66 g total

85.29 g Cd(PTC)$_2$ / 276.66 g (CdSe + Cd(PTC)$_2$) = 0.3083 = 30.83 % Cd(PTC)$_2$ by mass

0.3083 (% Cd(PTC)$_2$ / Sample) * 0.2858 (% S / Cd(PTC)$_2$) = **0.088 (% S / sample)**

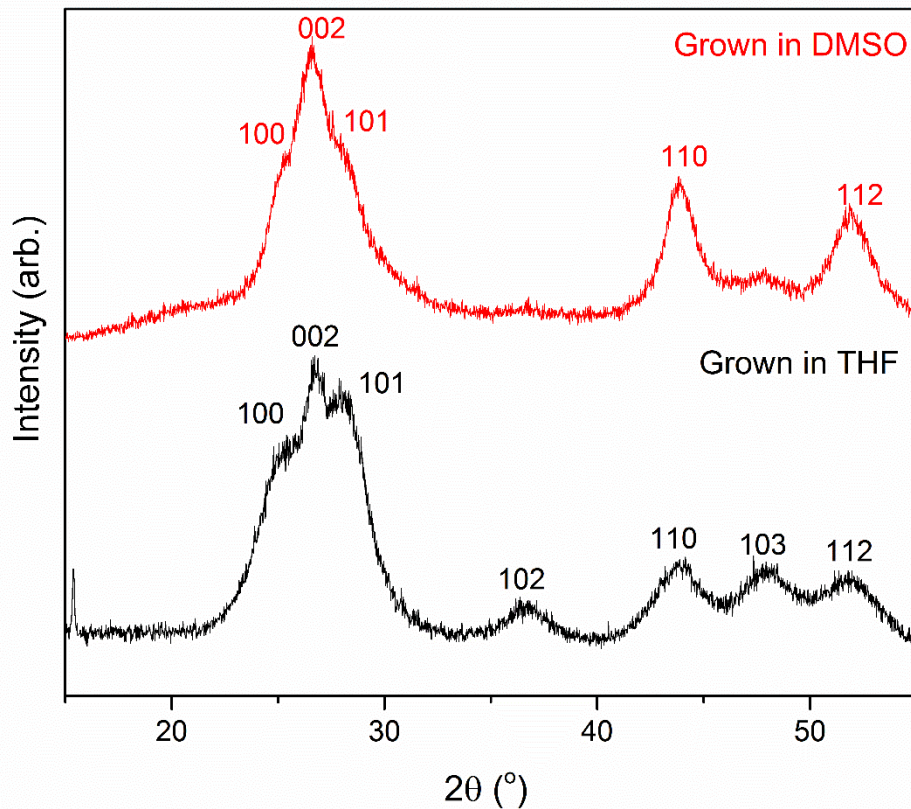**8.8 %S expected < 20.67 %S found**

Figure B.6 Powder XRD patterns of CdS formed from Cd(PTC)$_2$ decomposition (in the absence of CdSe QBs). CdS powder formation in DSMO (red) gave broader, less-resolved peaks. CdS powder formation in THF was slower and produced a well-resolved wurtzite pattern. The calculated lattice parameters, a = 4.10 Å and c = 6.83 Å, represent a -0.83%, and 1.86% deviation, respectively, from the bulk values of CdS (a = 4.13 Å and c = 6.75 Å).

Full scale counts: 2983   11085a25s-Bi(2)   Cursor: 0.019 keV
                                                                     1975 Counts

Element Line	Net Counts	Net Counts Error	Int. Cps/nA	K-Factor	Weight %	Weight % Error	Atom %	Atom % Error
S K	14119	+/- 190	---	1.030	23.99	+/- 0.32	52.53	+/- 0.71
	0	+/- 371	---	---	---	---	---	---
S L								
Cd L	26583	+/- 440	---	1.732	76.01	+/- 1.26	47.47	+/- 0.79
Cd M	0	+/- 61	---	---	---	---	---	---
Total					100.00		100.00	

Figure B.7 EDS results for the CdS powder product from thermolysis of Cd(PTC)$_2$ in THF. EDS data revealed a Cd:S ratio of nearly 1:1.
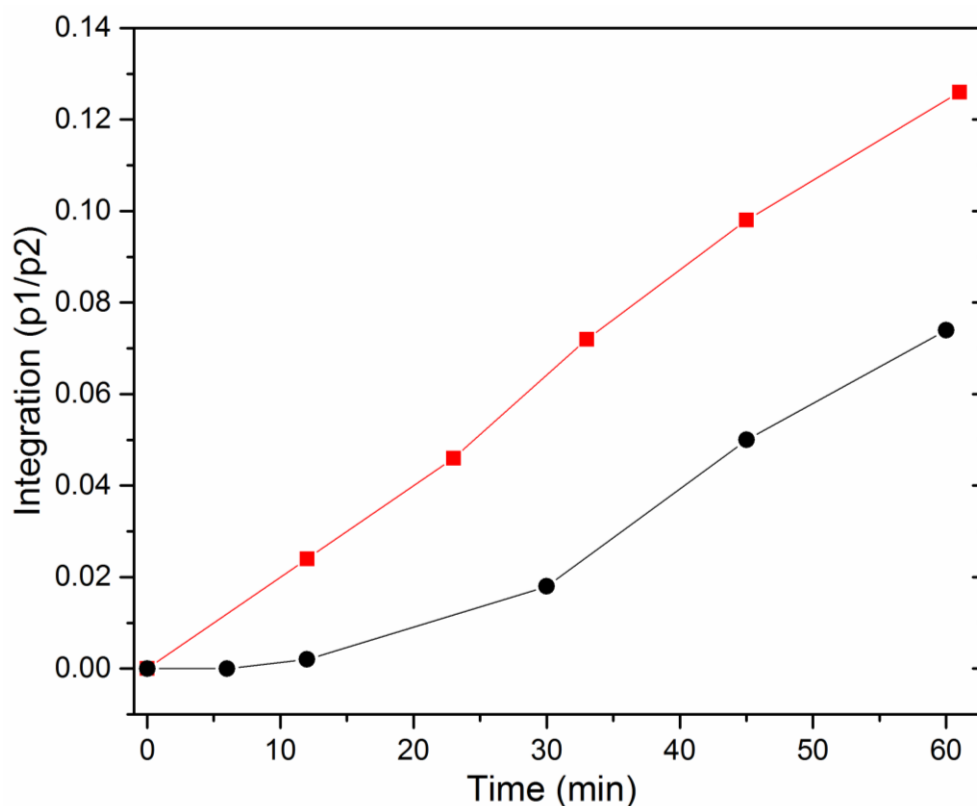
Figure B.8 Rate of conversion of Cd(PTC)$_2$ to 1,3-diphenylthiourea with (red squares) and without (black circles) added base. The rate of conversion of Cd(PTC)$_2$ to 1,3-diphenylthiourea was monitored by ^{1}H NMR. In principle, any primary amine could act as the base in this reaction, but that amine would also form a substituted thiourea product. To ensure that only a single symmetric, disubstituted thiourea was produced, aniline was chosen as the catalytic base. The black circles represent conversion of Cd(PTC)$_2$ to in DMSO at 50 °C without added base. The red squares represent the conversion of Cd(PTC)$_2$ in the presence of aniline in DSMO at 50 °C. The integrated area of the peaks corresponding to the N-H of Cd(PTC)$_2$ (*p2*) and the N-H of 1,3-diphenylthiourea (*p1*) product were compared in order to assess extent of reaction. Initially, the amine-catalyzed process was faster. However, after the reaction was initiated without added base, the rate of conversion roughly matched that observed in the process with added aniline.
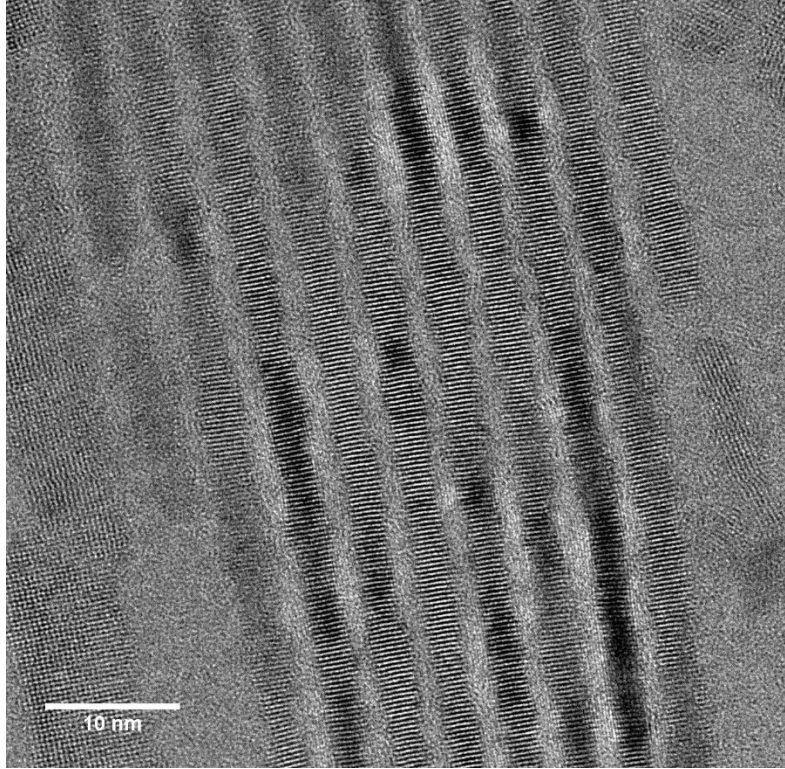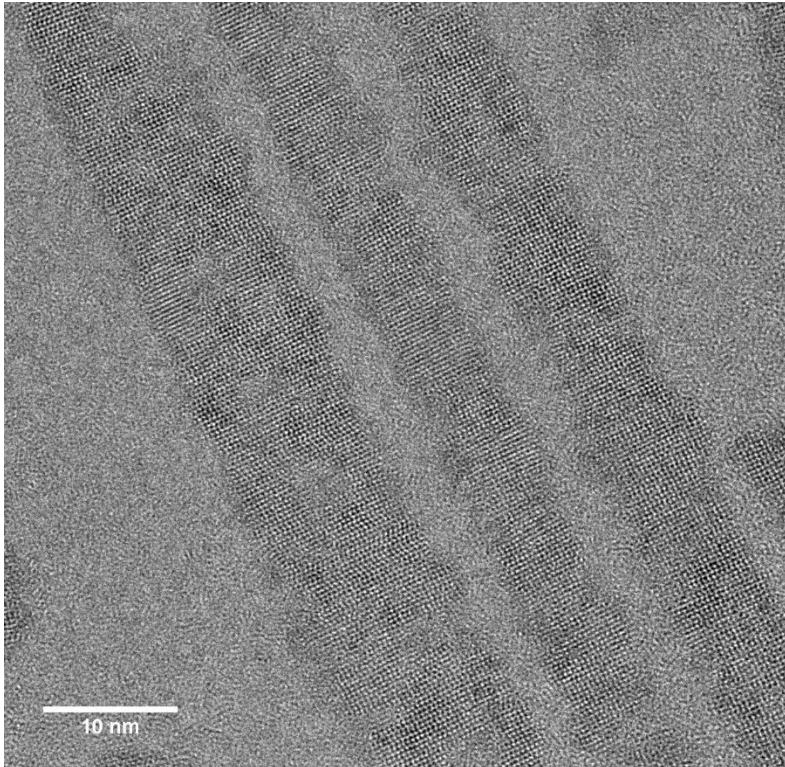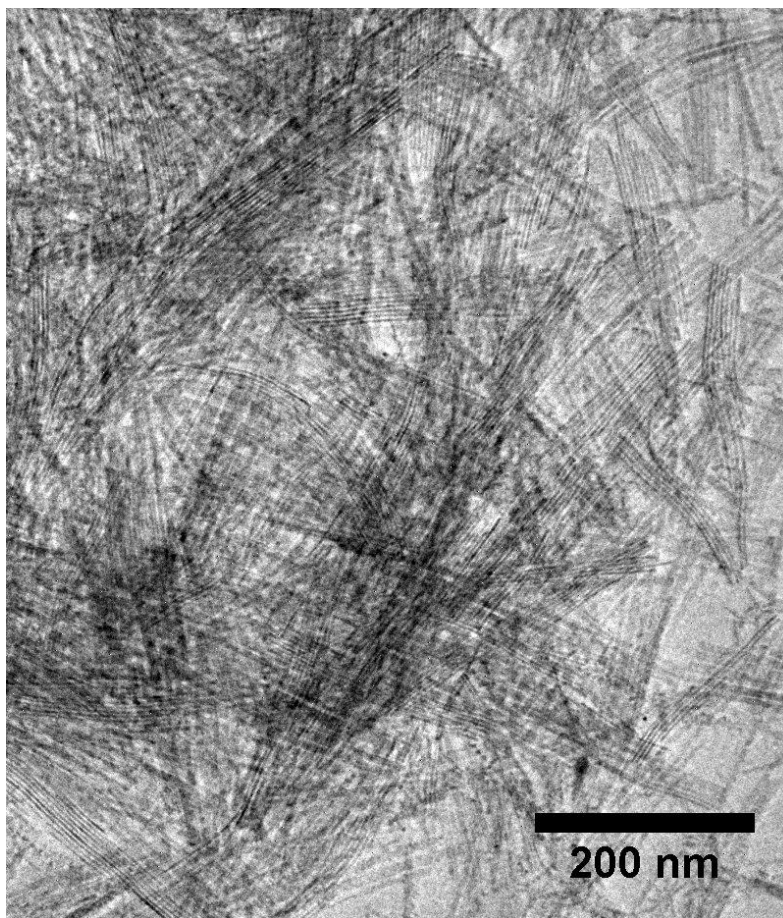
c)

Figure B.9 Additional HR-TEM images of CdSe-CdS QBs having shells of monolayer thickness. a) side view, b) broad surface facet, c) bundles.

References

1.   Onwudiwe, D. C.; Arfin, T.; Strydom, C. A.; Kriek, R. J., A study of the thermal and AC impedance properties of n-phenyldithiocarbamate complexes of Zn(II). *Electrochimica Acta* **2013,** *109*, 809-817.

2.   Zhou, Y.; Wang, F.; Buhro, W. E., Large Exciton Energy Shifts by Reversible Surface Exchange in 2D II–VI Nanocrystals. *Journal of the American Chemical Society* **2015,** *137* (48), 15198-15208.

Appendix C:

Associated Content for Chapter 5

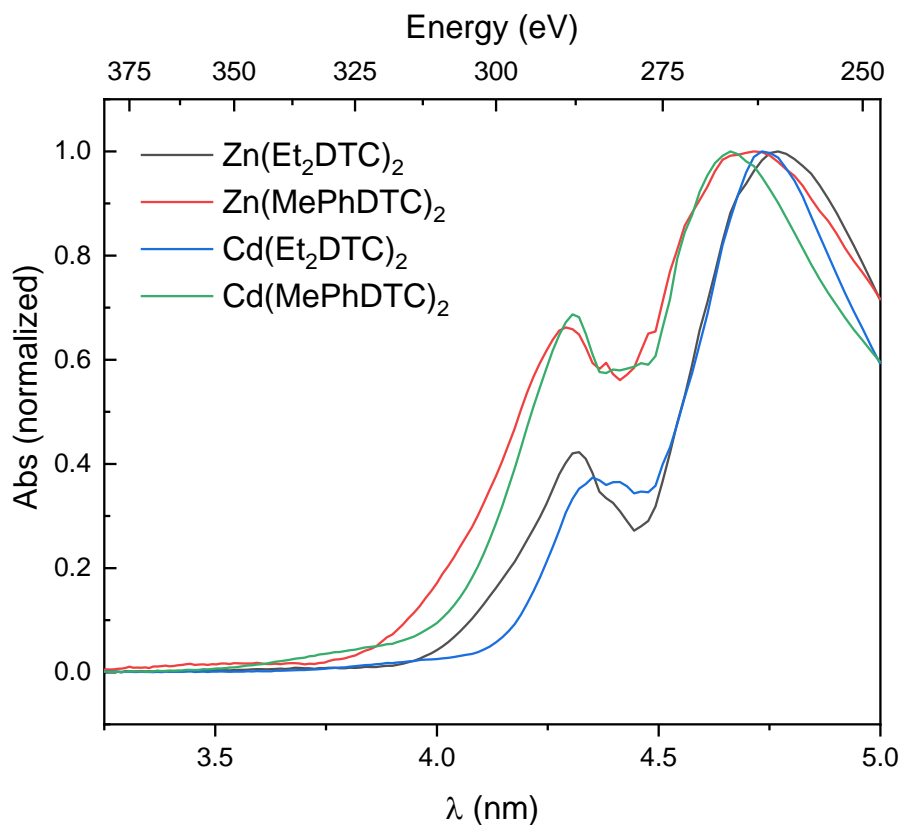## *Stable Metal Dithiocarbamates for Ligand Exchange*

Figure C.1 UV-Vis Spectra of Metal Dithiocarbamate Ligands. The absorption turn on for all four ligand cases occurs about 1 eV higher than the lowest energy transitions of the CdSe[n-alkylamine]$_{0.53}$ QBs, and should not interfere in the interpretation of energetic shifting at the band edge.
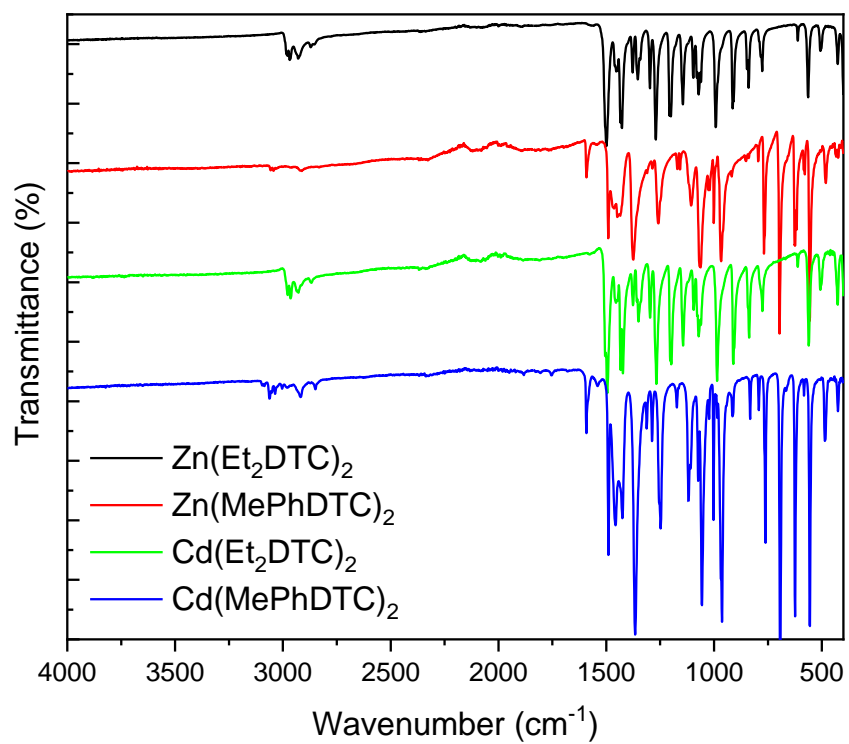
Figure C.2 FT-IR Spectra of Metal Dithiocarbamates.

Table C.1 Solubility and Stability Data

	Zn(Et₂DTC)₂	Zn(MePhDTC)₂	Cd(Et₂DTC)₂	Cd(MePhDTC)₂
Toluene	✓*+	✓	X	X
Dichloromethane	✓*	✓	X	X
Tetrahydrafuran	✓*	X	✓	X
Dimethylsulfoxide	✓*+	✓*+	✓*+	✓*+
DMF	✓*+	✓*+	✓*+	✓*+

✓ indicates soluble at concentrations >10 mg/mL.

✓* indicates soluble and stable for >12 h, monitored by ^{1}H NMR and ^{13}C{^{1}H} NMR.

✓*+ indicates soluble and stable for >4h at 40 °C, monitored by ^{1}H NMR and ^{13}C{^{1}H} NMR.

Table C.2 Shifting of the lowest energy feature of Previously Studied Z-type (MX_2) ligand exchanges.[1-2]

	Δ_{abs} (1_b-1_E)	
X	**M = Cd**	**M = Zn**
Oleate	140 ± 20	30 ± 20
Cl	252 ± 5	36 ± 5
I	151 ± 5	95 ± 5
Br	157 ± 5	89 ± 5

Figure C.3 Additional TEM Images for Exchanged Belts
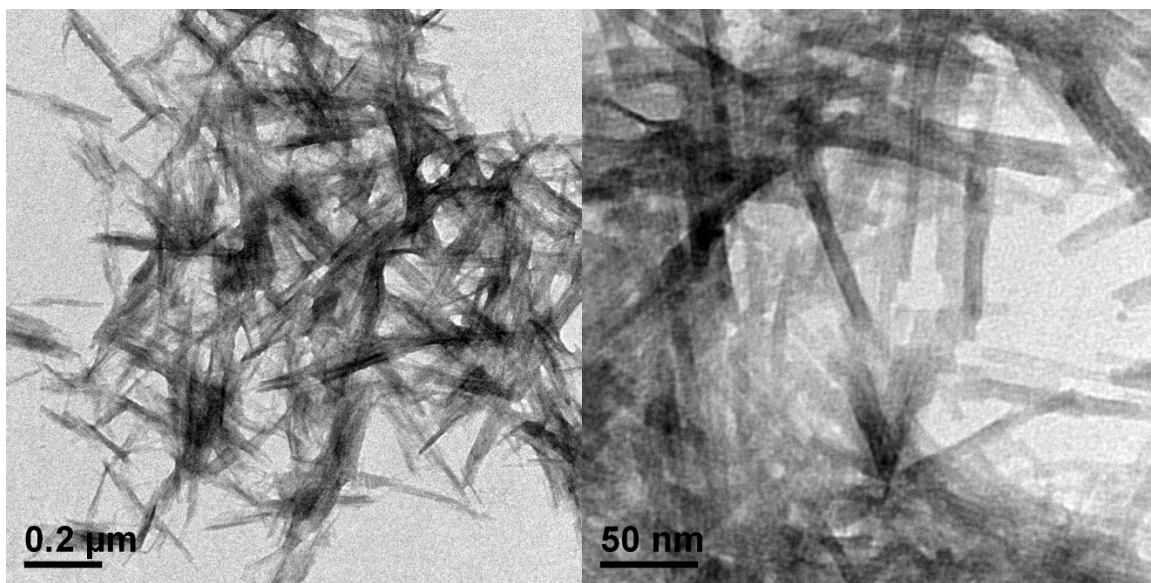
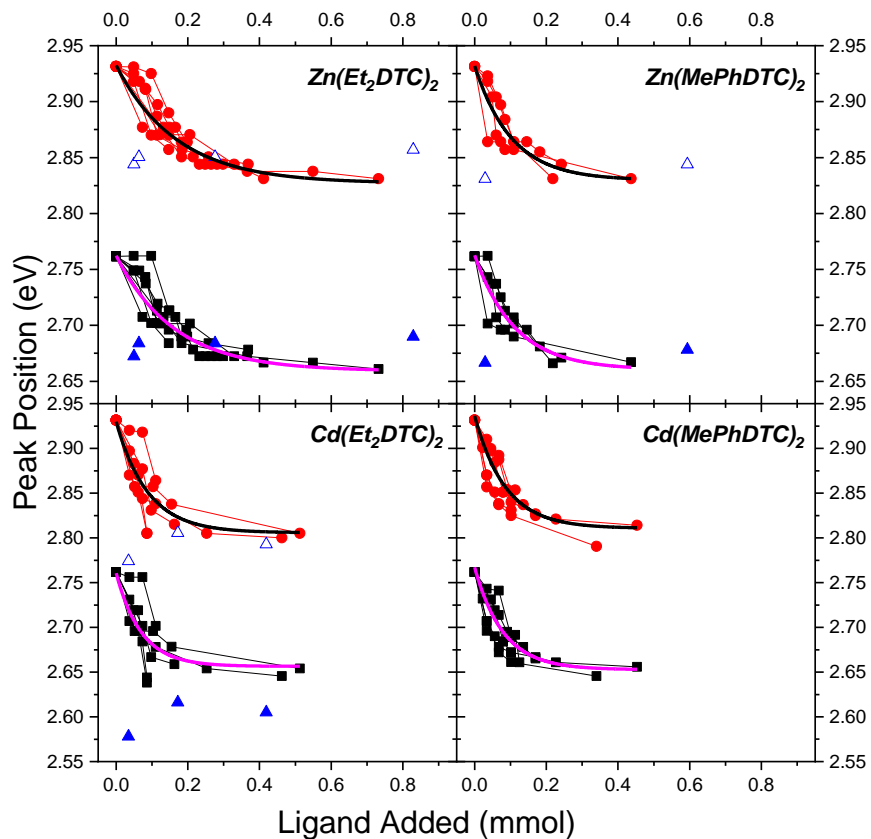**Section C.1** Exponential Decay Fits of the Direct Exchange Data

Figure C.4   Global single exponential decay fit of direct exchange data. The black squares and red circles represent the energetic positions of the 1_B-1_e and 1_A-1_e transitions, respectively. The respective fits of the data are shown by magenta and black solid lines. The fits do *not* represent the rate of exchange; instead, the fit was obtained to acquire the asymptote (y_o), which we use to determine the magnitude of the shift to lower energy of each transition.

$$y = Ae^{\frac{-x}{t_1}} + y_o$$

Table C.3 Exponential Decay Constants for 1_B-1_e Transition Data

Ligand	y_0	$A_1{}^a$	$t_1{}^a$	r^2
Zn(Et$_2$DTC)$_2$	2.65 ± 0.01	0.103 ± 0.006	1.68E-4 ± 2.21E-5	0.94
Zn(MePhDTC)$_2$	2.66 ± 0.01	0.102 ± 0.013	1.13E-4 ± 3.14E-5	0.85
Cd(Et$_2$DTC)$_2$	2.66 ± 0.01	0.104 ± 0.012	7.00E-5 ± 1.95E-5	0.94
Cd(MePhDTC)$_2$	2.65 ± 0.01	0.114 ± 0.011	7.94E-5 ± 1.77E-5	0.94

^{a} Extra digit retained. All values reported have two significant figures.

Table C.4 Exponential Decay Constants for 1_A-1_e Transition Data

Ligand	y_0	$A_1{}^a$	$t_1{}^a$	r^2
Zn(Et$_2$DTC)$_2$	2.83 ± 0.01	0.105 ± 0.006	1.70E-4 ± 2.31E-5	0.94
Zn(MePhDTC)$_2$	2.83 ± 0.01	0.102 ± 0.012	1.04E-4 ± 2.75E-5	0.83
Cd(Et$_2$DTC)$_2$	2.81 ± 0.01	0.124 ± 0.016	8.77E-5 ± 2.44E-5	0.93
Cd(MePhDTC)$_2$	2.81 ± 0.01	0.126 ± 0.012	8.56E-5 ± 1.77E-5	0.97

^{a} Extra digit retained. All values reported have two significant figures.

Section C.2 Calculating contributions to the confinement energy (E_c) from the electron in the 1e state and hole in the 1_B and 1_A states.[3]

Particle in a Well:

$$E_g = E_{g,Bulk} + \Delta E_g \qquad\qquad (C.1)$$

Change in Bandgap (ΔE_g):

$$\Delta E_g = \frac{h^2}{8L^2\left(\frac{1}{m_e^*}+\frac{1}{m_h^*}\right)} - 4E_b^{Bulk} + \Delta_{cf,Bulk} \qquad\qquad (C.2)$$

Confinement Energy of the Electron:

$$E_{c,electron} = \frac{h^2}{8L^2(m_e^*)} \qquad\qquad (C.3)$$

Confinement Energy of the Hole:

$$E_{c,hole} = -\frac{h^2}{8L^2(m_h^*)} \qquad\qquad (C.4)$$

Where:
$m_e^* = 0.12 \cdot m_e$
$m_{h,B}^* = 0.92 \cdot m_e$
$m_{h,A}^* = 0.45 \cdot m_e$
$E_b = 0.015$ eV[4]
$\Delta_{cf} = 0.026$ eV $-$ 0.040 eV[5-6]; a value of 0.026 eV was selected for calculations below.

Figure C.4 Confinement Energy (E_c)

Confinement Energy of the Electron:

$$E_{c,electron} = \frac{h^2}{8L^2(m_e^*)}$$ (C.1)

Confinement Energy of the Hole:

$$E_{c,hole} = -\frac{h^2}{8L^2(m_h^*)}$$ (C.2)

Where:

$m_e^* = 0.12 \cdot m_e$
$m_{h,B}^* = 0.92 \cdot m_e$
$m_{h,A}^* = 0.45 \cdot m_e$

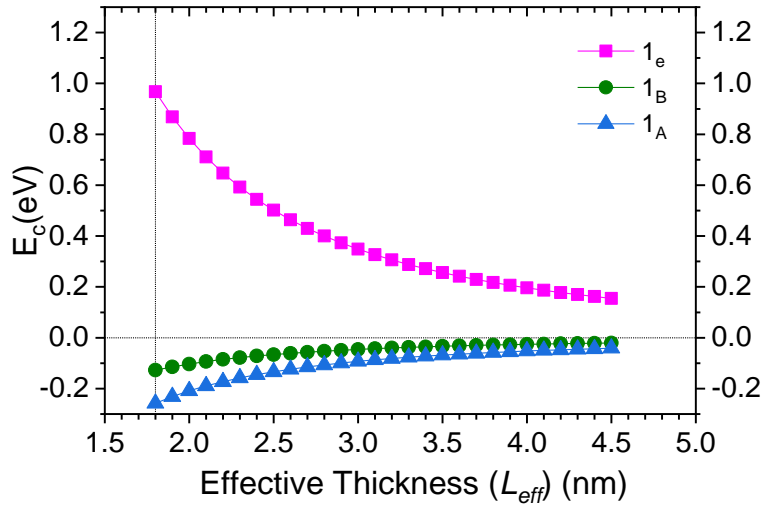**Figure C.5**. Plot of the E_c of the 1_e electron, 1_B and 1_A hole states (magenta squares, blue triangles and green circles, respectively) as a function of effective particle thickness (L) in nm. The horizontal black reference line are provided at 0 eV to guide the eye; the vertical black reference line denotes 1.8 nm, the thickness of the as-synthesized{CdSe[n-octylamine]$_{0.53}$} QBs. As the thickness of the particle increases, the E_c of the electron and hole states asymptotically approaches 0 eV. The calculations for the E_c of the electron and each hole state are performed independently (equations C.1 and C.2). Exciton binding energy (E_b) and crystal field splitting ($\Delta_{cf,Bulk}$) are not considered.

Calculation of Change in Bandgap (ΔE_g):

$$\Delta E_g = \frac{h^2}{8L^2\left(\frac{1}{m_e^*}+\frac{1}{m_h^*}\right)} - 4E_b^{Bulk} + \Delta_{cf,Bulk} \qquad\qquad (C.3)$$

The calculations for ΔE_g do consider E_b and Δ_{cf}, as noted in eq C.3 above.

Figures C.5 and C.6 plot ΔE_g for the 1_B-1_e and 1_A-1_e transitions (black squares and red circles, respectively) as a function of effective thickness (L_{eff}) of the valence and conduction bands, allowed the L_{eff} of each band to vary independently from the other. Figure C.7 plots ΔE_g if the L_{eff} of the valence and conduction bands increase together.

$\Delta\Delta E_{g(1B-1e)}$: The $\Delta\Delta E_{g(1B-1e)}$ notation refers to the energetic shift of the 1_B-1_e feature of the {CdSe[M(DTC)$_2$]$_x$} QBs *relative to* the energetic position of the 1_B-1_e feature of the {CdSe[n-octylamine]$_{0.53}$} QBs. Experimentally, a value of $\Delta\Delta E_{g(1B-1e)} \approx -0.1$ eV is observed in all M(DTC)$_2$ ligand exchange cases (value correspond to Δ_{max} values Table 5.1). Red vertical reference lines guide the eye to the corresponding L_{eff}.

$\Delta\Delta E_{g(1A-1e)}$: The $\Delta\Delta E_{g(1A-1e)}$ notation refers to the energetic shift of the 1_A-1_e feature of the {CdSe[M(DTC)$_2$]$_x$} QBs *relative to* the energetic position of the 1_A-1_e feature of the {CdSe[n-octylamine]$_{0.53}$} QBs. The $\Delta\Delta E_{g(1A-1e)}$ value is determined by using equation C.2, using the L_{eff} that corresponds to a $\Delta\Delta E_{g(1B-1e)} \approx -0.1$ eV.

$\Delta(\Delta E_{g,1A-1e} - \Delta E_{g,1B-1e})$: The $\Delta(\Delta E_{g,1A-1e} - \Delta E_{g,1B-1e})$ notation refers to the change in the energetic spacing between the 1_B-1_e and 1_A-1_e transitions. This value indicates the degree to which the 1_A-1_e and 1_B-1_e features energetically shift together. In the {CdSe[Zn(DTC)$_2$]$_x$} QBs detailed in Table 5.1, the 1_B-1_e and 1_A-1_e transitions shift by ~100 meV. The $\Delta(\Delta E_{g,1A-1e} - \Delta E_{g,1B-1e}) = 0$ eV. In the {CdSe[Cd(DTC)$_2$]$_x$} QBs, $\Delta(\Delta E_{g,1A-1e} - \Delta E_{g,1B-1e}) = 0.01$-$0.02$ eV.

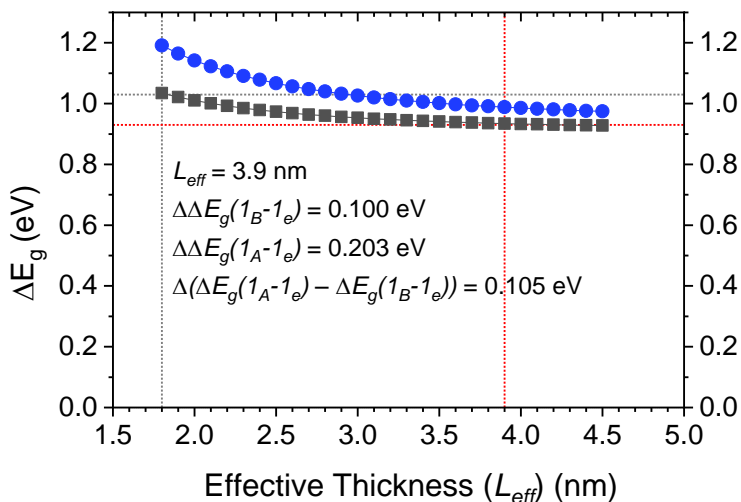**Scenario I: Preferential Modification of the Valence Band Only**

Figure C.6 Preferential modification of valence band potential only; 1_e state held constant. In order to achieve $\Delta\Delta E_{g(1B\text{-}1e)} = -0.1$ eV, L_{eff} must be 3.9 nm. We find this to be an unreasonable modification of the L_{eff} with the addition of a single ligand layer. Additionally, $\Delta(\Delta E_{g,1A\text{-}1e} - \Delta E_{g,1B\text{-}1e}) = 0.103$ eV, far in excess of any value observed in the data. We reject this scenario.

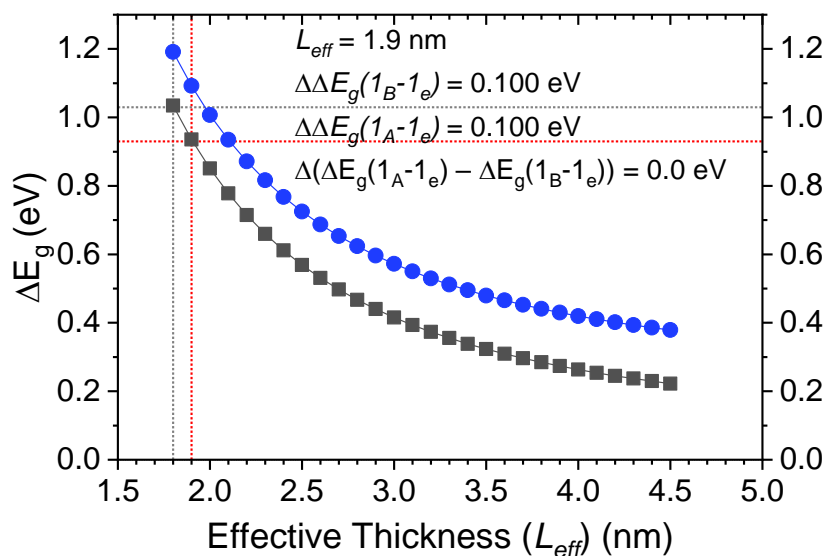**Scenario II: Preferential Modification of the Conduction Band Only**

Figure C.7 Preferential modification of the conduction band only; 1_B and 1_A hole states held constant. $\Delta\Delta E_{g(1B\text{-}1e)} = -0.1$ eV, L_{eff} must be 1.9 nm, an attainable L_{eff} with the addition of a single ligand layer. Additionally, Additionally, $\Delta(\Delta E_{g,1A\text{-}1e} - \Delta E_{g,1B\text{-}1e}) = 0$ eV, which is observed in the {CdSe[Zn(DTC)$_2$]}QBs.

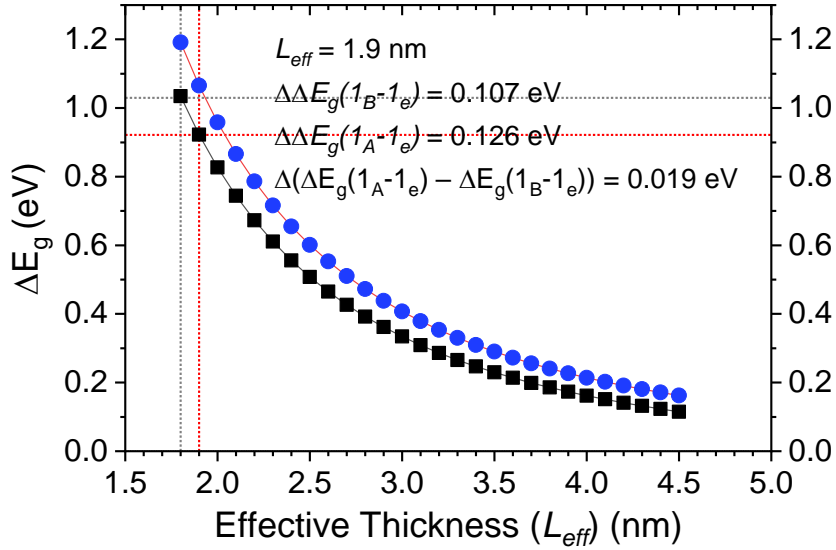**Scenario III: Modification of the valance and conduction band in unison**

Figure C.8 Modification of the valance and conduction band in unison. To achieve $\Delta\Delta E_{g(1B\text{-}1e)} = -0.107$ eV, L_{eff} must be 1.9 nm, which is an attainable L_{eff} with the addition of a single ligand layer. Additionally, Additionally, $\Delta(\Delta E_{g,1A\text{-}1e} - \Delta E_{g,1B\text{-}1e}) = 0.02$ eV, which agrees well with the observed values of 0.01-0.02 eV values in $\{CdSe[Cd(DTC)_2]_x\}$QBs.

Section C.3 Additional Experimental Notes.

Note 1. Direct exchange experiments take multiple hours to complete. UV-Vis, FT-IR must be checked before any other characterization is performed.

Complete unbundling is necessary to perform the direct exchange experiments. Unlike $Cd(oleate)_2$, the driving force for replacing the *n*-octylamine is apparently not strong enough to unbundle the belts, and doublet-like features can be seen in the UV-Vis (5×, 6×, 7× cycles in Figure C.5). We attribute this to heterogenous ligand exchange. Fully unbundled belts undergo faster exchange, while the partially bundled or bundled belts undergo a much slower exchange process, in effect creating two species in solution.

The exchange must be performed in dry solvents, and protected from atmosphere at all times. The following exchange demonstrates apparent "back-shifting" (shifting to higher energy) after exposure to environmental conditions.
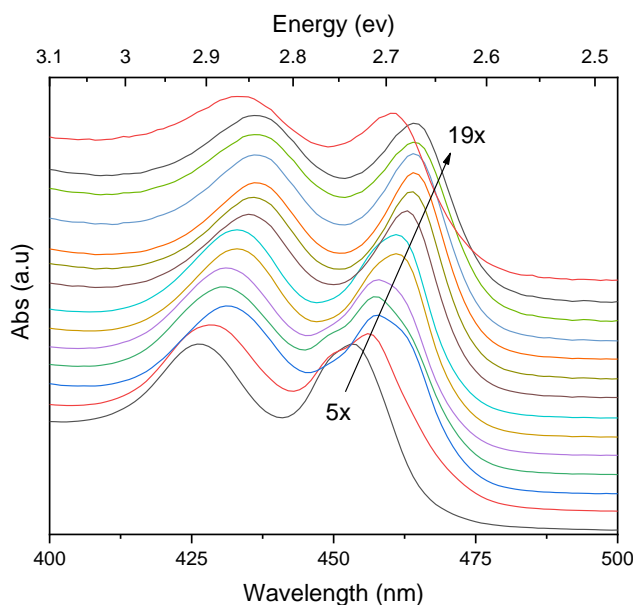

Figure C.5 Absorbance spectra of Direct Exchange with $Zn(Et_2DTC)_2$. In early ligand exchange (5×, 6×, 7× etc.) cycles, a "doublet-like" feature is seen at lower energy. We attribute this to heterogenous ligand exchange from incomplete unbundling of the as-synthesized QBs. Later in the exchange process, a shift to higher energy is observed. We hypothesize that it is possible to form ZnS late in the ligand exchange process after repeated exposure to ambient conditions, accelerated by the increased contributions from the thioureide resonance structure upon surface binding (Section 5.3.5), which is more susceptible to acidic attack than the dithiocarbamate resonance structure.

Note 2. Because of the increased instability of bound $M(DTC)_2$s (thioureide is more susceptible to acidic attack, Section 5.3.5), XRD data must be collected using a polyvinyl toluene window, which increases the difficulty of interpretation due to additional scattering.
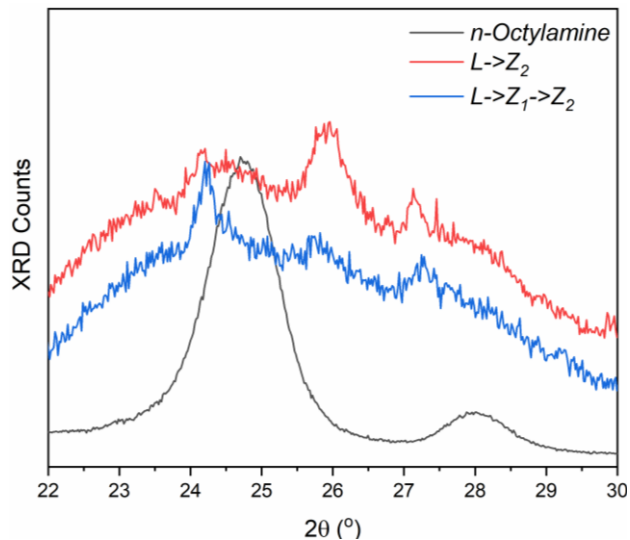

Figure C.6 XRD spectra of {CdSe[Zn(Et$_2$DTC)$_2$]} obtained via direct exchange (red) and L-Z$_1$-Z$_2$ exchange (blue), showing broadened peaks.

References

1.   Yao, Y.; Zhou, Y.; Sanderson, W. M.; Loomis, R. A.; Buhro, W. E., Metal-Halide-Ligated Cadmium Selenide Quantum Belts by Facile Surface Exchange. *Chem. Mater.* **2018,** *30* (8), 2848-2857.

2.   Zhou, Y.; Wang, F.; Buhro, W. E., Large Exciton Energy Shifts by Reversible Surface Exchange in 2D II–VI Nanocrystals. *J. Am. Chem. Soc.* **2015,** *137* (48), 15198-15208.

3.   Bui, H.; Karpulevich, A.; Bester, G., Excitonic Fine Structure of Zinc-Blende and Wurtzite Colloidal CdSe Nanocrystals and Comparison to Effective Mass Results. *Phys. Rev. B* **2020,** *101* (11), 115414.

4.   Pelant, I.; Valenta, J., *Luminescence Spectroscopy of Semiconductors*. OUP Oxford: 2012.

5.   *Semiconductors - Basic Data*. 2nd revised edition ed.; Springer: Berlin, 1996.

6.   Lew Yan Voon, L. C.; Willatzen, M.; Cardona, M.; Christensen, N. E., Terms Linear in *k* in the Band Structure of Wurtzite-Type Semiconductors. *Phys. Rev. B* **1996,** *53* (16), 10703-10714.

CALYNN JOHNSON MORRISON

SUMMARY AND OBJECTIVE
Physical materials chemist with teaching experience at the university level, including the independent development of an introductory chemistry course through University College at Washington University. Conducted interdisciplinary research in the fields of inorganic and polymeric nanomaterials. Seeking position in higher education teaching introductory, general or physical chemistry.

EDUCATION

Ph.D.	**Washington University in St. Louis**	January 2021

Chemistry, Emphasis in Physical Materials
    Advisors: Prof. Richard Loomis, Ph.D., Prof. William Buhro, Ph.D.

Dissertation: Surface Modification of II-VI Semiconducting Nanocrystals

B.S.	**College of Charleston, Honors College**	May 2013

Chemistry and Biochemistry (Double Major)

Undergraduate Thesis: Solvent Assisted Assembly of
    Poly(3-hexylthiophene)

TEACHING EXPERIENCE

Teaching Faculty	Introductory Chemistry 101/103L	Fall 2020

St. Charles Community College

- Tailored and taught introductory chemistry course material for remote learning setting. Evaluated highly by supervisors and students for effective teaching and guided learning practices.
- Course material offers a survey of concepts in chemistry, intended for non-science majors. Introduced chemical and physical principles and their applications to the properties and transformations of materials, including the concept of energy and its uses, gas laws, laws of chemical combination, atomic and molecular structure, periodic classification of the elements, and chemical bonding.

Course Instructor	Foundations in Chemistry U1005	Summer 2017

University College, Washington University in St. Louis

- Independently developed curriculum and course materials for a 2-credit hour, introductory chemistry course.
- Course materials were tailored for inmates at medium security correctional facility.
- Course content introduced topics ranging from rudimentary properties of matter and light, through structure of the atom and basic models of chemical bonding.

Teaching Assistant	General Chemistry 111	Fall 2014-2016

Washington University in St. Louis
- Led three weekly POGIL or regular recitation style sections each Fall (roughly 25-30 students per section). Evaluated highly by supervisors and students for effective teaching and guided learning practices.
- Course material offers advanced, systematic treatment of fundamental chemical and physical principles and their applications to the properties and transformations of materials, including the concept of energy and its uses, gas laws, laws of chemical combination, atomic and molecular structure, periodic classification of the elements, and chemical bonding.

Teaching Assistant   Inorganic Chemistry Laboratory   Spring 2016
Washington University in St. Louis
- Supervised and mentored upper-division chemistry majors in synthetic inorganic lab (8 students).
- Instructed students in air-free synthetic technique, and NMR, FT-IR, UV-Visible absorption, TEM data acquisition.
- Developed and enhanced procedures for quantum dot labs.

RESEARCH EXPERIENCE

Investigation of Semiconductor Nanomaterial   2015 – Present
Surface and Interface Chemistry via Ligand Replacement

Synthesized a library of organic compounds to serve as functional surface ligands for II-VI semiconductors. Installed functional and degrading ligands to alter the nanocrystal surface. Analyzed ligand binding using a variety of analytical characterization techniques. Investigated changes in electronic structure and dynamics upon surface chemistry manipulation.

Publications and Presentations

Sanderson, W. M., Hoy, J., **Morrison, C. E**., Wang, F., Wang, Y. Y., Morrison, P. J., Buhro, W. E., Loomis, R. A., Excitation Energy Dependence of Photoluminescence Quantum Yields in Semiconductor Nanomaterials with Varying Dimensionalities. J. Phys. Chem. Lett. 11, 9, 3249–3256.

Morrison, C.E., Sun, H., Yao, Y., Buhro, W. E., Loomis, R. A., Quantitative Characterization of Total Composition of II-VI Semiconducting Nanocrystals. Chem. Mater., 32, 5, 1760-1768.

Morrison, C. E., Wang, F., Wieliczka, B. M., Rath, N. P., Loomis, R. A., and Buhro, W. E. (2017), "L- to Z- to Shell: Cadmium Bis(phenyldithiocarbamate) as a Nanocrystal Shell-Growth Precursor," 69th Southeastern Regional Meeting of the American Chemical Society, Charlotte, NC, November 11, 2017. *(Oral Presentation)*

Morrison, C. E., Wang, F., Wieliczka, B. M., Rath, N. P., Loomis, R. A., and Buhro, W. E., Cadmium Bis(phenyldithiocarbamate) as a Nanocrystal Shell-Growth Precursor. Inorg. Chem., 56, 12920-12929.

Solvent Assisted Assembly of Poly(3-hexylthiophene)(P3HT)   2012 – 2015

Synthesized highly regio-regular P3HT via Grignard metathesis method (GRIM). Utilized a variety of polymer characterization, spectroscopic, and mechanical techniques to fully characterize optoelectronic polymers in solution. Employed solvent effects to control aggregation and self-assembly behavior.

Publications and Presentations

Johnson, C. E., Gordon, M. P. and Boucher, D. S. (2015). Rationalizing the Self-assembly of Poly(3-hexylthiophene) Using Solubility and Solvatochromic Parameters. J. Polym. Sci. B Polym. Phys., 53, 841–850.

Johnson, C.E., and Boucher, D.S. (2014). Poly(3-hexylthiophene) Aggregate Formation in Binary Solvents: An Excitonic Coupling Analysis. J. Polym. Sci., Part B: Polym. Phys., 52, 526-538.

Johnson, C. E. and Boucher, D. S., ″Solvent-Driven Assembly of Poly(3-Hexylthiophene) Aggregates systems,″ Annual Meeting of the South Carolina Academy of Science, Benedict College, Columbia, SC, April 13, 2013. (*Oral Presentation*)

Johnson, C. E. and Boucher, D. S., ″Spectroscopic Investigation of Poly(3-Hexylthiophene) Aggregates in Binary Solvent Systems,″ 245th ACS National Meeting, New Orleans, LA, April 10, 2013. (*Poster*)

Johnson, C. E. and Boucher, D. S., "Toward controlled polymer self-organization in solution." 64th Southeast Regional Meeting of the American Chemical Society, Raleigh, NC, United States, November 14-17, 2012. (*Poster*)

MENTORING

Inorganic Synthesis & Characterization   Fall 2015 – Present
- Yuewei Yao
- Stephanie Pecaro

Spectroscopy   Summer 2017 – Present
- Jie Chen

AWARDS AND FUNDING

Awards
- Department of Chemistry Teaching Excellence Award (WUSTL) 2015
- HyperCube Research Student of the Year (CofC) 2013

Funding
- Major Year Academic Scholarship Grant (URCA) ($2,500)
- SERMACS Undergraduate Research Presentation Grant ($200)
- Research Presentation Grant (URCA) ($200)
- Howard Hughes Medical Institute Undergraduate Research Education Grant Recipient ($8,500)

OUTREACH & AFFILIATIONS

Catalyst for Change Volunteer (2014-2017)
ACS Member (2013-Present)